Université de Liège

UNIVERSITÉ DE GRENOBLE

THÈSE

Pour obtenir le grade de

DOCTEUR DE L'UNIVERSITÉ DE GRENOBLE

Spécialité : **Matériaux, Mécanique, Génie civil, Electrochimie**

Arrêté ministériel : 7 août 2006

Et de

DOCTEUR DE L'UNIVERSITÉ DE LIÈGE

Spécialité : **Sciences**

Présentée par

Alina PRIKOCKYTĖ

Thèse dirigée par
Catherine DUBOURDIEU et **Philippe GHOSEZ**

préparée au sein
du **Laboratoire des Matériaux et Génie Physique**
dans **l'École Doctorale Ingénierie - Matériaux, Mécanique, Environnement, Energétique, Procédés, Production**
et
du **Service de Physique Théorique des Matériaux**
dans **l'École Doctorale Sciences Physiques**

First-principles and experimental studies of hexagonal $YMnO_3$ single crystals and epitaxial films

Thèse soutenue publiquement **le 29 Octobre 2012**,
devant le jury composé de :

M. John MARTIN
Professeur, Université de Liège (Président)
M. Wilfrid PRELLIER
Dir. de Recherche, CRISMAT-CNRS (Rapporteur)
M. Ludger WIRTZ
Professeur, Université de Luxembourg (Rapporteur)
M. Michel PONS
Dir. de Recherche, SIMAP-CNRS (Membre)
M. Eric BOUSQUET
Chercheur Qualifié FNRS, Université de Liège (Membre)
Mme Catherine DUBOURDIEU
Dir. de Recherche, LMGP-CNRS (Directrice de thèse)
M. Philippe GHOSEZ
Professeur, Université de Liège (Directeur de thèse)

To my lovely daughter Rugilė

Acknowledgements

My PhD thesis was full of colourful experiences. I faced various approaches to research – unknown theoretical and more familiar experimental; daunting, but enriching teaching activities; wide possibilities to share and acquire the knowledge at conferences and meetings. It was a big honor and pleasure to meet and work with many people.

First thanks I dedicate to my advisors Catherine Dubourdieu and Philippe Ghosez for giving me an opportunity to join their team and make my thesis, their availability to discuss and scientific guidance. I very appreciated I could rely and keep my motivation on scientific ideas. I am very thankful for support and flexibility through I could successfully continue my thesis after the birth of my daughter.

I would like to thank to Jury Members for having agreed to be in my Thesis Committee.

First steps in the theoretical field I made with guidance of Eric Bousquet. I thank for the comprehensive explanations and shearing knowledge using Abinit code.

Thanks to Daniel Bilc and Julien Varignon for a fruitful collaboration and the Crystal data.

For sharing their experience in Raman measurements, I would like to thank to Samuel Margueron and Pierre Bouvier.

It was good to know that X-ray diffraction measurements were in good hands. Thanks to Hervé Roussel for availability to answer the questions.

I am grateful to Gwilherm Nénert and Thomas Palstra for providing the $YMnO_3$ single crystals.

I would like to thank to Peter Schlagheck, Alejandro Silhanek, Matthieu Verstraete, Alain Pirlot and Christelle Prospery for an accordant pedagogical work together.

I particularly would like to thank my colleagues with whom I shared my office and enjoyed their pleasant company discussing science and life: Engin Durgun, Safari Amisi, Patrick Hermet, and Zeila Zanolli.

Thanks to colleagues for a cosy and friendship working atmosphere: Isabèle Gélard, Céline Otjacques, Rengin Pekoz, Hania Djani, Henu Sharma, Marco Goffinet, Denis Fontaine, Satadeep Bhattacharjee, Srijan Kumar Saha, Jinzhu Zhao, Naihua Miao, Nicholas Bristowe, Momar Diakhate, Bin Xu, Marco di Gennaro, Theodoros Papadopoulos, Jean-Yves Raty, Osman Baris Malcioglu, Wilfredo Ibarra Hernandez.

Nuoširdžiai ačiū to my first advisor Rolandas Tomašiūnas for a scientific enthusiasm and amiable work together; to colleague Regina Beresnienė for a pleasant working atmosphere.

Širdingai ačiū to my husband Paulius for support, help, love and especially for a passion for physics in laboratory and everyday life; to my wonderful daughter Rugilė, who brought new colors into my life and perturbed my minds in good sense; to my family and to Paulius family for support and being together. Destiny itself is not valuable if not experienced and sheared with beloved people.

Contents

Introduction

Multiferroic materials have attracted much interest during the recent years. Our study is devoted to a prototypic system: yttrium manganite. In particular, we focus on the ferroelectric properties in bulk and in thin film forms. Yttrium manganite belongs to the class of ABO_3 compounds. Most theoretical studies of ferroelectricity to date were concentrated on cubic perovskite ABO_3. Yttrium manganite is hexagonal and is an improper ferroelectric. We were interested to study theoretically and experimentally how these two features behave in thin film form. Our study is organized as follows.

In the first two chapters, we overview the general framework of this thesis. In Chapter 1, we present the class of multifunctional ABO_3 compounds potentially attractive for wide applications and the most characteristic phenomena: the magnetoelectric effect, multiferroicity and ferroelectricity. Further on, we introduce hexagonal yttrium manganite and emphasize on improper ferroelectricity. In Chapter 2, we describe our used theoretical (first-principles calculations) and experimental (Raman spectroscopy, Metal organic chemical vapour deposition and X-Ray diffraction) techniques and provide the related technical details.

In the next chapters, we report our various theoretical and experimental results for $YMnO_3$ in bulk and thin film form.

In Chapter 3, we report and discuss the structural properties computed from first principles of both high-temperature paraelectric and ground-state ferroelectric phases of bulk $YMnO_3$ in comparison to other theoretical and experimental data available in the literature.

In Chapter 4, we present never previously reported dynamical properties computed from first principles of paraelectric and ferroelectric bulk $YMnO_3$. We extend this theoretical study with

our own experimentally measured Raman spectra of ferroelectric $YMnO_3$ single crystal. The crystal was found to be miscut, but our computed angular dispersion curves explained the obtained experimental results. All our theoretical and experimental data are discussed in comparison to other theoretical and experimental data available in the literature.

On one hand, Chapter 3 and Chapter 4 count as the important individual parts to supplement the knowledge in the structural and dynamical properties of hexagonal $YMnO_3$. One the other hand, these parts are complementary and at the same the necessary parts in order to build a model based on first-principles calculations for epitaxial thin films of $YMnO_3$ presented in Chapter 5, which opened the possibilities to study the role of epitaxial strain on hexagonal perovskites and the role of electrical boundary conditions on improper ferroelectrics.

In Chapter 6, we report the experimental study of structural and dynamical properties of $YMnO_3$ epitaxial thin films grown by MOCVD. The obtained results for films are discussed in comparison to those for bulk reported in Chapter 3 and Chapter 4. The experimental results are understood and explained using the first-principles model presented in Chapter 5.

Chapter 1

Magnetoelectric effect, multiferroism and ferroelectricity in ABO_3 compounds

The present chapter overviews the general framework of this thesis. It is divided into five sections. The first one introduces the ABO_3 oxide compounds and their incredible variety of functional properties. The next three sections present the main concepts of the magnetoelectric effect, the class of multiferroic materials and the ferroelectricity. The last section is devoted to yttrium manganite ($YMnO_3$), which is one of the most intensively studied hexagonal multiferroics and is at the center of this thesis.

1.1 Multifunctional ABO_3 compounds

The ABO_3 oxide compounds mainly crystallize into a simple *perovskite* structure (from the mineral perovskite $CaTiO_3$). The ideal perovskite structure is a cubic structure with the space group $Pm\bar{3}m$ (221) and contains five atoms in a unit cell with the A atom at the corner of the cube, the B atom at the center and the O atoms are located at the center of each face (Figure 1.1). The oxygen atoms form an octahedron with B atom at the center.

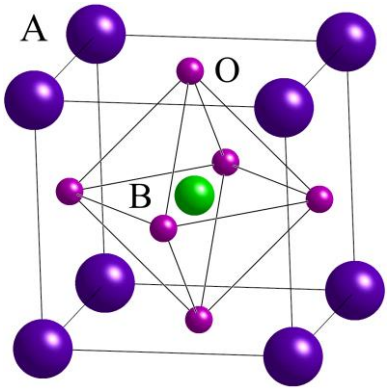

Figure 1.1 Structure of the ideal cubic perovskite.

The A and B sites can support metal cations with a wide range of sizes and valences, which causes a variety of different orderings and physical phenomena (ferroelectricity, superconductivity, ferromagnetism,…) (Figure 1.2).

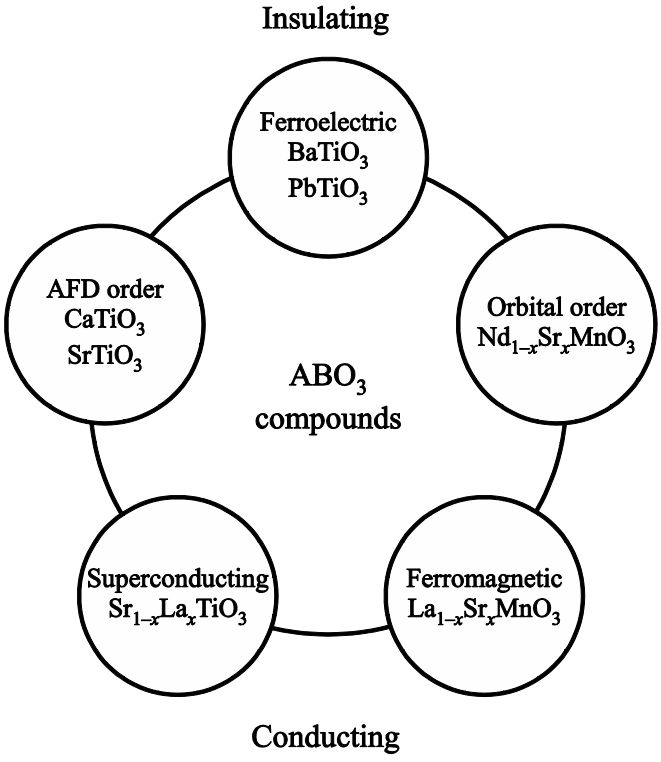

Figure 1.2 ABO_3 perovskites and related layered compounds with a broad spectrum of functional properties (taken from Ref. [1]).

Thanks to their similar structure, ABO_3 compounds can be easily combined in various type of nanostructures. The most common configurations are multilayers and thin films grown on a substrate. The ability to control the growth of oxides on the atomic scale opened the possibilities to fabricate the high-quality heterostructures leading to undiscovered field of properties. As illustrated in Figure 1.3, creating interfaces between different compounds one can expect not only to combine or amplify the properties of the perovskite compounds, but to act on various degrees of freedom (lattice, spin, charge, orbitals) through various effects (epitaxial strain, charge transfer at the interface, symmetry breaking…). For instance, a magnetoelectric coupling between electrical polarization and magnetization was constructed in heterostructures consisting of piezoelectric and magnetostrictive materials. Through the mechanical coupling, the magnetic field induces strain in the magnetostrictive material and propagates into the piezoelectric layer generating an electrical response.

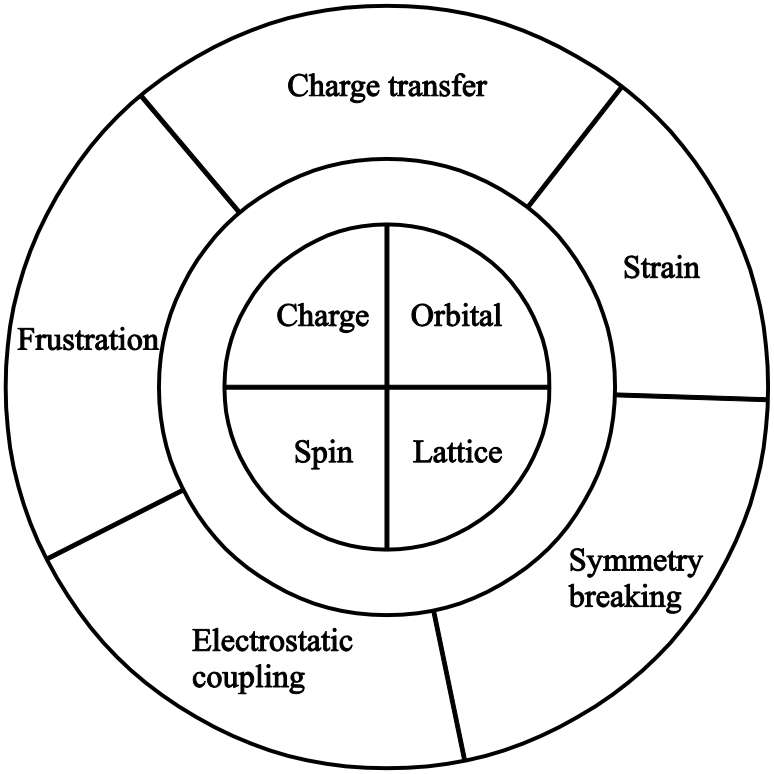

Figure 1.3 The interactions of oxides at the interface between their charge, orbital, spin and lattice degrees of freedom (taken from Ref. [1]).

The stability condition of the ideal cubic perovskite structure depends on the radii of A, B and O atoms controlled by the Goldschmidt tolerance factor *t*:

$$t = \frac{R_A + R_O}{\sqrt{2}\ R_B + R_O}, \tag{1.1}$$

where R_A, R_B and R_O are the ionic radii of A, B and O atoms in the ABO_3 structure (see Figure 1.1), respectively.

For the ideal cubic structure, the tolerance factor $t = 1$ (Figure 1.4). The ionic radii R_A, R_B and R_O are such that all the anions (O atoms) just touch the cations (A and B atoms). When $(R_A + R_O) > \sqrt{2}(R_B + R_O)$, the tolerance factor is $t > 1$ and the B atom is too small for the oxygen octahedron meaning that the B atom has the freedom to move. These perovskites tend to be B-type ferroelectrics as a small polar distortion is developed. When $(R_A + R_O) < \sqrt{2}(R_B + R_O)$, the tolerance factor is $t < 1$ and this time the A atom is too small for the structure and cannot effectively bond with neighboring O atoms. This leads to phases with tilts of the oxygen octahedra or A-type driven ferroelectricity. The structures with the tolerance factor $t \ll 1$ $(R_A = R_B)$ are far from ideal perovskite structure that becomes unfavored compared to hexagonal structures (Figure 1.5).

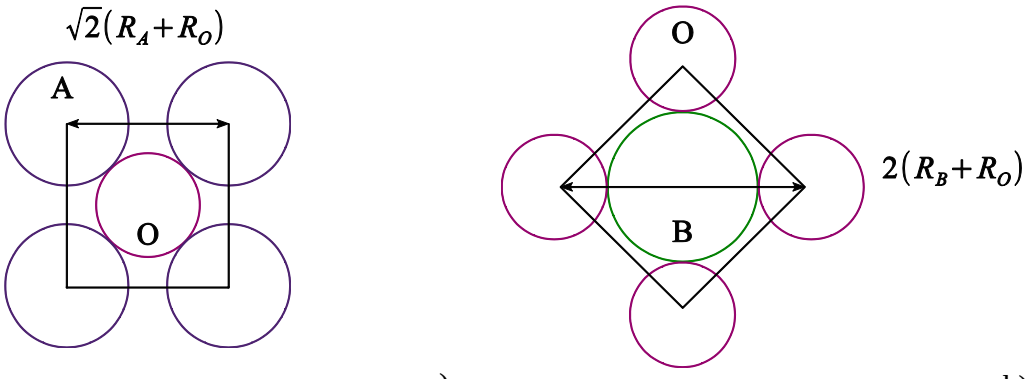

Figure 1.4 Lattice parameter *a* in terms of A and B atoms ionic radii: AO (a) and BO (b) planes of cubic perovskite structure shown in Figure 1.1. Tolerance factor $t = 1$.

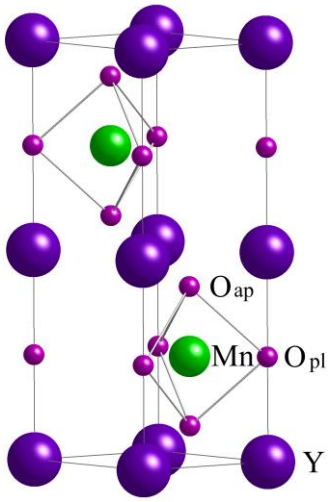

Figure 1.5 Structure of the hexagonal perovskite $YMnO_3$ (space group: *P6₃/mmc*).

A atom	R_A (Å) [2]	Tolerance
Er	0.95	0.75
Gd	0.94	0.74
Tb	0.92	0.74
Dy	0.91	0.73
Sc	0.75	0.68
In	0.80	0.70
Ho	0.89	0.73
Er	0.89	0.73
Tm	0.88	0.72
Yb	0.86	0.72
Lu	0.86	0.72
Y	0.90	0.73

Table 1.1 Tolerance factor *t* for hexagonal manganites $RMnO_3$ with R = A atom. The ionic radius of Mn atom (B atom) and O atoms are $R_B = 0.83\,\text{Å}$ and $R_O = 1.27\,\text{Å}$ taken from Ref. [2], respectively.

The rare-earth manganites belongs to the family of ABO_3 compounds through a chemical formula $RMnO_3$, where A = R is a trivalent rare earth ion and B = Mn is a trivalent manganese ion. As shown in Table 1.1, the compounds of this family have a small tolerance factor $t \ll 1$ and are at the tolerance factor limit.

On the one hand, the the rare-earth manganites with the largest tolerance factor meaning with larger A cations (Eu, Gd, Tb, Dy) prefer to crystallize into the most common distorted perovskite-type orthorhombic phase.

On the other hand, the rare-earth manganites with a smaller tolerance factor meaning with smaller A cations (Sc, In, Ho, Er, Tm, Yb, Lu), including $YMnO_3$ studied in this work, crystallize into the hexagonal $P6_3cm$ phase.

However, since the deviation in tolerance factors of the rare-earth manganites is not broad, the orthorhombic manganites can be stabilized into the hexagonal phase and vice versa.

A magnetoelectric effect occurring in some ABO_3 compounds as a results of the electric and magnetic orderings coupling is presented in the next section.

1.2 Magnetoelectric effect

The coupling between the electric polarization $\boldsymbol{P}$ and a magnetic field $\boldsymbol{H}$ or between magnetization $\boldsymbol{M}$ and an a electric field $\boldsymbol{E}$ is called a magnetoelectric (ME) effect.

The free energy F in terms of electric and magnetic field of magnetoelectric material is expended as follows [3]:

$$\begin{aligned} F(\boldsymbol{E},\boldsymbol{H}) = F_0 - P_i^S E_i - M_i^S H_i \\ -\frac{1}{2}\epsilon_0\epsilon_{ij}E_iE_j - \frac{1}{2}\mu_0\mu_{ij}H_iH_j - \alpha_{ij}E_iH_j \\ -\frac{1}{2}\beta_{ijk}E_iH_jH_k - \frac{1}{2}\gamma_{ijk}H_iE_jE_k - ..., \end{aligned} \tag{1.2}$$

where, P_i^S and M_i^S are the spontaneous polarization and magnetization, respectively, in direction *i*, ε and μ are the dielectric permittivity and magnetic permeability, α is the linear magnetoelectric susceptibility tensor, β and γ are the high order terms parameterizing the nonlinear ME effect.

The electric polarization P_i along a given direction *i* is obtained after differentiating the energy with respect to the electric field in direction *i*:

$$\begin{aligned} P_i\ (\boldsymbol{E},\boldsymbol{H}) &= -\frac{\partial F}{\partial E_i} \\ &= P_i^S + \epsilon_0 \epsilon_{ij} E_j + \alpha_{ij} H_j \\ &\quad + \frac{1}{2}\beta_{ijk} H_j H_k + \gamma_{ijk} H_i E_j - \ldots \end{aligned} \tag{1.3}$$

The magnetization M_i along a given direction *i* is obtained after differentiating the energy with respect to the magnetic field in direction *i*:

$$\begin{aligned} M_i\ (\boldsymbol{E},\boldsymbol{H}) &= -\frac{\partial F}{\partial H_i} \\ &= M_i^S + \mu_0 \mu_{ij} H_j + \alpha_{ij} E_j \\ &\quad + \beta_{ijk} E_i H_j + \frac{1}{2}\gamma_{ijk} E_j E_k - \ldots \end{aligned} \tag{1.4}$$

The linear magnetoelectric susceptibility α_{ij} then is defined as

$$P_i = \alpha_{ij} H_j, \tag{1.5}$$

$$M_j = \alpha_{ji} E_i. \tag{1.6}$$

This means that an electric polarization $\boldsymbol{P}$ can be induced via an applied magnetic field $\boldsymbol{H}$ or a magnetization $\boldsymbol{M}$ can be induced via an applied electric field $\boldsymbol{E}$.

It is usually accepted that the linear ME effect responses α_{ij} is bound by the electric χ_{ii}^e and magnetic χ_{jj}^m susceptibilities through relation given as follows [4]:

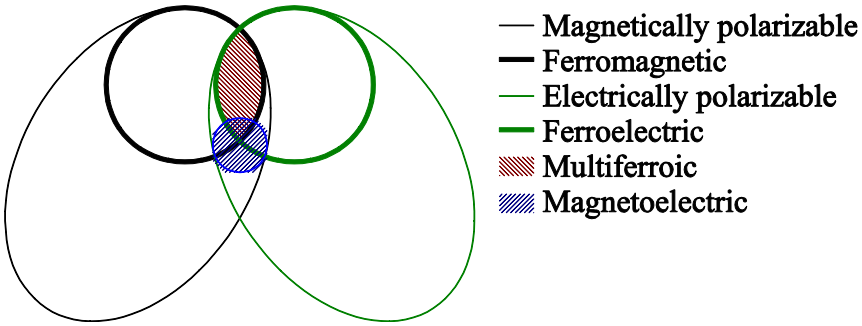

Figure 1.6 Multiferroics and Magneto-electrics are distinct classes of materials that can exist independently (taken from Ref. [5]).

$$\alpha_{ij}^2 < \chi_{ii}^e \chi_{jj}^m. \tag{1.7}$$

This relation motivated the search of materials that are both ferroelectric and ferromagnetic expecting to combine the large electric and large magnetic susceptibilities and thus to observe a significant ME effect. In the search of new magneto-electrics, a specific attention was then devoted to multiferroics.

As shown in Figure 1.6, it is however important to distinguish these two classes of materials because a magnetoelectric is not necessarily a multiferroic (and vice versa), although a significant ME effect might be observed in a multiferroic material, as in case of hexagonal $YMnO_3$ studied in this work.

1.3 Multiferroic materials

A material is considered as a multiferroic when at least two ferroic orderings (ferroelasticity, ferroelectricity, ferromagnetism and ferrotoroidicity) exist in the same phase. The definition is often extended to antiferroic orderings. Although any combination of ferroic orderings refers to multiferroics, most commonly, the materials are considered as multiferroics when the simultaneous presence of ferroelectric and (any) magnetic orderings is observed (i.e.

multiferroic is a shortcut that implicitly refers to the subclass of "magneto-electric" multiferroics).

The majority of multiferroic materials that show an interest of the ME effect for the applications are qualified in four crystallographic groups:

1. *Compound with perovskite structure*: These compounds with chemical formula ABO_3 (see Section 1.1) and their ferroelectric properties are intensively studied theoretically as well as experimentally.
2. *Compounds with hexagonal structure*: When the cation radius is enough small, the compounds ABO_3 crystallizes into the hexagonal structure rather than in usual perovskite structure. The number of manganites with chemical formula $RMnO_3$ (with R = Sc, Y, In, Ho, Er, Tm, Yb, Lu) belongs to this class and are simultaneously ferroelectric and antiferromagnetic.
3. *Compounds of boracites class*: The materials with chemical formula $M_3B_7O_{13}X$ (with M = Cr, Mn, Fe, Co, Cu, Ni and X = Cl, Br, I) are generally ferroelectric, antiferroelectric and ferroelastic, and usually crystalizes into a cubic and/or orthorhombic structure. The $Ni_3B_7O_{13}I$ is the first material discovered to show simultaneously ferroelectric and ferromagnetic orderings [6].
4. *Compounds of type $BaMF_4$* (with M = Mg, Mn, Fe, Co, Ni, Zn): These materials crystallize into the orthorhombic structure and are simultaneously ferroelectric and antiferromagnetic.

The next section details more the concept of ferroelectricity presenting the main definition and classification of proper and improper ferroelectrics.

1.4 Proper and improper ferroelectricity

A material is classified as ferroelectric when at zero applied electric field it has a non-zero electric polarization referred to as "spontaneous polarization". In addition, this electric polarization must be switchable between different metastable states by the application and

removal of an electric field. The coupling between the field ***E*** and polarization ***P*** causes the changes of the relative energy of the states and gives rise to electric hysteresis loop (Figure 1.7). In addition, to be a ferroelectric a material must be insulating (otherwise the mobile charges would screen out the electric polarization) and the structure of the crystal must contain a polar space group.

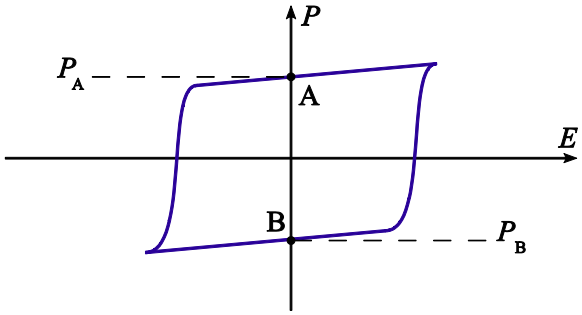

Figure 1.7 A typical P-E hysteresis loop. One half of the difference $\boldsymbol{P}_{\mathrm{B}} - \boldsymbol{P}_{\mathrm{A}}$ defines the magnitude of the spontaneous polarization $\boldsymbol{P}_{\mathrm{s}}$ in the vertical direction.

The key concept of ferroelectricity – polarization – can be measured experimentally as well as determined from the calculations. Experimentally the polarization is determined measuring the electric current going through a ferroelectric capacitor when the polarization is switched. The magnitude of spontaneous polarization can also be estimated theoretically using Born effective charges Z^* and distortions ξ from a reference centrosymmetric structure to the ferroelectric phase as follows

$$P = \frac{1}{\Omega}\sum Z^* \xi, \tag{1.8}$$

where Ω is the volume of the unit cell. The polarization can also be more accurately determined using the Berry phase formalism [7].

Most ferroelectrics undergo a structural phase transition from a non-polar centrosymmetric paraelectric phase (usually referred to a high-symmetry phase) to a polar noncentrosymmetric

ferroelectric phase when lowering the temperature. The transition mechanism is different in proper and improper ferroelectrics.

Non-ferroelectric materials are characterized by a single-well energy potential in terms of polarization having its minimum at zero polarization as shown in Figure 1.8 (red curve). Proper ferroelectric materials are characterized by a double-well potential and a minimum of energy at non-zero polarization (Figure 1.8, green curve). The negative curvature of the energy at the origin, corresponding to the reference paraelectric phase, is associated to an imaginary frequency of a given unstable zone-center polar mode. The ferroelectric phase transition arises from the condensation of this unstable polar mode, which turn will lead to a small change of the cell size and shape. The spontaneous polarization is produced directly by the condensation of the polar mode that acts as a primary order parameter.

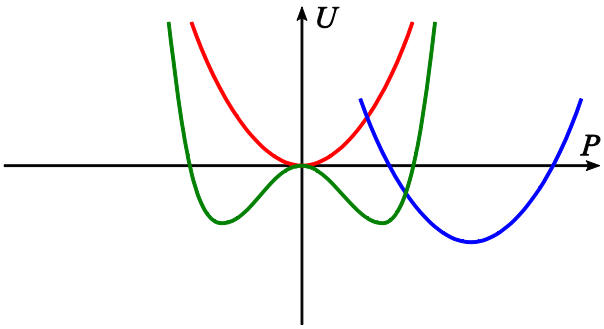

Figure 1.8 Internal energy *U* as a function of polarization for a non-ferroelectric material (in red), for a ferroelectric material (in green) and for an improper ferroelectric (in blue).

Improper ferroelectrics are characterized by a single-well energy potential in terms of polarization as shown in Figure 1.8 (blue curve). In this case, there is no unstable polar mode in the paraelectric phase (red curve). The ferroelectric transition is driven by an unstable non-polar mode that through a linear coupling with the polar mode will shift energy well of the latter to lower energy and induce a non-zero polarization (from red to blue curve in Figure 1.8). In improper ferroelectrics, the spontaneous polarization is a secondary order parameter coupled to a primary non-polar lattice distortion. More detailed discussion is reported in Section 1.5.2.

1.5 Hexagonal yttrium manganite ($YMnO_3$)

1.5.1 Introduction

Hexagonal yttrium manganite is a multiferroic material, in which the simultaneous occurrence of the ferroelectric and magnetic orderings exist at low temperature.

On one hand, as shown in Figure 1.9, at room temperature, $YMnO_3$ is ferroelectric (FE) [8,9] with an experimentally reported spontaneous polarization $P \sim 5.5\mu C/cm^2$ [10]. At the Curie temperature $T_C \simeq 1273\,K$, it undergoes a ferroelectric phase transition from a FE to a paraelectric (PE) phase [11]. The high-temperature PE phase is in *$P6_3/mmc$* space group (Figure 1.5).

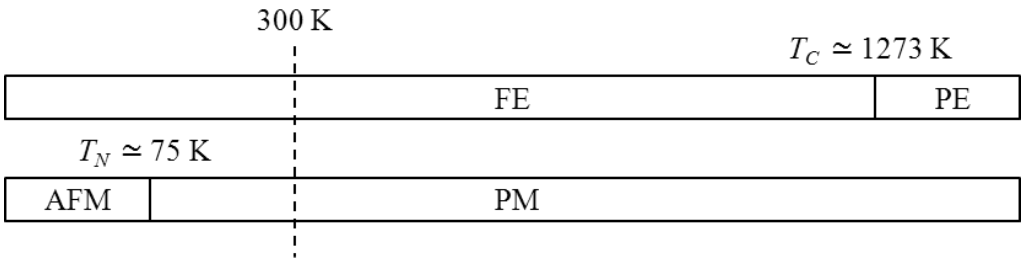

Figure 1.9 Temperature scale of the electric and magnetic phase transitions in hexagonal $YMnO_3$.

On the other hand, YMO_3 is an A-type antiferromagnetic material. At the Néel temperature $T_N \simeq 75\,K$ (Figure 1.9), it undergoes a magnetic phase transition from an antiferromagnetic (AFM) to a paramagnetic (PM) phase [12].

$YMnO_3$ is multiferroic only below $75\,K$. Although a big difference between the critical temperature of electric and magnetic orderings may suggest that no magnetoelectric coupling is present, the anomalies in the dielectric constant [13] and the optical measurements [14] confirm the existence of the ME effect in this compound.

1.5.2 Geometrically driven ferroelectricity

As presented in the previous section, $YMnO_3$ is a ferroelectric material. The mechanism for ferroelectricity has been already identified [15,16] classifying $YMnO_3$ as an improper ferroelectric [16]. In the following, we summarize the discussions concerning the origin of ferroelectricity in $YMnO_3$ mainly based on Fennie and Rabe first-principles modelling [16] as their developed model form a basis for our model presented and discussed in Chapter 5.

Fennie and Rabe through the group theoretical analysis proposed [16] that there are three symmetry-allowed paths from a high-temperature paraelectric (PE) *P6₃/mmc* to a low-temperature ferroelectric (FE) *P6₃cm* phase of $YMnO_3$ shown in Figure 1.10. Our calculations discussed in Section 4.4 in Chapter 4 and Chapter 5 are in agreement with this scheme and argued evidences that the Path (3) is the most natural phase transition from PE to FE driven by a highly unstable zone-boundary K_3 mode.

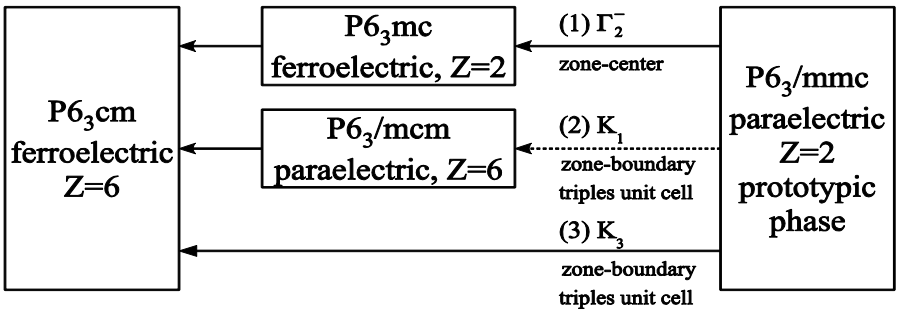

Figure 1.10 Symmetry-allowed ferroelectric phase transition paths from the high-temperature paraelectric *P6₃/mmc* to the low-temperature ferroelectric *P6₃cm* phase of $YMnO_3$ (taken from Ref. [16]).

The Path (1) with a probable *P6₃mc* intermediate phase was discarded since this is still a phase with 10 atoms in a unit cell contrary to the experimental measurements that confirmed the unit cell tripling (of the 10-atoms cell) occurring before or at the FE transition. The Path (2) at least was not in contradiction with experimental observations: first, the unit cell tripling at 1273 K and, second, the experimental signs of intermediate paraelectric phase

P6₃/mcm below this temperature at about 1000 K. Although, contrary to what was expected by Aken and *al.* [15], in Chapter 5 of this work we show that there is no unstable K_1 mode in the paraelectric phase and the contribution of K_1 to FE transition is negligible ruling out this path.

In order to realize the Path (3), Fennie and Rabe [16] decomposed the ferroelectric distortion into the symmetry-adapted modes of the paraelectric phase and determined that a non-polar zone-boundary K_3 mode and a polar zone-center Γ_2^- mode are the dominant modes in the ferroelectric distortion that relates the paraelectric phase and the low-temperature ferroelectric phase.

Further on, the performed energy calculations revealed that although $YMnO_3$ is ferroelectric, the polar Γ_2^- is stable showing a characteristic single-well energy potential (Figure 1.11, top) and only the non-polar K_3 mode is unstable with a double-well potential (Figure 1.11, bottom) meaning that the K_3 is a primary order parameter in the ferroelectric transition in $YMnO_3$.

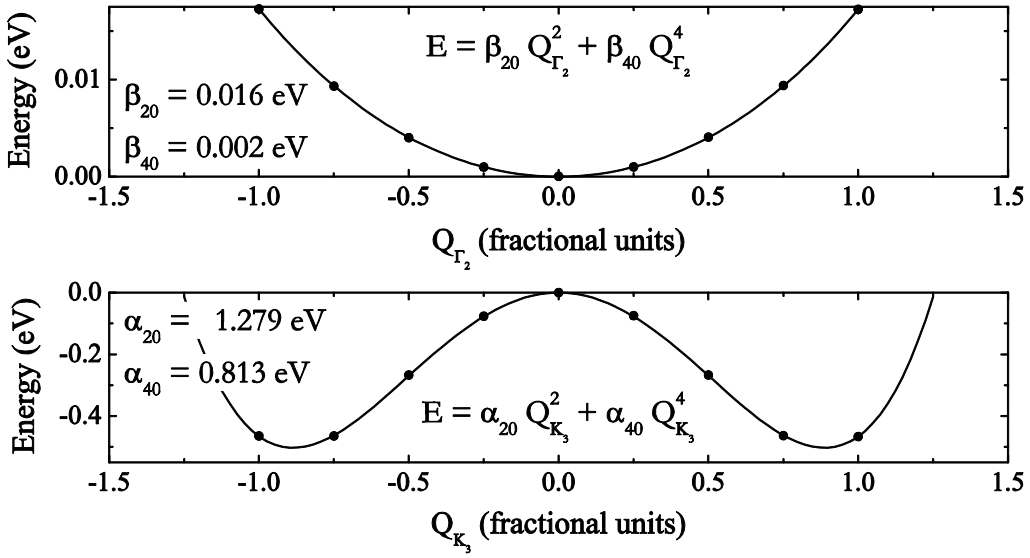

Figure 1.11 Energy as a function of Γ_2^- and K_3 mode amplitudes $Q_{\Gamma_2^-}$ (top) and Q_{K_3} (bottom) in the range of $[0,1]$ in fractional units, respectively (taken from Ref. [16]).

Then, Fennie and Rabe noticed, that the condensation of K_3 mode drives the single well of Γ_2^- mode to lower energy inducing a finite polarization as shown in Figure 1.12. This means that the polarization is directly related to the polar Γ_2^- mode (i.e. $\mathbf{P} \propto Q_{\Gamma_2^-}$) and can be calculated using the Berry phase formalism [7].

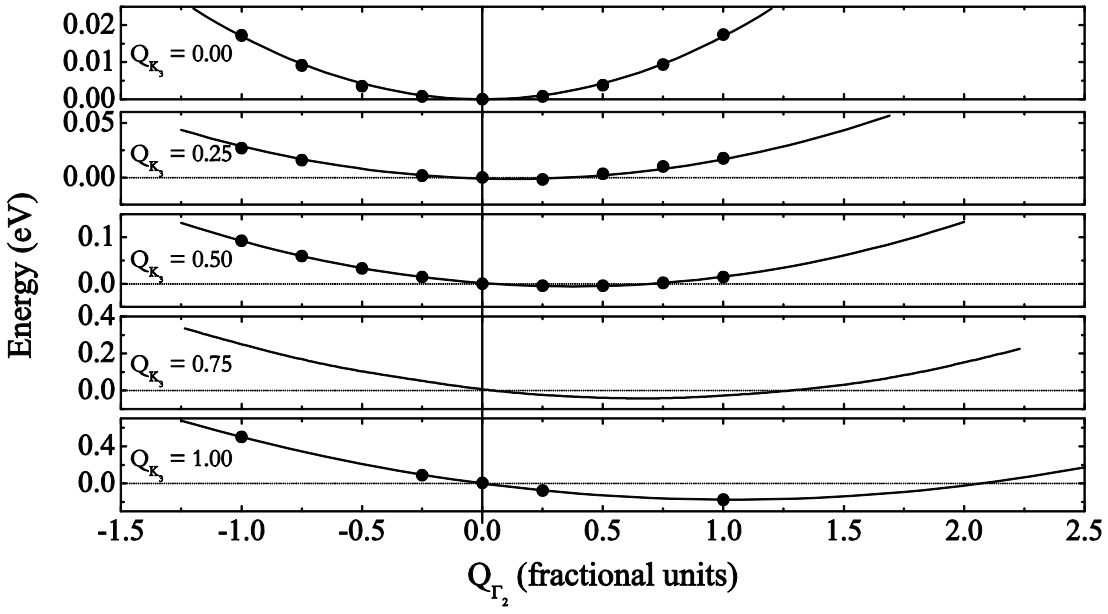

Figure 1.12 Energy as a function of Γ_2^- mode amplitude $Q_{\Gamma_2^-}$ at fixed K_3 mode amplitude Q_{K_3} in the range of $[0,1]$ in fractional units (taken from Ref. [16]).

Finally, the coupling of the unstable non-polar K_3 mode with the polar Γ_2^- mode by shifting the Γ_2^- mode from a zero to a non-zero equilibrium position is consistent with the presence of a linear term $Q_{K_3}^3 Q_{\Gamma_2^-}$ of K_3 and Γ_2^- modes in the energy expansion:

$$E[Q_{K_3}, Q_{\Gamma_2^-}] = \alpha_{20} Q_{K_3}^2 + \alpha_{40} Q_{K_3}^4 + \beta_{20} Q_{\Gamma_2^-}^2 + \beta_{40} Q_{\Gamma_2^-}^4 + \kappa_{310} Q_{K_3}^3 Q_{\Gamma_2^-} + \kappa_{220} Q_{K_3}^2 Q_{\Gamma_2^-}^2. \quad (1.9)$$

This linear term specifically identifies the improper ferroelectrics.

1.5.3 Non-collinear magnetic ordering

As introduced previously, hexagonal $YMnO_3$ is antiferromagnetic with a magnetic order present due to the magnetic Mn atoms. The optical second harmonic measurements determined the magnetic structure and observed a planar triangular arrangement of the Mn spins shown in Figure 1.13.

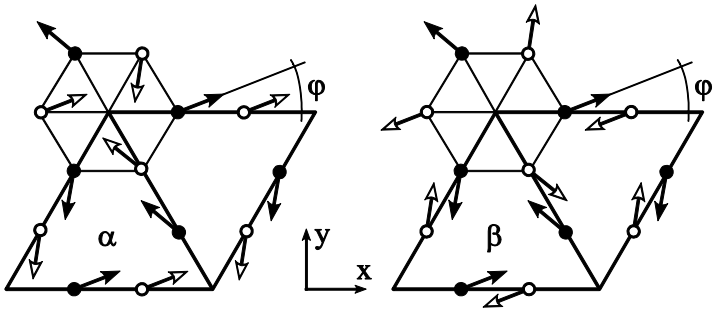

Figure 1.13 Planar triangular magnetic structures of hexagonal $RMnO_3$ manganites determined from optical second harmonic measurements. The parallel (model α) and antiparallel (model β) orientation in *xy* plane of the magnetic unit cell of Mn spins at $z = 0$ (closed arrows) and at $z = c/2$ (open arrows). (taken from Ref. [17]).

We have limited our first-principles studies to collinear magnetism considering a planar antiparallel magnetic ordering shown in Figure 1.14. The Mn spins in *xy* plane of the magnetic unit cell at $z = 0$ were oriented parallel up and in plane $z = c/2$ oriented parallel down. Each plane has a certain magnetic moment, but the total magnetic moment is equal to zero defining well the antiferromagnetic ordering of $YMnO_3$.

As it will be discussed in Chapter 3, our limitation to collinear magnetic ordering of Mn atoms might result in less well defined atomic position of Mn atom in the ferroelectric phase of $YMnO_3$. Although, a good agreement between our first-principles calculations discussed throughout this thesis and experimental data propose that it is reasonable to assume that most quantities (like geometry, Born effective charges, phonons, magnetic moments…) will not be significantly affected limiting ourselves to collinear magnetic ordering.

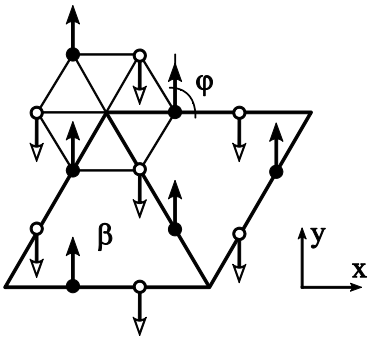

Figure 1.14 Planar antiparallel magnetic ordering in *xy* plane of the magnetic unit cell of Mn spins at $z = 0$ (closed arrows) and at $z = c/2$ (open arrows) considered in our first-principles calculations.

Chapter 2

Description of used techniques

This chapter provides a brief overview of techniques - theoretical as well as experimental - that we used to study the properties of hexagonal $YMnO_3$. The main concepts of theoretical technique - the first-principles calculations based on the density functional theory – are reviewed in the first section of this chapter. The second section is devoted to the main experimental techniques used in our study – Raman spectroscopy, liquid injection Metal Organic Chemical Vapor Deposition and X-ray diffraction.

2.1 First-principles calculations

2.1.1 Density functional theory

We performed our first-principles calculations using softwares based on the density functional theory (DFT) [18], which states that ground-state energy of the system of many interacting electrons might be formulated as a functional of the electronic density. The success of DFT included in close association with independent-particle approaches has led to widespread interest and became among the most popular and versatile methods available in the theory of

materials. The results obtained using this theory are usually in a good agreement with experimental values. Thus, later discussing our results in Chapter 3 and Chapter 4, we tend to compare our first-principles results with the experimental measurements available in the literature as well as with our own experimental studies.

2.1.1.1 General problem

In quantum mechanics, a solid can be considered as a system of nuclei and electrons interacting with each others. The system might be expressed through the Hamiltonian written as follows

$$H = T_N + T_e + V_{NN} + V_{ee} + V_{eN}, \tag{2.1}$$

The significance and mathematical form of each term is given in the following

- the kinetic energy of nuclei:

$$T_N = -\frac{\hbar^2}{2}\sum_I \frac{1}{M_I}\frac{\partial^2}{\partial \boldsymbol{R}_I^2} \tag{2.2}$$

- the kinetic energy of electrons:

$$T_e = -\frac{\hbar^2}{2m_e}\sum_i \frac{\partial^2}{\partial \boldsymbol{r}_i^2} \tag{2.3}$$

- the interaction between nuclei:

$$V_{NN} = \frac{e^2}{2}\sum_{I\neq J}\frac{Z_I Z_{II}}{\left\|\boldsymbol{R}_I - \boldsymbol{R}_J\right\|} \tag{2.4}$$

- the interaction between electrons:

$$V_{ee} = \frac{e^2}{2}\sum_{i\neq j}\frac{1}{\left\|\boldsymbol{r}_i - \boldsymbol{r}_j\right\|} \tag{2.5}$$

- the interaction between electrons and nuclei:

$$V_{eN} = -e^2 \sum_{iI} \frac{Z_I}{\left\| \boldsymbol{r}_i - R_J \right\|}, \tag{2.6}$$

where Z_I is the charge of nucleus I with mass M_I, m_e and $-e$ is the mass and elementary charge of the electron, $\boldsymbol{R} \equiv \boldsymbol{R}_I$ and $\boldsymbol{r} \equiv \boldsymbol{r}_i$ label the set of all nuclei $\boldsymbol{R}_I$ and electronic $\boldsymbol{r}_i$ coordinates, respectively.

The exact ground state can in principle be obtained by solving the corresponding Schrödinger equation

$$H\Psi = E\Psi, \tag{2.7}$$

where H is the Hamiltonian of the system, Ψ is the many-body wave function for all the particles and E is the corresponding energy.

But the problem is too complex to be solved in practice. The theory requires approximations in order to simplify and solve the problem.

2.1.1.2 The Born-Oppenheimer approximation

The Born-Oppenheimer approximation is based on the observations that $M_I \gg m_e$. This means that the kinetic energy of nuclei T_N can be neglected in Eq.2.1. Assuming $T_N \simeq 0$, there is no any differential operator acting on the positions of the nuclei, so that it becomes a parameter of the Hamiltonian. In other words, since the mass of the nuclei is much larger than the mass of the electrons, they are much slower and the electrons adiabatically adopt to nuclei positions. The Hamiltonian (Eq.2.1) simplifies to the expression written in the following

$$H_e = T_e + V_{NN} + V_{ee} + V_{eN}. \tag{2.8}$$

Although the problem is now reduced to the study of the interacting electrons in an external potential generated by the nuclei, the difficulty to obtain the direct solution remains due to the complexity of many-body wave function:

$$H_e \Psi_e = E_e \Psi_e. \tag{2.9}$$

Other simplifications are required to estimate the electronic interactions.

2.1.1.3 Kohn-Sham density functional theory

The most common implementation of DFT is through the Kohn-Sham approach [19] that maps the system of many interacting electrons on to a system of fictitious independent particles leading to the same ground-state density as the real system, which makes the problem possible to solve practically.

It can be shown that the electronic ground-state of the system is given minimizing self-consistently with respect to the density the following energy functional E_{KS} [20]:

$$E_{KS}\ \psi_i\ = -\frac{1}{2}\sum_i \langle \psi_i |\ \nabla^2\ | \psi_i \rangle + \frac{1}{2}\int \frac{n\ \boldsymbol{r}\ \ n\ \boldsymbol{r}'}{|\boldsymbol{r}-\boldsymbol{r}'|} d\boldsymbol{r} d\boldsymbol{r}' + E_{xc}\ \ n\ \ + \int V_{ext}\ \ \boldsymbol{r}\ \ \ n\ \ \boldsymbol{r}\ \ d\boldsymbol{r} + V_{NN}, \quad (2.10)$$

where the first term corresponds to the kinetic energy of independent electrons, the second term is the classical Coulomb energy (Hartree energy E_{Hartree}) of the electron density n r , the third term is the exchange and correlation energy E_{xc}, the fourth term is the energy of electrons in the external V_{ext} potential created by nuclei and the last term is the interaction between nuclei (see Eq.2.4). All these terms are well defined except the exchange-correlation functional $E_{xc}\ \ n$ that contains all the electronic interactions going beyond the classical Coulomb interaction E_{Hartree}. DFT is an exact theory: if the exact functional $E_{xc}\ \ n$ was known, then the exact ground-state energy and density of many interacting electrons problem would be provided by minimizing Eq.2.10. Unfortunately, although Kohn and Sham demonstrated the existence of such a functional, its far remains elusive and, in practice, calculations rely on approximate E_{xc}.

2.1.1.4 Functionals for exchange and correlation term

The most common approach to determine the exchange-correlation between interacting electrons is the local density approximation (LDA) (or more generally the local spin density

approximation (LSDA)), which locally substitutes the exchange-correlation energy density of the inhomogeneous system by that of a homogeneous electron gas evaluated at the local density:

$$E_{xc}^{LDA}\ n\ = \int \epsilon_{xc}^{\mathrm{hom}}\left[n\ \mathbf{r}\ \right] n\ \mathbf{r}\ \ d\mathbf{r}\,. \tag{2.11}$$

The exchange energy of the homogeneous gas $\epsilon_x^{\mathrm{hom}}$ is given by a simple analytic form:

$$\epsilon_x^{\mathrm{hom}}\ n\ = -\frac{3}{4\pi}\ 3\pi^2 n\ ^{1/3}. \tag{2.12}$$

While the correlation energy $\epsilon_c^{\mathrm{hom}}\ n$ has been fitted on Monte Carlo simulations on the homogeneous electron gas of different densities [21].

Semi-local generalized gradient approximations (GGA) are more evolved with marked improvements over LSDA as it also takes into account a dependence on the local density gradient [22,23]. The high accuracy of provided results has led to a wide use in the computational chemistry.

The most accurate are the hybrid functionals, which are essentially a combination of usual exchange-correlation functionals with a small percentage of exact exchange in order to go beyond the usual functionals and improve their deficiencies.

Throughout this thesis, we report in comparison both B1-WC hybrid functional [24] and LSDA+*U* [25] results.

2.1.1.5 LSDA+*U*

The LSDA calculations typically underestimate the lattice parameters by 1-2 % and phonon frequencies by 5% relative to the experimental values. Although, LSDA leads to significant underestimates of the band gap estimation. The LSDA+*U* functional has proved successful to open a band gap in a study of magnetic ferroelectric oxides. The Hubbard *U* term is often taken from constrained density functional calculations so that the theories do not contain adjustable parameters.

While $YMnO_3$ is an insulator with a band gap of 1.55 eV, it is described as a metal in LSDA calculations. In order to describe it as an insulating material, we used *U* term to open a band gap between the filled and empty 3d orbitals of Mn atoms. In this way, the LSDA-type calculations are coupled with orbital-dependent interaction. This additional interaction is usually considered only for high localized atomic-like orbitals on the same site.

2.1.2 Technical details

2.1.2.1 Structural optimization

Our first-principles calculations were performed with collinear magnetism within the LSDA+*U* as implemented in the ABINIT code [26] and within the B1-WC hybrid scheme [24] using the CRYSTAL code [27].

In ABINIT calculations, we used the projector augmented-wave (PAW) approach with atomic data generated by N. Holzwarth and coworkers [28,29]. The cutoff radius R_c was 2.0 Bohr for Y, 1.9 Bohr for Mn and 1.0 Bohr for O. We used the Perdew-Wang parameterization of LSDA [30] and the LSDA+*U* formalism of Liechtenstein *et al*. [25]. The values of Hubbard *U* term $U = 8$ eV and exchange parameter $J = 0.88$ eV, obtained by Medvedeva et *al*. [31] from constrained LSDA supercell calculations [32,33], were applied to Mn d orbitals. The evolution of the band gap E_{gap} and magnetic moment μ_B of Mn atoms in term of *U* will be discussed in Chapter 3. The wavefunctions were expanded in plane waves up to a kinetic energy cutoff of 35 Ha (Figure 2.1). The sufficiently large PAW energy cutoff for the double grid was of 50 Ha. Integrals over the Brillouin zone were approximated by sums on a 4 x 4 x 2 (for $P6_3cm$ 30 atom cell) and 6 x 6 x 2 (for $P6_3/mmc$ 10 atom cell) *k*-point mesh (Figure 2.2). The self-consistent cycles were converged up to tolerances of 10^{-8} Ha / Bohr on the difference of forces for the electronic degrees of freedom and of 10^{-7} Ha / Bohr on the maximal forces for the structural relaxations. The energy cutoff, *k*-point mesh and convergence criteria were optimized to reach good convergence of phonon frequencies.

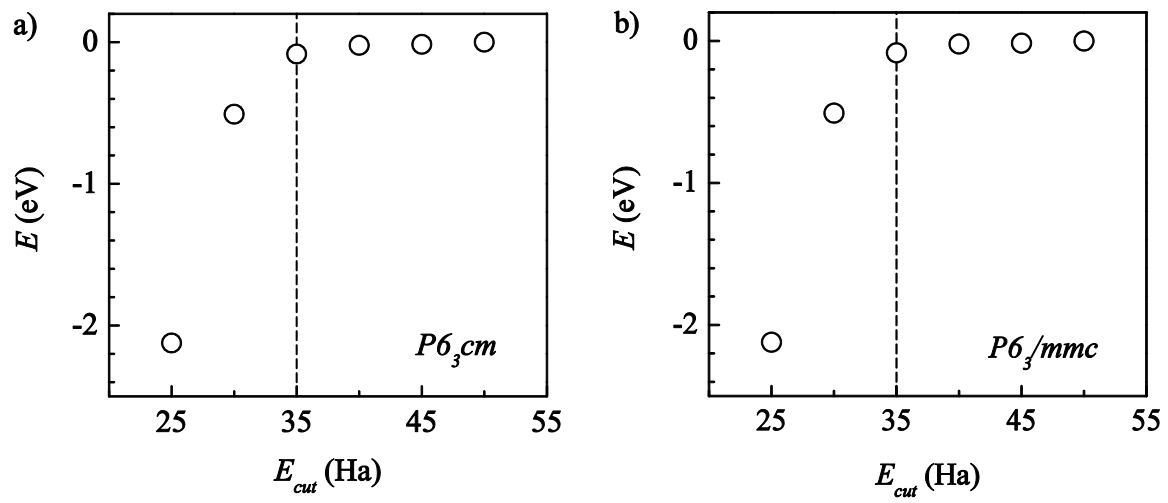

Figure 2.1 LSDA+*U* total energy *E* per $YMnO_3$ formula units (5 atoms) as a function of the energy cut-off E_{cut} for a) *P6₃cm* and b) *P6₃/mmc* phases.

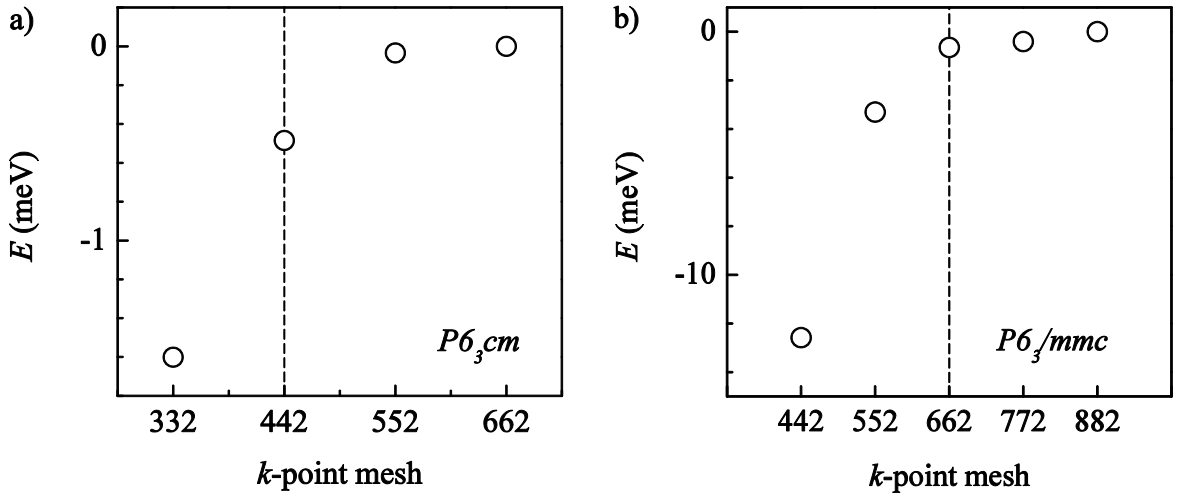

Figure 2.2 LSDA+*U* total energy *E* per $YMnO_3$ formula units (5 atoms) as a function of the *k*-point mesh for a) *P6₃cm* and b) *P6₃/mmc* phases.

In CRYSTAL calculations, we used a linear combination of atomic orbitals (LCAO) approach and localized Gaussian basis sets for Y [34], Mn [35] and O [36]. For Y^{3+} ion, the outermost 6sp, 7sp, and 8sp shells of the Y free atom were not considered. The Gaussian exponents of the outermost 5sp, 5d shells and the scale factor of 4d shell were optimized in $YMnO_3$ ferroelectric phase considering antiferromagnetic (AFM) order for Mn spins. The values for the optimized exponents of 5sp, 5d shells and the scale factor of 4d shell are 0.2633225,

0.1171919 and 1.0086, respectively. For Mn^{3+} ion the optimized values for the exponent of 4d shell and the scale factor of 3d shell are 0.259 and 1.02, respectively. Brillouin zone integrations were performed using a 4 x 4 x 2 mesh (for $P6_3cm$ 30 atom cell) of *k*-points. The self-consistent calculations were considered to be converged when the energy changes between interactions were smaller than 10^{-14} Ha. An extralarge predefined pruned grid consisting of 75 radial points and 974 angular points was used for the numerical integration of charge density. We performed full optimization of the lattice constants and atomic positions. The optimization convergence of 2.5×10^{-5} Ha / Bohr in the root-mean square values of forces and 6×10^{-5} Bohr in the root-mean square values of atomic displacements was simultaneously achieved. The level of accuracy in evaluating the Coulomb and exchange series is controlled by five parameters [27]. The values used in our calculations are 7, 7, 7, 7, and 14.

All calculations were performed at 0 K for a A-type AFM order.

2.1.2.2 Phonon calculations

Phonon calculations were done in a frozen phonon framework. Hessian matrix was built by displacing the atom by ~ 0.0028 Å (for ABINIT) and 0.003 Å (for CRYSTAL) in the primitive cell and calculating the forces on all the atoms in the unit cell. Positive and negative displacements were considered in order to minimize the influence of the anharmonic effects. The amplitude of displacement was chosen as a compromise in order to minimize the numerical errors, while staying close to the linear response regime. Dynamical matrix was built from the Hessian one and we used PHON code [37] to compute the frequencies of TO modes. The nonanalytical term [38] was calculated and added to the dynamical matrix in order to determine the frequencies of LO modes and calculate the angular dispersion curves of oblique phonon modes (see Section 4.2.3.2). The acoustic modes were set to zero by reimposing the acoustic sum rule.

In all cases, phonon calculations were performed at the theoretically optimized lattice parameters reported in Chapter 3. Although this choice is the most consistent from the theoretical point of view, inaccuracies on the structure can have a direct impact on the phonon

frequencies and the correct prediction of lattice parameters becomes a critical issue in the calculation, as further discussed in the next section.

The Born effective charges for the ferroelectric $YMnO_3$ were calculated with ABINIT using the Berry phase approach [7] by displacing the atom by ~ 0.005 Å along the crystal axes and calculating the induced polarization. Positive and negative displacements were considered in order to minimize the influence of the anharmonic effects. The acoustic sum rule gives values smaller than $0.01\,e^-$.

2.2 Experimental techniques

2.2.1 Raman spectroscopy

2.2.1.1 Introduction

In our work, the phonon frequencies were obtained using one of the main methods – Raman spectroscopy. This technique enables to observe how the light interacts with condensed matter. It may be reflected, absorbed or scattered in some manner. The general explanation of the Raman effect is that the incident light with a certain frequency ω_i interacts with the lattice vibrations (phonons) and the energy $\hbar\omega$ gained or lost by the lattice is compensated by a decrease or increase in the frequency ω_s of the scattered light ($\omega_s = \omega_i \pm \omega$) [39].

We measured our polarized Raman spectra using the Porto notation:

$$k_i \;\; E_i E_s \;\; k_s, \tag{2.13}$$

where k_i and k_s are the wavevectors of incident and scattered light, E_i and E_s are the electric polarization of incident and scattered light, respectively. In case of back-scattering

experimental setup, k_s corresponds to $\bar{k}_s$; the underline means that the direction of scattered light is reversed by 180° respect to incident light direction (Figure 2.3).

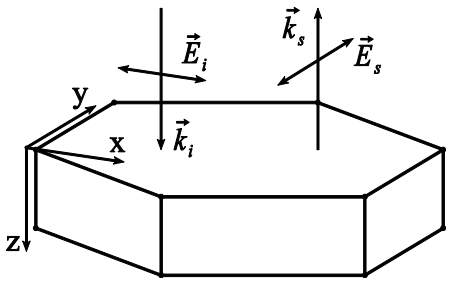

Figure 2.3 An example of Porto notation $z(xy)\bar{z}$: the wavevector of incident light k_i is directed along *z* direction and the wavevector of back-scattered light k_s is collected along *z*-axis direction, the polarization of incident light is aligned along *x*-axis and the polarization of back-scattered light is collected aligned along *y*-axis. x, y and z are the axes of the Cartesian coordinate system.

We identified the phonon symmetries from the Raman tensors, which in case of hexagonal $YMnO_3$ (space group: $P6_3cm$) are written as follows

$$A_1\ z = \begin{pmatrix} a & 0 & 0 \\ 0 & a & 0 \\ 0 & 0 & b \end{pmatrix},\quad E_1\ y = \begin{pmatrix} 0 & 0 & 0 \\ 0 & 0 & c \\ 0 & c & 0 \end{pmatrix},\quad E_1\ -x = \begin{pmatrix} 0 & 0 & -c \\ 0 & 0 & 0 \\ -c & 0 & 0 \end{pmatrix},$$

$$E_2 = \begin{pmatrix} 0 & d & 0 \\ d & 0 & 0 \\ 0 & 0 & 0 \end{pmatrix},\quad E_2 = \begin{pmatrix} d & 0 & 0 \\ 0 & -d & 0 \\ 0 & 0 & 0 \end{pmatrix}.$$

The allowed phonon symmetries in $YMnO_3$, labeled with Porto notation, for Raman scattering are summarized and discussed in Section 4.2.3.1 in Chapter 4.

2.2.1.2 Technical details

Our Raman spectra were recorded with a LabRam Jobin-Yvon spectrometer equipped with a liquid-nitrogen-cooled charge-coupled-device (CCD) detector. The 514 nm line of an Ar^+ ion laser was used as an excitation wavelength. The light was focused to a 1 μm^2 spot using a $\times$ 100 objective at room temperature. The material is sensitive to the laser power (heating effects), thus the experiments were carried out using an incident power less than 0.5 mW to avoid overheating of the crystal. The signal of each spectrum was accumulated 2000 s twice. All measurements, performed under the microscope, were recorded in a back-scattering geometry; the instrumental resolution was 2.8 ± 0.2 cm^{-1}.

2.2.2 Liquid injection MOCVD

2.2.2.1 Introduction

Our epitaxial thin films of hexagonal $YMnO_3$ were grown using liquid injection Metal Organic Chemical Vapour Deposition (MOCVD). CVD is a deposition process in which a solid film is formed from a gas phase *via* chemical reactions taking place in heterogeneous phase (i.e. reactions occur on a surface, not in the gas phase). All by-products of the reactions should be gaseous and are evacuated.

The volatile compounds (precursors) containing the constituent atoms of the grown material in the gas phase are transported to the chamber by a carrier neutral gas (Ar gas in our case).

When the precursors are liquid or solid, the gas phase has to be created by evaporating the precursors. This is the case for complex oxide deposition. A major difficulty for the CVD of complex oxides is to create a stable gas phase while the precursors are not very volatile and are, moreover, thermally unstable. If they are heated for a prolonged time in bubblers (which is a classical way to evaporate liquid precursors), they degrade and the cationic composition drifts. In order to solve this issue, the LMGP has designed an injector liquid source, that has been patented by CNRS [40]. It is based on the sequential injection of micro-amounts of

liquid precursors into an evaporator where "flash" volatilisation occurs. The flash volatilization ensures that the precursors do not degrade before volatilization.

The liquid solution of precursors is injected with an injector of the same type as those used for the fuel injection in thermal motors. It is a high-speed reliable electrovalve driven by computer. The liquid is kept in a closed vessel, pressurized under few bars of argon. The reactive species flow rate created in the evaporator depends on the electrical pulse width, which defines the volume of the droplets (typically of the order of a few milligrams) on the injection frequency of the microvalve, on the viscosity and concentration of the liquid solution and on the differential pressure between the reservoir and the evaporator.

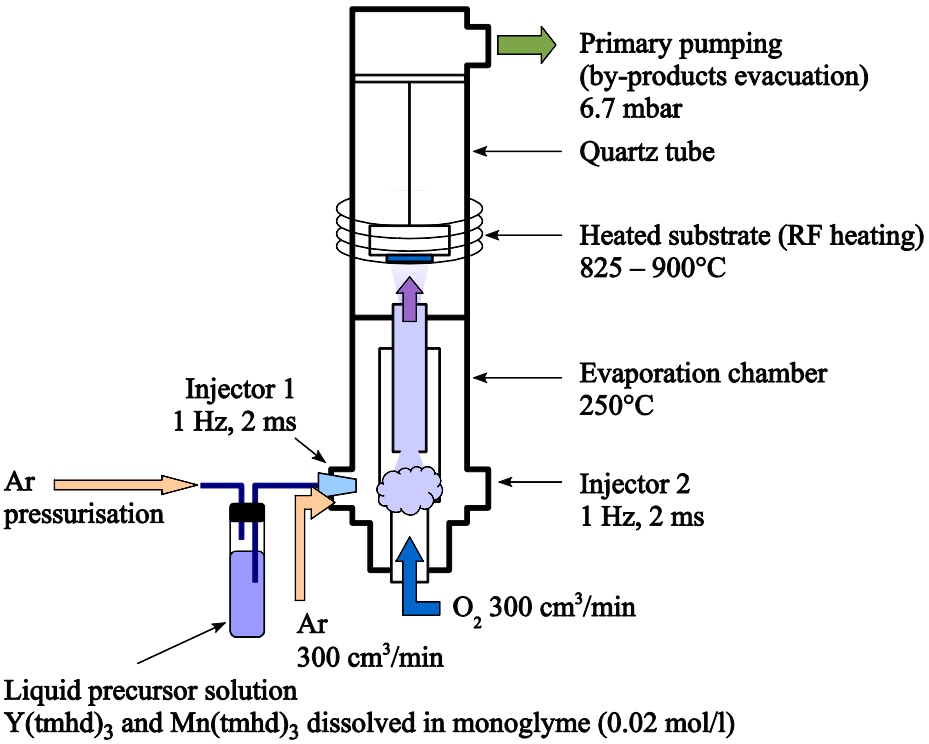

Figure 2.4 Schema of liquid injection MOCVD (taken from Ref. [41]).

The deposition of complex oxides is realized either by injecting each precursor separately or by using a single injector fed with a mixture of the different precursors. This is the later case that we used.

Figure 2.4 illustrates our liquid injection MOCVD reactor used for the growth of epitaxial thin films of hexagonal $YMnO_3$ on YSZ (111) substrates.

The reactor consists of three main parts:

- liquid injection source: an injector with the liquid precursor solution, the cooling system in order to avoid overheating of the injector and the evaporation chamber, in which the liquid is injected to be flash volatilized. The carrier gas flow rate is regulated using a mass flow meter.

- growth chamber: a vertical quartz tube and a stainless steel substrate holder with a hot-wall type configuration. The cylindrical hot wall is heated by radio frequency (RF) inductive currents and the substrate holder is heated mostly by radiation. The temperature of the substrate holder is regulated. Di-oxygen is induced in the deposition chamber (here *via* the evaporator) and the flow rate is regulated using a mass flow meter. The total pressure is regulated using a butterfly valve.

- evacuation: a primary pump and a cold trap using liquid nitrogen to condense the residual decomposition compounds to avoid contamination of the vacuum pump.

2.2.2.2 Technical details

The growth parameters of our epitaxial thin films of hexagonal $YMnO_3$ on YSZ (111) substrates by liquid injection MOCVD are listed in Table 2.1.

The metalorganic volatile precursors were $Y(tmhd)_3$ and $Mn(tmhd)_3$, where tmhd stands for 2,2,6,6-tetramethyl-3,5-heptane-dionate. The precursors were solid at room temperature and were dissolved in monoglyme solvent (1,2-dimethoxyethane), in concentration of 0.02 mol/l. Both precursors were mixed in a unique solution to deposit $YMnO_3$. The precursors were provided by SAFC Hitech [42] within the framework of the European MaCoMuFi STREP project.

Each growth of thin film was followed by an *in situ* annealing at the growth temperature for 15 minutes in 1 bar of oxygen to fully oxygenate the film.

Solution	Precursor	$Y(tmhd)_3$, $Mn(tmhd)_3$
	Solvant	monoglyme
	Concentration	0.02 mol/l
	Composition n_Y / n_{Mn}	**0.8 – 1.2**
Temperature	Zone of injection	250 °C
	Zone of evaporation	250 °C
	Zone of growth	**825 – 900 °C**
Environment in growth chamber	Pressure	6.7 mbar
	Flow of O_2	300 cm^3/min
	Flow of Ar	300 cm^3/min
Injection parameters	Opening time of injector	2 ms
	Frequency of injections	1 Hz
	Mass of one injection	~ 2 - 4 mg
Annealing	Pressure	1 bar
	Temperature	825 – 900 °C
	Time	15 min

Table 2.1 Growth parameters of the hexagonal $YMnO_3$ by liquid injection MOCVD. The optimized parameters in this work are marked in bold. Annealing was performed at growth temperature.

2.2.3 X-Ray diffraction

2.2.3.1 Introduction

We performed the structural characterizations of our grown $YMnO_3$ films using X-Ray diffraction (XRD) technique.

XRD diffraction is a non-destructive analytical technique, which provides the information about the crystalline structure of material. This technique is based on the observation of scattered intensity of an X-ray beam by the atoms of the crystal. X-rays are electromagnetic radiation with wavelengths (in the range 0.5 - 2.5 Å) of the same order of magnitude as the interatomic distances in solids.

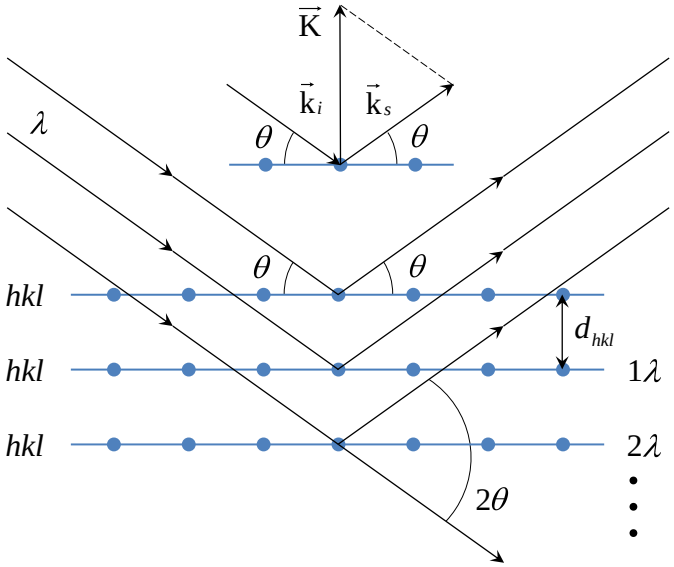

Figure 2.5 Diffraction condition. λ and θ, a wavelength and an angle of incident X-ray beam, respectively; d_{hkl}, a distance between *hkl* lattice planes; K, a scattering vector defined as $K = k_s - k_i$, with the wavevectors of incident k_i and scattered k_s X-rays; n, a diffraction order (integer).

When the incident X-ray beam arrives to a crystal, it is scattered in all directions by the atoms of crystal. In some directions, the increased intensity of scattered beam is observed due to the constructive interference of the scattered waves.

Figure 2.5 illustrates the conditions for a constructive interference of the X-ray beam of wavelength λ incident on the crystal at an angle θ and scattered from the *hkl* lattice planes with interplanar distance d_{hkl}. The constructive interference is observed when (i) the X-rays are reflected from the lattice planes at the specular angle, (ii) the path length difference between X-rays scattered from different *hkl*-planes is an integer (n) times the wavelength and (iii) the scattering vector K is parallel to the normal of the *hkl*-planes. The diffraction condition is summarized in the Bragg law:

$$n\lambda = 2d_{hkl}\sin\theta \quad . \tag{2.14}$$

Depending on a chosen X-ray setup, the different structural properties of the crystal might be investigated.

We used $\theta / 2\theta$ locked coupled scan in Brag-Brentano geometry to determine the nature of crystalline phases present in films (secondary phases), the preference crystalline orientation of films and the out-of plane *c*-lattice parameter.

Then, we performed the rocking curve scans in order to determine the mean spread of *c*-axis orientation.

2.2.3.2 Technical details

We performed the XRD measurements of our $YMnO_3$ films using Siemens D500 diffractometer: with the Cu-$K_{\alpha 1}$ line with wavelength λ_{Cu} = 0.154056 nm for $\theta / 2\theta$ scans (the radiation of Cu-K_β line was eliminated by germanium monochromator, the Cu-$K_{\alpha 2}$ line much less intense than Cu-$K_{\alpha 1}$ line) and with the Fe-$(2K_{\alpha 1}+K_{\alpha 2})/3$ lines with average wavelength λ_{Fe} = 0.19373 nm for rocking curve scans (the fluorescence and the radiation of Fe- K_β line was eliminated by graphite monochromator).

For $\theta / 2\theta$ locked coupled scan, the X-ray tube was set at a tension of 40 kV and a current of 30 mA. The scattering angle was between 2θ = 10° and 2θ = 90°with step of 0.04 °. At each angle the signal was collected between 8 to 40 s. The samples were tilted by 0.3° in order to avoid the saturation of the detector because of the intense scattering coming the single crystalline substrate. For *c*-lattice parameter determination, the scattering angle was between 2θ = 58° and 2θ = 68° (to measure 004 reflection of $YMnO_3$ film and 222 reflection of YSZ substrate) with step of 0.02°. The crystalline phases and their orientations present in samples were identified from the angle of diffraction 2θ using The International Centre for Diffraction Data (ICDD).

For rocking curve scan, the X-ray tube was set at a tension of 40 kV and a current of 35 mA. The angle θ was varied between 17.5° and 22° with step of 0.01° and counting time between 10 and 40 s for 2θ = 39.7° (to measure the most intense 004 reflection of $YMnO_3$). Two slits of 0.1° before sample and two slits of 0.1° and 0.05° after sample were used to achieve higher resolution.

Chapter 3

Structural properties of $YMnO_3$

The ground-state structure of hexagonal $YMnO_3$ is ferroelectric and belongs to the space group *P6$_3$cm* stable below ~ 1270 K [11]. At high temperature, $YMnO_3$ undergoes a structural phase transition and crystallizes into a paraelectric *P6$_3$/mmc* structure.

This chapter overviews the structural properties of both phases of hexagonal $YMnO_3$. Our theoretical lattice parameters, atomic positions, band gap and local magnetic moment of Mn atoms are discussed in comparison to other theoretical and experimental values available in the literature.

3.1 Ferroelectric phase *P6$_3$cm*

The ground-state structure of $YMnO_3$ is shown in Figure 3.1. This ferroelectric phase of space group *P6$_3$cm* contains six formula units (30 atoms) in its primitive unit cell. Two inequivalent Y_1 and Y_2 atoms form layers in between the MnO_5 triangular bipyramids tilted with respect to *c*-axis. Equivalent Mn atoms are surrounded by non-equivalent oxygen atoms - apical O_1, O_2 and planar O_3, O_4. Table 3.1 lists the generic atomic positions in reduced coordinates. The displacement δ indicates the magnitude of the distortion with respect to the high-symmetry

position occupied in the *P6₃/mmc* paraelectric phase (see section 3.2). The oxygen atoms O_1 and O_2 have a degree of freedom along *c*-axis in both phases and their position in the ferroelectric phase are noted as z_{O1} and z_{O2}. The origin in the *ab* plane is set to the Y_1 atom while the origin along *c* is set to the Mn atom.

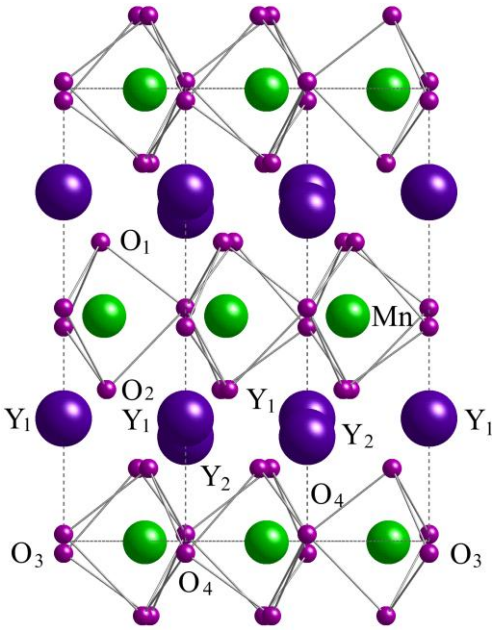

Figure 3.1 Structure of the *P6₃cm* ferroelectric $YMnO_3$. The view plane is (010).

Atom	Wyckoff	Position
Y_1	2a	$(0, 0, 1/4 + \delta_{Y1})$
Y_2	4b	$(1/3, 2/3, 1/4 - \delta_{Y2})$
Mn	6c	$(1/3 + \delta_{Mn}, 0, 0)$
O_1	6c	$(1/3 - \delta_{O1}, 0, z_{O1})$
O_2	6c	$(1/3 + \delta_{O2}, 0, z_{O2})$
O_3	2a	$(0, 0, 0 + \delta_{O3})$
O_4	4b	$(1/3, 2/3, 0 + \delta_{O4})$

Table 3.1 Generic atomic positions in the *P6₃cm* ferroelectric phase of $YMnO_3$.

	Theory			Experiment						
	LSDA+*U* present	B1-WC present	LSDA+*U* [16]	3 K [12]	RT [12]	RT [43]	RT [44]	RT [45]	RT [46]	RT [47]
a (Å)	6.085	6.144	6.099	6.121	6.138	6.147	6.139	6.155	6.148	6.148
c (Å)	11.340	11.323	11.42	11.408	11.396	11.437	11.407	11.403	11.443	11.399
δ_{Y1}	0.0251	0.0253	0.0251	0.0260	0.0220	0.0235	0.0243	0.0189	0.0189	0.021
δ_{Y2}	0.0188	0.0190	0.0187	0.0185	0.0180	0.0172	0.0165	0.0210	0.0206	0.019
δ_{Mn}	0.0002	0.0003	0.0001	0.0107	0.0004	-0.0005	0.0019	-0.0125	-0.010	0.016
δ_{O1}	0.0271	0.0258	0.0275	0.0328	0.0253	0.030	0.0250	0.0233	0.008	0.040
z_{O1}	0.1635	0.1636	0.1642	0.1602	0.1620	0.163	0.1627	0.1621	0.163	0.152
δ_{O2}	0.0264	0.0250	0.0268	0.0275	0.0265	0.020	0.0254	0.0278	0.038	0.010
z_{O2}	-0.1634	-0.1634	-0.1641	-0.1658	-0.1636	-0.1624	-0.1628	-0.1633	-0.162	-0.173
δ_{O3}	-0.0237	-0.0226	-0.0242	-0.0205	-0.0250	-0.024	-0.0218	-0.0255	-0.016	-0.018
δ_{O4}	0.0203	0.0194	0.0207	0.0182	0.0155	0.017	0.0186	0.0133	0.022	0.023

Table 3.2 Lattice parameters and atomic positions (see notations in Table 3.1) in the $P6_3cm$ ferroelectric phase of $YMnO_3$. Comparison of the theoretical results obtained from first-principles (LSDA+*U* and B1-WC) with the experimental data at room temperature (RT) and 3 K.

In Table 3.2, we report our calculated LSDA+*U* and B1-WC structural parameters (lattice parameters and atomic positions as defined in Table 3.1) in comparison to previous theoretical and experimental values. We compare our results to the theoretical structure obtained within the LSDA+*U* approximation using VASP package by Fennie and Rabe [16] and a variety of experimental structural refinements [12,43,44,45,46,47]. Most referred experimental data are obtained at room temperature (paramagnetic order). Only Ref. [12] gives the measured parameters at 3 K (AFM order) and should better compare to our calculations.

LSDA+*U* lattice parameters are in good agreement with the data from Fennie and Rabe and reproduce the experimental values at 3 K within ≈ 0.6 %. B1-WC hybrid functional gives a good *c*-lattice parameter as well, but slightly overestimates the *a*-lattice parameter, which

appears closer to the one reported at room temperature rather than to the one at low temperature.

Our calculated atomic positions using both LSDA+*U* and B1-WC correspond very well to the computed Fennie and Rabe data. The standard deviation σ of all theoretical predictions reported in Table 3.2 is small and of the order of $1x10^{-4}$ for δ_{Y1}, δ_{Y2}, δ_{Mn}, $3x10^{-4}$ for z_{O1}, z_{O2} and $7x10^{-4}$ for δ_{O1}, δ_{O2}, δ_{O3} and δ_{O4}. The experimental refinements of atomic positions reported in the literature are more widely dispersed. The standard deviation of the values reported in Table 3.2 is larger than $1x10^{-3}$ (comparing Ref. [12], [43], [44]) and goes up to $1x10^{-2}$ (including the values of Ref. [45], [46], [47]). Most reported values from Ref. [45], [46], [47] are far from the average values from Ref. [12], [43], [44]. Thus we tend to compare our results to Ref. [12], [43], [44] that are actually in good agreement with each others. As for theoretical data, the most dispersed experimental values are those of the atomic positions of O_1, O_2 in *ab* plane and O_3, O_4 along *c*-axis.

We notice that our calculations do not predict well the position of the Mn atom. The low temperature data show that this atom moves drastically away from its room-temperature position when going below the Néel temperature, T_N = 75 K [12]. This suggests that this position could be strongly dependent on the magnetic order. It might therefore be important to go beyond collinear magnetism and to treat more properly the triangular arrangement of Mn spins in order to achieve a better description of the Mn position. The only attempt in this direction has been reported by Zhong et *al.* [48]. Their results are quite different from others, but they clearly do not compare better with experiment.

From a more technical point of view, LSDA calculations do not describe $YMnO_3$ as an insulating material, which requires to include a Coulomb interaction correction *U* for Mn atoms. $YMnO_3$ becomes an insulator for $U > 4.7$ eV (rather independently of *J*) and, as expected, the band gap grows with increasing *U* (Figure 3.2, a). We used the values of $U = 8$ eV and $J = 0.88$ eV [49] that were obtained from the constrained LSDA supercell calculations [32,33] and that opens a band gap equal to 1.17 eV. In comparison, B1-WC hybrid functional estimates the band gap at a very similar value of 1.0 eV, that reasonably agrees with the experimental one (1.55 eV) measured at 3 K [50]. The local magnetic moment of Mn atoms also depends on the Hubbard *U* correction (Figure 3.2, b). It grows when *U*

increases, typically overestimating the experimental magnetic moment of 3.09 μ_B measured at 1.5 K [51]. Our LSDA+U calculations (U = 8 eV, J = 0.88 eV) predict a value of 3.68 μ_B and B1-WC gives a magnetic moment equal to 3.85 μ_B. In conclusion, there is no magic approach providing exact description together of the band gap and of the magnetic moment, but LSDA+U (with calculated U and J) and B1-WC are good compromises that yield simultaneously band gap and magnetic moment in satisfactory agreement with experimental values.

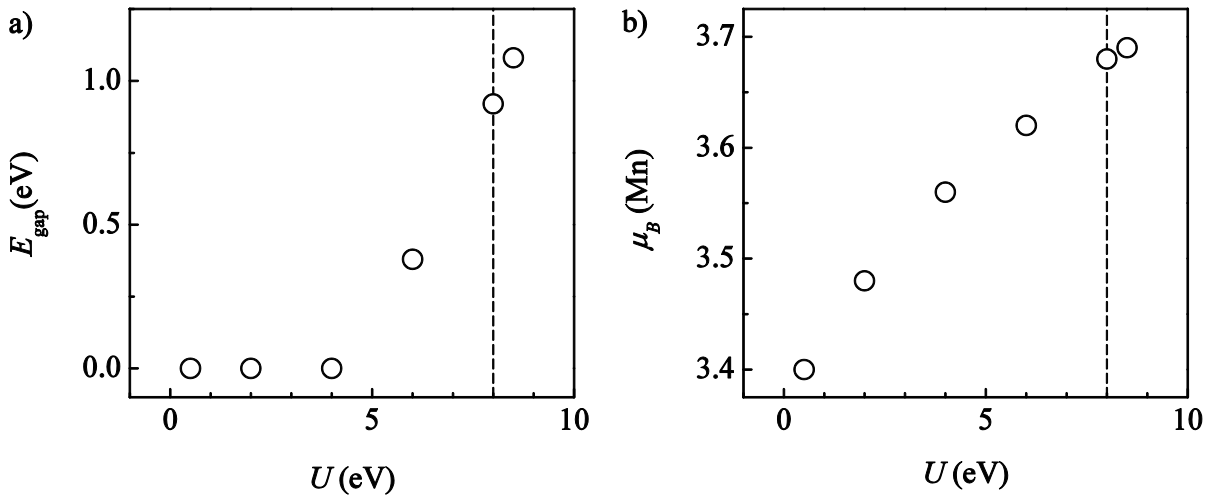

Figure 3.2 LSDA+U band gap E_{gap} (a) and magnetic moment μ_B of Mn atoms (b) dependence on U term (J is set to a typical value of 10% of U) in the paraelectric *P6₃/mmc* phase of $YMnO_3$.

3.2 Paraelectric phase *P6₃/mmc*

The primitive unit cell of the paraelectric *P6₃/mmc* phase shown in Figure 3.3 is smaller and has less ionic degrees of freedom than the unit cell of the ferroelectric *P6₃cm* phase. The non-distorted paraelectric structure contains two formula units (10 atoms) and has one Wyckoff site for Y and Mn, two inequivalent sites for oxygen atoms: apical O_{ap} and plane O_{pl}. The

Table 3.3 lists the generic atomic positions in reduced coordinates. All atoms are fixed by symmetry except the oxygen atom defined as O_{ap} (1/3, 2/3, z_{Oap}) that has a degree of freedom z_{Oap} along *c*-axis.

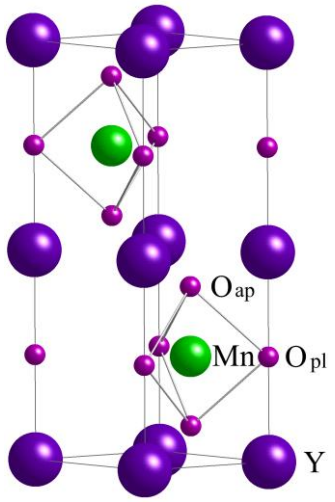

Figure 3.3 Structure of the *P6₃/mmc* paraelectric $YMnO_3$.

Atom	Wyckoff	Position
Y	2a	(0, 0, 0)
Mn	2d	(1/3, 2/3, 3/4)
O_{ap}	4f	(1/3, 2/3, z_{Oap})
O_{pl}	2b	(0, 0, 1/4)

Table 3.3 Generic atomic positions in the *P6₃/mmc* paraelectric phase of $YMnO_3$.

Table 3.4 shows the LSDA+*U* lattice parameters and atomic position of oxygen atom z_{Oap} of *P6₃/mmc* paraelectric $YMnO_3$ (as defined in Table 3.3) in comparison to the available theoretical and experimental data. We compare our results to the theoretical structure obtained within the LSDA+*U* approximation using VASP package by Fennie and Rabe [52]. Note that

the calculations are performed at 0 K (AFM order) and experimental values are measured at 1285 K [53] and 1373 K [43] (paramagnetic order), respectively.

	Theory		Experiment	
	ABINIT	VASP [52]	1285 K [53]	1373 K [43]
a (Å)	3.555	3.561	3.61	3.622
c (Å)	11.11	11.23	11.39	11.34
zOap	-0.0838	-0.0834	-0.0873	-0.0821

Table 3.4 Lattice parameters *a* and *c* in angstroms, atomic position z_{Oap} (see notation in Table 3.3) in reduced coordinates in the *P6₃/mmc* paraelectric phase of $YMnO_3$. Comparison of theoretical results obtained from first principles (LSDA+*U*) and experimental data.

Our LSDA+*U* *a*-lattice parameter and z_{Oap} atomic position are in good agreement with Fennie and Rabe data (Table 3.4). The *c*-lattice parameter obtained by ABINIT code is smaller than the one by VASP package, but both values agree with each other within ≈ 1%. Our calculated structure at 0 K reproduces reasonably well (within ≈ 2.5 %) the experimental values measured at high temperature.

The Figure 3.4 shows the primitive cell (10 atoms) and in-plane tripled cell (30 atoms) of *P6₃/mmc* paraelectric phase of $YMnO_3$. The primitive cell drawn in the plane of Y atoms in red is tripled along in-plane diagonal *x*, *y*. The triple cell with axes *x'*, *y'* is drawn in blue. The *a*-lattice parameter differs by a factor of $\sqrt{3}$: a_{PE} = 3.555 Å (paraelectric simple, Table 3.4) and a_{PEt} = 6.158 Å (paraelectric triple). The *c*-lattice parameter for both cells remains unchanged $c_{PE} = c_{PEt}$ =11.11 Å (Table 3.4).

The Table 3.5 gives the correspondance of atomic positions in the *P6₃/mmc* paraelectric primitive and triple cell in reduced coordinates. The Wyckoff positions of atoms in the triple paraelectric phase are the same as in the ground state ferroelectric $YMnO_3$ (see positions in Table 3.1). As in the *P6₃/mmc* primitive paraelectric phase, all atoms remain fixed by the symmetry except the apical oxygen atoms O_{ap1} and O_{ap2} that have a degree of freedom along

c-axis noted as z_{Oap}. We optimized the z_{Oap} value in the triple cell. The position in the *P6₃/mmc* simple and triple cell is equal to z_{Oap} = -0.0837896 (the same value as in Table 3.4) and z_{Oap} = -0.0837801, respectively. The difference between two values is of order of $1x10^{-5}$. The origin in the *ab* plane and along *c*-axis is set to the plane oxygen O_{pl3}.

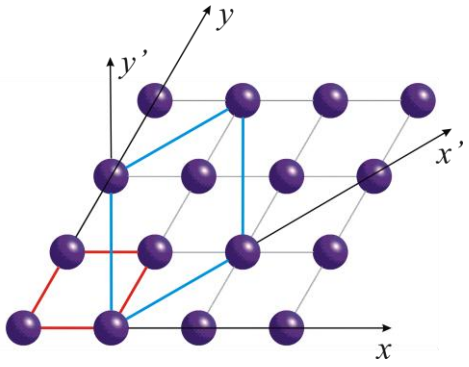

Figure 3.4 Connection between the crystal axes: *x*, *y* of *P6₃/mmc* primitive paraelectric phase (red line) and *x'*, *y'* of the *P6₃/mmc* triple paraelectric phase (blue line). The view plane is Y atoms (001).

Atom	Wyckoff	*P6₃/mmc* simple	Wyckoff	*P6₃/mmc* triple
Y_1	2a	(0, 0, 1/2)	2a	(0, 0, 1/4)
Y_2	2a	(0, 0, 0)	4b	(1/3, 2/3, 1/4)
Mn	2d	(2/3, 1/3, 1/4)	6c	(1/3, 0, 0)
O_{ap1}	4f	(1/3, 2/3, z_{Oap}+1/2)	6c	(1/3, 0, z_{Oap}+1/4)
O_{ap2}	4f	(2/3, 1/3, -z_{Oap}+1/2)	6c	(1/3, 0, -z_{Oap}-1/4)
O_{pl3}	2b	(0, 0, 3/4)	2a	(0, 0, 0)
O_{pl4}	2b	(0, 0, 1/4)	4b	(1/3, 2/3, 0)

Table 3.5 Correspondence of the generic atomic positions (see notations in Table 3.3) of *P6₃/mmc* primitive and triple paraelectric phases of $YMnO_3$.

As discussed in the previous section, the LSDA+*U* calculations are required to open a band gap and to have an insulating $YMnO_3$. We used the values of U = 8 eV and J = 0.88 eV that were obtained from the constrained LSDA supercell calculations [32,33]. Our LSDA+*U* calculations predict the band gap equal to 0.92 eV and the local magnetic moment for Mn atoms equal to 3.69 μ_B (Figure 3.2). The first attempts [31] to calculate the band gap and magnetic moment using LSDA+*U* approach implemented in the Stuttgart TBLMTO-47 code give a smaller value of 0.47 eV for the band gap and a slightly larger magnetic moment 3.99 μ_B. To the best of our knowledge, there are no available experimental values of the band gap and magnetic moment.

3.3 Conclusions

In this chapter, we discussed the structural properties of the hexagonal $YMnO_3$ calculated from first principles.

First, we reported the lattice parameters and atomic positions for the $P6_3cm$ ferroelectric phase of $YMnO_3$ computed within LSDA+*U* and B1-WC hybrid functional. Both approximations predict similar results that are in good agreement with experimental data, except for the atomic position of Mn atom that might probably be better predicted by including the noncollinear spin ordering treatment. Our estimated band gap and local magnetic moment of Mn atoms are well consistent with experimental measurements. Here, LSDA+*U* gives slightly closer values to experiment than B1-WC functional.

Then, we discussed the structure of the high-temperature $P6_3/mmc$ paraelectric phase of $YMnO_3$ computed within LSDA+*U*. The lattice parameters and atomic positions are again in good agreement with the experimental values.

Chapter 4

Dynamical properties of $YMnO_3$

4.1 Introduction

In this chapter, we discuss the dynamical properties of the ground state ferroelectric *P6₃cm* and high-temperature paraelectric *P6₃/mmc* structures of hexagonal $YMnO_3$.

Iliev *et al.* [54] first reported a qualitative Raman scattering study of single crystals and mostly agree with each others and 32 of 38 Raman and infrared-active phonon modes at room temperature expected at Γ-point have been identified. The list remains however incomplete and the proper assignment of recorded phonon modes is complicated by the fact that the interpretation of experimental data can only rely on semi-empirical calculations.

First, this chapter reports the first-principles calculations of transverse optical (TO) and longitudinal (LO) phonon frequencies at Γ-point of $YMnO_3$ in its *P6₃cm* ferroelectric phase. We compare the results obtained using the standard LSDA+*U* method and the B1-WC hybrid functional. A partial reassignment of previously published experimental data is proposed on the basis of these calculations. Our recorded polarized Raman-scattering spectra of $YMnO_3$ single crystal at Γ-point at room temperature support this reassignment. This new experimental study also confirms most previously reported data and brings to light one mode

never previously recorded. In addition, we report the Born effective charges and the angular dispersion curves of oblique phonon modes in order to take into account the misorientation of *c*-axis of our $YMnO_3$ single crystal and thus to insure the reliability of our assignment.

Next, we discuss the phonon frequencies at Γ-point calculated from first principles within LSDA+*U* of high-temperature paraelectric phase *P6₃/mmc* of $YMnO_3$. We compare the results with the published values in the literature measured experimentally and obtained using the semi-empirical model. The phonon frequencies at Γ-point of a triple cell are reported. These phonon calculations combine the frequencies of modes at Γ-point and at the zone-boundary K-point of the primitive unit cell.

4.2 Ferroelectric phase *P6₃cm*

4.2.1 Introduction

There are 90 zone-center phonon modes in the *P6₃cm* hexagonal ferroelectric phase of $YMnO_3$ that can be classified into: $10A_1 \oplus 5A_2 \oplus 10B_1 \oplus 5B_2 \oplus 15E_1 \oplus 15E_2$ [55]. The A_1 and E_1 modes are both Raman- and infrared-active whereas E_2 symmetry modes are only Raman-active (Table 4.1). The A_2, B_1 and B_2 are silent modes. The acoustic modes A_1 and E_1 are set to zero by applying the acoustic sum rule. The A_1, A_2, B_1 and B_2 modes are nondegenerated. The E_1 and E_2 modes are doubly degenerated.

$\Gamma_{Raman} = 9A_1 \oplus 14E_1 \oplus 15E_2$
$\Gamma_{infrared} = 9A_1 \oplus 14E_1$
$\Gamma_{silent} = 5A_2 \oplus 10B_1 \oplus 5B_2$
$\Gamma_{acoustic} = A_1 \oplus E_1$

Table 4.1 Classification of the zone-center phonon modes of *P6₃cm* into Raman-, infrared-active, silent and acoustic modes.

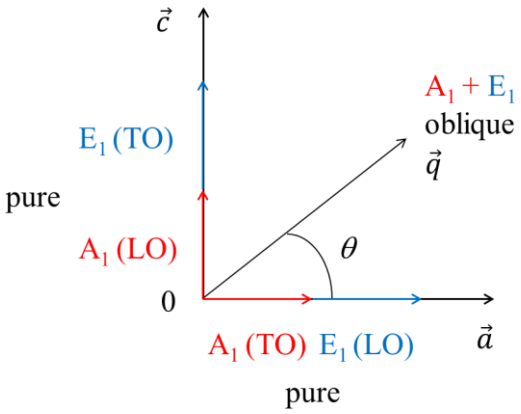

Figure 4.1 Orientation of $\vec{q}$ vector for LO and TO modes around Γ-point.

$YMnO_3$ is an ionic crystal (i.e. with non-vanishing Born effective charges). In such crystals, the long range Coulomb interaction causes a well-known phenomenon of LO-TO splitting, that is, the hardening of longitudinal optical (LO) modes with respect to transverse optical (TO) modes around the Brillouin zone center, Γ. Moreover, this hardening and so the frequency of the optical modes depends on the direction in approaching Γ.

At Γ-point, there are 23 polar phonon modes in ferroelectric $YMnO_3$: 9 of A_1 and 14 of E_1 symmetry. The A_1(TO) and E_1(LO) modes have their wave vector $\vec{q}$ oriented along *a*-axis (Figure 4.1). The A_1(LO) and E_1(TO) modes have their wave vector $\vec{q}$ oriented along c-axis. By varying the direction θ of $\vec{q}$ from 0 to 90 ° with respect to the crystallographic *a*-axis, one can determine the angular dependence of so-called oblique phonon frequencies, as a function of the phonon wave vector orientation, hereafter called angular dispersion.

4.2.2 Theoretical results

4.2.2.1 Phonons

Table 4.2 reports the $YMnO_3$ phonon frequencies with A_1, E_1 and E_2 symmetries, calculated within LSDA+*U* and B1-WC hybrid functional, in comparison to empirical values. Note that the TO and LO phonon frequencies of A_1 and E_1 modes are listed in ascending order.

Mode	LSDA+*U*	B1-WC	SM [54]	Mode	LSDA+*U*	B1-WC	SM [54]
$A_1(TO_1)$	170	172	147	$A_1(LO_1)$	172	173	147
$A_1(TO_2)$	252	247	204	$A_1(LO_2)$	264	257	216
$A_1(TO_3)$	272	277	222	$A_1(LO_3)$	278	288	269
$A_1(TO_4)$	313	320	299	$A_1(LO_4)$	333	338	301
$A_1(TO_5)$	428	435	388	$A_1(LO_5)$	428	435	398
$A_1(TO_6)$	460	472	423	$A_1(LO_6)$	460	472	467
$A_1(TO_7)$	498	501	492	$A_1(LO_7)$	517	526	496
$A_1(TO_8)$	593	583	588	$A_1(LO_8)$	691	707	601
$A_1(TO_9)$	691	707	662	$A_1(LO_9)$	728	746	662
$E_1(TO_1)$	171	116	117	$E_1(LO_1)$	171	160	118
$E_1(TO_2)$	183	166	147	$E_1(LO_2)$	183	167	149
$E_1(TO_3)$	211	191	158	$E_1(LO_3)$	214	211	158
$E_1(TO_4)$	245	227	212	$E_1(LO_4)$	245	244	231
$E_1(TO_5)$	274	244	233	$E_1(LO_5)$	289	286	245
$E_1(TO_6)$	302	298	250	$E_1(LO_6)$	338	321	337
$E_1(TO_7)$	367	362	353	$E_1(LO_7)$	378	363	367
$E_1(TO_8)$	379	378	390	$E_1(LO_8)$	400	413	403
$E_1(TO_9)$	403	415	410	$E_1(LO_9)$	414	418	415
$E_1(TO_{10})$	419	426	459	$E_1(LO_{10})$	459	444	477
$E_1(TO_{11})$	459	445	492	$E_1(LO_{11})$	488	493	527
$E_1(TO_{12})$	489	494	559	$E_1(LO_{12})$	560	562	559
$E_1(TO_{13})$	622	619	586	$E_1(LO_{13})$	626	626	589
$E_1(TO_{14})$	644	652	635	$E_1(LO_{14})$	644	652	635
$E_2(1)$	102	100	71				
$E_2(2)$	145	115	108				
$E_2(3)$	184	166	136				
$E_2(4)$	210	171	161				
$E_2(5)$	243	210	212				
$E_2(6)$	261	245	241				
$E_2(7)$	314	306	245				
$E_2(8)$	350	360	336				
$E_2(9)$	376	364	382				
$E_2(10)$	398	409	407				
$E_2(11)$	440	438	458				
$E_2(12)$	455	450	515				
$E_2(13)$	490	494	557				
$E_2(14)$	623	620	580				
$E_2(15)$	643	651	638				

Table 4.2 Zone-center Raman-active phonon frequencies (cm^{-1}) of *P6₃cm* ferroelectric $YMnO_3$ calculated from first principles in comparison to shell model (SM) calculations.

Mode	LSDA+*U*	B1-WC
A_2	105	99
A_2	266	263
A_2	306	314
A_2	401	408
A_2	524	533
B_1	137	139
B_1	262	261
B_1	271	272
B_1	424	434
B_1	520	526
B_2	127	122
B_2	207	209
B_2	224	225
B_2	274	274
B_2	342	351
B_2	401	407
B_2	454	461
B_2	529	540
B_2	700	719
B_2	769	788

Table 4.3 Calculated frequencies (cm^{-1}) of silent modes at Γ-point of the *$P6_3cm$* ferroelectric phase of $YMnO_3$.

Table 4.3 summarizes the calculated frequencies of silent A_2, B_1 and B_2 modes. To the best our knowledge, there are no previous density functional calculations in the literature.

Both our approaches predict similar results that are consistent within 4 %. We notice that the LSDA+*U* unit-cell volume is about 2 % smaller than the one of B1-WC (see the lattice parameters in Chapter 3). Since the phonon frequencies can be very sensitive to the unit-cell volume, a certain disagreement was expected. The highest deviation is observed for low frequency modes, up to about 300 cm^{-1}.

Comparing the phonon frequencies determined from first-principles and empirically, the empirical frequencies are reasonably well predicted, although, as it will be discussed in the

following, the inaccuracies appear in assigning the modes. Our first-principles results provide a more reliable estimate of the frequencies.

4.2.2.2 Born effective charges and optical dielectric constant

Table 4.4 reports the Born effective charges for all atoms calculated from first-principles in the ferroelectric *P6$_3$cm* phase of $YMnO_3$.

As we can see in Table 4.4, the absolute value of the Z^*_{zz} components of Born effective charges for most atoms along *c*-axis are larger than the ones in *ab* plane.

Our calculated dynamical effective charges (see in Table 4.4) are moderately larger than the nominal charges Y^{3+}, Mn^{3+} and O^{2-}. Thus, there are anomalous charges, but they are smaller than the ones of ferroelectric perovskites [56]. Aken et *al.* [15] determined the Z^*s even closer to nominal values $Z^*_Y = +3.6$, $Z^*_{Mn} = +3.3$, $Z^*_{O_{pl}} = -2.2$ and $Z^*_{O_{ap}} = -2.3$. The experimental measurements [57] give values slightly larger than our calculations $Z^*_Y = +4.0$, $Z^*_{Mn} = +4.0$, $Z^*_{O_{pl}} = -2.7$ and $Z^*_{O_{ap}} = -2.7$. This explains in part a small polarization of the hexagonal ferroelectric phase of $YMnO_3$. In section 5.4 Chapter 5, we discuss the polarization in more details.

For the computation of the LO-TO splitting, we used the optical dielectric constant $\varepsilon_\infty = 6.46$ along *c* direction taken from Ref. [57].

4.2.3 Experimental results

4.2.3.1 Introduction

In addition to calculations, we used Raman spectroscopy technique to record Raman spectra. There are 38 Raman-active phonon modes in hexagonal ferroelectric $YMnO_3$. The Table 4.5 reviews all possible scattering configurations and observable modes.

Y1,2	3.71	0.00	0.00	Y3,4	3.78	-0.10	0.00	Y5,6	3.78	0.10	0.00
	0.00	3.71	0.00		0.10	3.78	0.00		-0.10	3.78	0.00
	0.00	0.00	3.97		0.00	0.00	3.90		0.00	0.00	3.90
Mn1	3.34	0.00	0.09	Mn2	3.41	0.04	-0.05	Mn3	3.41	-0.04	-0.05
	0.00	3.34	0.00		0.04	3.36	0.08		-0.04	3.36	-0.08
	0.41	0.00	3.95		-0.21	0.36	3.95		-0.21	-0.36	3.95
Mn4	3.34	0.00	-0.09	Mn5	3.41	-0.04	0.05	Mn6	3.41	0.04	0.05
	0.00	3.43	0.00		-0.04	3.36	0.08		0.04	3.36	-0.08
	-0.41	0.00	3.95		0.21	0.36	3.95		0.21	-0.36	3.95
O1	-2.01	0.00	0.17	O2	-2.01	0.00	-0.17	O3	-2.06	-0.03	-0.09
	0.00	-2.08	0.00		0.00	-2.08	0.00		-0.03	-2.03	0.15
	0.21	0.00	-3.07		-0.21	0.00	-3.07		-0.10	0.18	-3.07
O4	-2.06	0.03	-0.09	O5	-2.06	0.03	0.09	O6	-2.06	-0.03	0.09
	0.03	-2.03	-0.15		0.03	-2.03	0.15		-0.03	-2.03	-0.15
	-0.10	-0.18	-3.07		0.10	0.18	-3.07		0.10	-0.18	-3.07
O7	-1.98	0.00	0.16	O8	-1.98	0.00	-0.16	O9	-1.95	0.01	-0.08
	0.00	-1.94	0.00		0.00	-1.94	0.00		0.02	-1.97	0.14
	0.17	0.00	-3.21		-0.17	0.00	-3.21		-0.08	0.14	-3.21
O10	-1.96	-0.01	-0.08	O11	-1.96	-0.01	0.08	O12	-1.95	0.01	0.08
	-0.01	-1.97	-0.14		-0.01	-1.96	0.14		0.02	-1.97	-0.14
	-0.08	-0.14	-3.21		0.08	0.14	-3.21		0.08	-0.14	-3.21
O13,14	-3.11	0.00	0.00	O15,16	-3.15	0.02	0.00	O17,18	-3.15	-0.02	0.00
	0.00	-3.11	0.00		-0.02	-3.15	0.00		0.02	-3.15	0.00
	0.00	0.00	-1.66		0.00	0.00	-1.56		0.00	0.00	-1.56

Table 4.4 Born effective charges of the ferroelectric $YMnO_3$ calculated within LSDA+*U*. Space group: $P6_3cm$. Tensors are reported in cartesian coordinates in atomic units[1]. The dynamical charges are $Z^*_Y = +3.8$, $Z^*_{Mn} = +3.6$, $Z^*_{O_{pl}=O_{1\text{-}12}} = -2.4$ and $Z^*_{O_{ap}=O_{13\text{-}18}} = -2.6$ defined as $Z^*_i = (Z^*_{xx} + Z^*_{yy} + Z^*_{zz})/3$, with *i* - atom.

[1] The atomic unit of charge is the electron charge.

Configurations	Observed modes
$x(zz)\bar{x}$	$A_1(TO)$
$x(yy)\bar{x}$	$A_1(TO) + E_2$
$x(zy)\bar{x}$	$E_1(TO)$
$x(yz)\bar{x}$	
$y(xx)\bar{y}$	$A_1(TO) + E_2$
$y(zz)\bar{y}$	$A_1(TO)$
$y(xz)\bar{y}$	$E_1(TO)$
$y(zx)\bar{y}$	
$z(xx)\bar{z}$	$A_1(LO) + E_2$
$z(yy)\bar{z}$	$A_1(LO) + E_2$
$z(xy)\bar{z}$	E_2
$z(yx)\bar{z}$	

Table 4.5 Porto notation and Raman-active phonon modes of ferroelectric $YMnO_3$. Space group: $P6_3cm$. $E_1(LO)$ is not active.

Exciting along in-plane *a*- or *b*-axis, the pure $A_1(TO)$ symmetry mode is recorded when polarization is oriented along the ferroelectric *c*-axis (configurations $x(zz)\bar{x}$ and $y(zz)\bar{y}$), both $A_1(TO)$ and E_2 are observed when the polarization is oriented along one of the in-plane axis (configurations $x(yy)\bar{x}$ and $y(xx)\bar{y}$) and pure $E_1(TO)$ mode is observed when the polarization is crossed (configurations $x(z\,y,y\,z)\bar{x}$ and $y(x\,z,z\,x)\bar{y}$). Exciting along ferroelectric *c*-axis, the $A_1(LO)$ and E_2 symmetries are observed when the polarization is aligned along one of in-plane axis (configurations $z(xx)\bar{z}$ and $z(yy)\bar{z}$) and pure E_2 symmetry is observed when the polarization is crossed (configurations $z(x\,y,y\,x)\bar{z}$). The $E_1(LO)$ symmetry modes are not visible. We measured all configurations in order to identify and assign symmetries precisely.

4.2.3.2 Miscut of single crystal

Raman measurements have been performed on a $YMnO_3$ single crystal grown by the standard floating zone technique using a four mirror furnace (provided by the group of T. T. M. Palstra

in Groningen, for more details concerning the growth can be found in Ref. [43]). The lattice parameters determined from the x-ray-diffraction data are the following : a = 6.12 Å and c = 11.52 Å. The crystal surfaces were polished in order to reduce the surface roughness and thus the light reflection.

Note that unfortunately our $YMnO_3$ single crystal is miscut. The c-axis is not exactly perpendicular to the surface, but tilted by ~ 20° as shown in Figure 4.2. Therefore, we didn't measure pure A_1(TO) and pure E_1(TO) symmetry modes, but oblique mode frequencies. For E_2 modes, the frequencies remain unchanged since the E_2 are not polar modes.

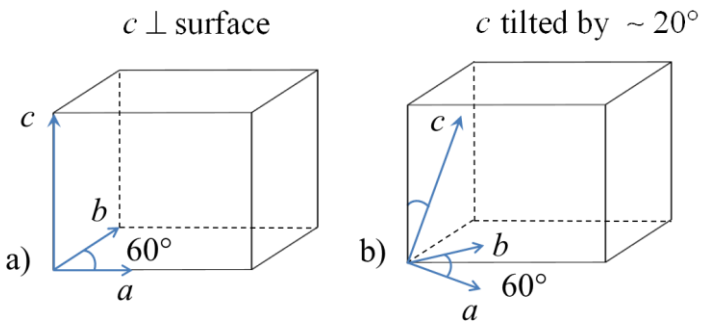

Figure 4.2 $YMnO_3$ single crystal with *c*-axis (a) perpendicular to the surface, (b) tilted by ~20° to the surface (miscut).

In order to quantify the effect of the crystal miscut on phonon frequencies, we computed the angular dependence of the frequencies that show the evolution from pure TO to pure LO phonon modes (Figure 4.3). The red circles at the angle of 0° and 90° mark the TO and LO modes of A_1 symmetry, respectively. Since A_1(TO) is perpendicular to E_1(TO), the pure TO and LO phonon modes of E_1 symmetry are marked at 90 and 0° by blue stars, respectively.

As mentioned previously, the modes between the pure TO and LO modes are the oblique modes that mix LO and TO frequencies. The main difficulty is that there is no a one to one correspondence between TO and LO modes. To get Figure 4.3, we had to explicitly diagonalize the dynamical matrix $D(\mathbf{q} \to 0)$ including the appropriate nonanalytical

electrostatic contribution $D^{\text{nan}}(\mathrm{q}\to 0)$ (computed from Z^* and ε^{∞}) and approaching $q=0$ along each θ (between 0° and 90° with a step of 1°) orientation [58]:

$$D_{\kappa\alpha,\kappa'\beta}(\mathbf{q}\to 0)=D^{\text{an}}_{\kappa\alpha,\kappa'\beta}(\mathbf{q}=0)+D^{\text{nan}}_{\kappa\alpha,\kappa'\beta}(\mathbf{q}\to 0), \tag{4.1}$$

where the nonanalytical term can be written as:

$$D^{\text{nan}}_{\kappa\alpha,\kappa'\beta}(\mathbf{q}\to 0)=\frac{4\pi}{\Omega_0}\frac{\sum_{\beta'}(Z^*_{\kappa,\beta'\alpha}q_{\beta'})(Z^*_{\kappa,\alpha'\beta}q_{\alpha'})}{\sum_{\alpha'\beta'}q_{\alpha'}\varepsilon^{\infty}_{\alpha'\beta'}q_{\beta'}}. \tag{4.2}$$

In Figure 4.3, the red circles at 20° show the oblique modes with the dominant A_1 symmetry. The blue stars at 70° (miscut angle of 20° respect to pure E_1(TO) modes) show the oblique modes with the dominant E_1 symmetry.

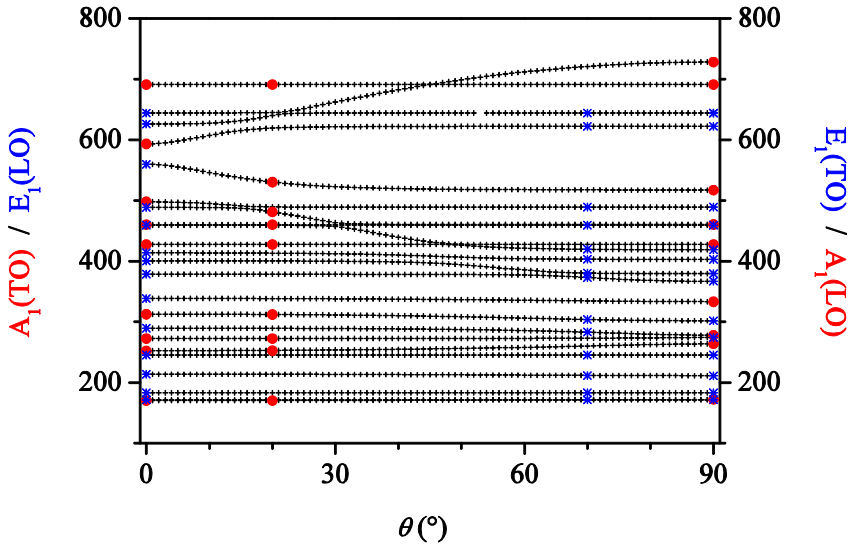

Figure 4.3 Angular dependence of phonon A_1 and E_1 modes of ferroelectric $YMnO_3$. Space group: *P6₃cm*. Phonon frequencies (cm^{-1}) of A_1 and E_1 symmetry modes are marked at specific angles by red dots and blue stars, respectively.

In order to determine the dominant A_1 or E_1 character of modes at the crystal miscut angle, we computed the overlap α_{ij} of eigenvectors γ_i^{TO} of TO phonon modes with eigenvectors γ_j of

oblique modes at the crystal misorientation angle ($\alpha_{ij} = < \gamma_i^{TO} \mid \gamma_j >$). Then, we deduced the total overlap $\alpha_j^{A_1\ 2} = \sum_{i \in A_1} \alpha_{ij}^2$ of oblique modes at 20° with A_1(TO) modes and, respectively, the total overlap $\alpha_j^{E_1\ 2} = \sum_{i \in E_1} \alpha_{ij}^2$ of oblique modes at 70° with E_1(TO) modes. When $\alpha_j^{A_1} > \alpha_j^{E_1}$, the dominant A_1 character was attributed to oblique mode and vice versa.

We observe that the angular dependence is very weak meaning that the oblique frequencies measured on the miscut crystal are good estimate of pure TO and LO frequencies. The angular dependence of the frequencies of $A_1(TO_7)$ and $A_1(TO_8)$ symmetry modes at 498 cm^{-1} and 593 cm^{-1} is more significant, but we don't observe these modes in our Raman spectra. Note that the dominant A_1 or E_1 character for these two modes is not well defined (see Appendix A). In the following, we limit our discussion to the TO frequency modes.

4.2.3.3 Experimental Raman spectra

Figure 4.4 shows the plot of selected configurations that were recorded at room temperature. The following configurations $y\,(z\ x)\,\bar{y}$, $y\,(z\ z)\,\bar{y}$ and $z\,(x\ y)\,\bar{z}$ were chosen because they allow to observe independently E_1(TO), A_1(TO) and E_2 modes. The configuration $y\,(x\ x)\,\bar{y}$ was added for the purpose of showing the sum of A_1(TO) and E_2 modes and thus illustrating the method of identification. The modes that are forbidden in a noted configuration, but are nevertheless observed because of i) polarization leakage, ii) disorientation of crystal are marked by stars. It usually happens for intense peaks: for instance, the most intense A_1 mode appears in all spectra. The lines in Figure 4.4 represent the LSDA+*U* data. As can be seen, the calculated positions match well the measured peaks. The comparison is plotted between spectra taken at room temperature and values computed at 0 K thus the majority of calculated frequencies are positioned at higher frequencies than those measured. At low temperature, the experimental peaks shift by few reciprocal centimeters to higher frequencies, slightly improving the matching between calculated and experimental data. These spectra globally match previously published spectra and also supplement them with the identification of one additional mode at a frequency of 247 cm^{-1}, as it will be discussed later.

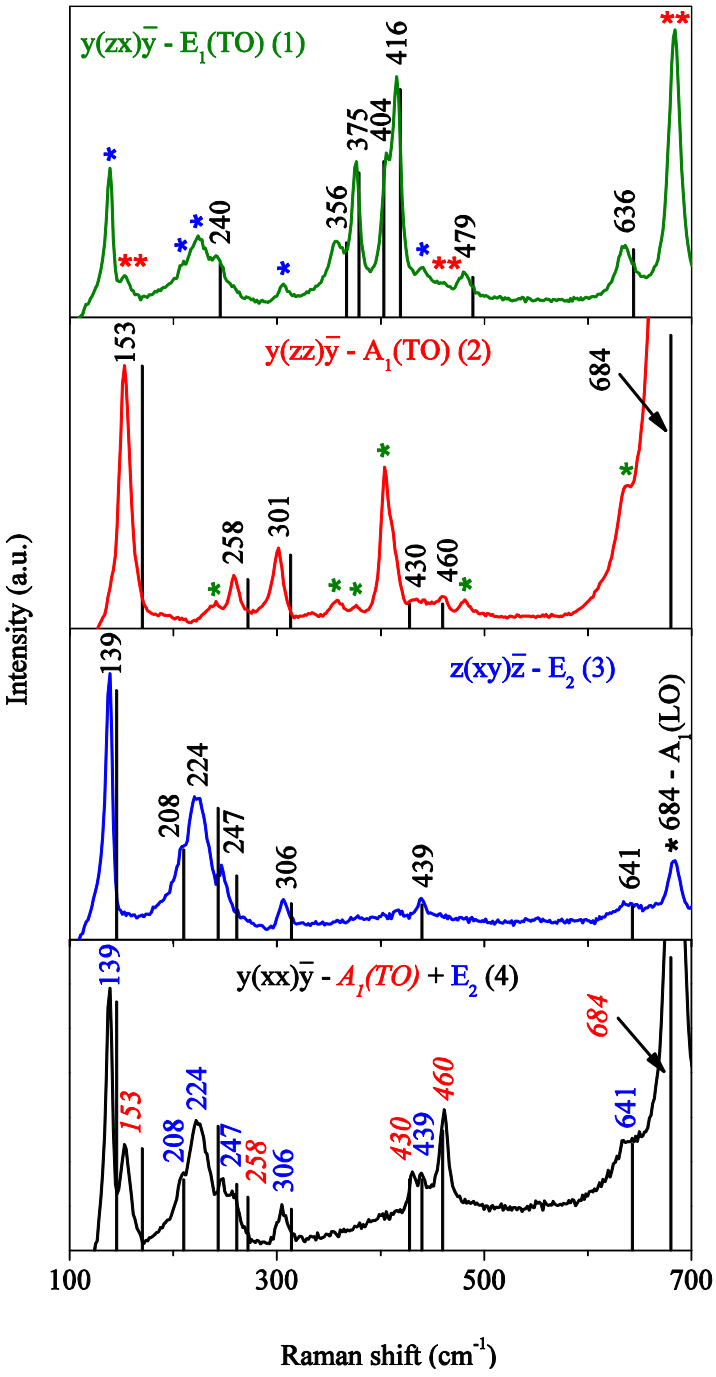

Figure 4.4 Raman spectra of $YMnO_3$ (*P6₃cm*) single crystal at room temperature. Each configuration represents the allowed symmetries: E_1(TO), A_1(TO), E_2, A_1(TO) + E_2. The appearing forbidden symmetries are marked by stars: E_2*, A_1(TO)** in spectrum (1); E_1(TO)* - (2), A_1(LO)* - (3). The positions of A_1(TO) and E_2 modes in spectrum (4) are noted in red color (italic) and blue color, respectively. The drawn lines represent the computed frequencies within LSDA+*U*.

	LSDA+*U*		Experiment					
Mode	0°	20°	RT	RT [54]	RT [59]	10K [59]	15K [60]	10K [57]
$A_1(TO_1)$	170	170	153	148	151	161	160	(154)
$A_1(TO_2)$	252	253		190	241	244	210	
$A_1(TO_3)$	272	272	258	257(265)	259	264	264	(235)
$A_1(TO_4)$	313	312	301	297	300	307		(260)
$A_1(TO_5)$	428	428	430	(398)	431	434		(304)
$A_1(TO_6)$	460	460	460	433(428)	461	467	435	(432)
$A_1(TO_7)$	498	481		459			466	(486)
$A_1(TO_8)$	593	530		(612)				(562)
$A_1(TO_9)$	691	691	684	681	683	686	686	
$E_1(TO_1)$	171	171						
$E_1(TO_2)$	183	183						(162)
$E_1(TO_3)$	211	212						
$E_1(TO_4)$	245	245	240	(211)				(207)
$E_1(TO_5)$	274	283		(238)			247	(249)
$E_1(TO_6)$	302	304		(281)				(299)
$E_1(TO_7)$	367	373	356	(308)	354	361	360	(380)
$E_1(TO_8)$	379	380	375	376			377	(400)
$E_1(TO_9)$	403	403	404	408			420	(416)
$E_1(TO_{10})$	419	420	416	(457)				
$E_1(TO_{11})$	459	459		(491)			509	
$E_1(TO_{12})$	489	489	479					
$E_1(TO_{13})$	622	622		(596)				(594)
$E_1(TO_{14})$	644	644	636	632	631	637	638	
$E_2(1)$	102							
$E_2(2)$	145		139					
$E_2(3)$	184			135			141	
$E_2(4)$	210		208					
$E_2(5)$	243		224	~ 215	223	231	225	
$E_2(6)$	261		247					
$E_2(7)$	314		306				307	
$E_2(8)$	350			302	356	357	331	
$E_2(9)$	376						406	
$E_2(10)$	398						444	
$E_2(11)$	440		439		439	441	483	
$E_2(12)$	455							
$E_2(13)$	490							
$E_2(14)$	623							
$E_2(15)$	643		641				647	

Table 4.6 Zone-center Raman-active TO phonon frequencies (cm^{-1}) at 0° and miscut angle of 20° of $P6_3cm$ ferroelectric $YMnO_3$ calculated from first-principles in comparison to Raman, infrared (in brackets) data obtained at room and low temperature.

4.2.4 Discussion

Table 4.6 reports the $YMnO_3$ TO phonon frequencies with A_1, E_1 and E_2 symmetries, calculated within LSDA+*U* in comparison to experimental values. As can be seen, the calculated frequencies correspond well to the experimental values. However, disagreements appear in assigning the modes. The attempts of Iliev et *al.* to support the assignment of experimentally observed Raman and infrared peaks using a shell model are reasonably good, but not always very accurate. In the following, we discuss the modes of each symmetry independently and propose a reassignment of certain modes. Note that in Table 4.6 our own experimental data are listed according to the assignment deduced from comparison with our first-principles calculations while the experimental data are listed as in their original work, according to the assignment they made on the basis of their semi-empirical calculations.

There are 9 Raman and infrared-active A_1 symmetry modes. The literature provides all their frequencies. However, our first-principles data question the assignment of the room temperature (RT) experimental frequencies at 398 cm^{-1} (IR) , 433 cm^{-1} (428 cm^{-1}, 432 cm^{-1}, IR and 435 cm^{-1}, 15 K) and 459 cm^{-1} (466 cm^{-1}, 15 K). A better correspondence with first-principles calculations and measured values is achieved when the modes recorded using Raman technique at 433 cm^{-1} (432 cm^{-1}, IR and 435 cm^{-1}, 15 K) and 459 cm^{-1} (466 cm^{-1}, 15 K) and initially assigned to $A_1(TO_6)$ and $A_1(TO_7)$, are attributed to $A_1(TO_5)$ and $A_1(TO_6)$. It is tempting also to assign the IR mode at 428 cm^{-1} to $A_1(TO_5)$ but, then, the presence of another IR mode at 398 cm^{-1} is questionable. Supplementary measurements are certainly needed to further clarify the assignment of these modes.

In the literature, 11 frequencies out of 14 existing E_1 symmetry modes have been experimentally reported. As discussed below, the reassignment in view of first-principles calculations increases the number of recorded modes to 13. The RT frequencies at 211 cm^{-1} (207 cm^{-1}, IR), 238 cm^{-1} (247 cm^{-1}, 15 K and 249 cm^{-1}, IR), 281 cm^{-1} and 308 cm^{-1} initially assigned to the modes from $E_1(TO_4)$ to $E_1(TO_7)$, respectively, clearly match better with our calculated and measured values from $E_1(TO_3)$ to $E_1(TO_6)$; this further removes the apparent disagreement between the frequencies initially proposed at RT and 15 K for $E_1(TO_7)$. In addition, we suggest that the modes observed at 10 K in the infrared measurements at

380 cm^{-1} and 400 cm^{-1} better match with $E_1(TO_8)$ and $E_1(TO_9)$ than $E_1(TO_7)$ and $E_1(TO_8)$. The frequency measured at 15 K at 420 cm^{-1} (416 cm^{-1}, IR) should be assigned to $E_1(TO_{10})$ rather than to $E_1(TO_9)$. Then, we finally propose to assign the observed modes at 457 cm^{-1} and 491 cm^{-1} (509 cm^{-1}, 15 K) to $E_1(TO_{11})$ and $E_1(TO_{12})$, respectively, rather than to $E_1(TO_{10})$ and $E_1(TO_{11})$ as initially proposed by Iliev *et al* and Fukumura *et al*.

The list of registered E_2 symmetry modes is more sparse. The reassignment with respect to our first-principle data extents this list from 8 to 10 known frequencies, out of the 15 existing ones. The experimentally registered modes at RT at 135 cm^{-1} (141 cm^{-1}, 15 K), ~ 215 cm^{-1} and at 15 K at 406 cm^{-1}, 444 cm^{-1} and 483 cm^{-1} fit well the $E_2(2)$, $E_2(4)$, $E_2(10)$, $E_2(11)$ and $E_2(13)$ calculated and measured frequencies, respectively. The experimental mode measured at RT by Iliev *et al.* at 302 cm^{-1} and assigned to $E_2(8)$ and measured at 15 K by Fukumura *et al* at 307 cm^{-1} and assigned to $E_2(7)$ corresponds to our calculated and measured $E_2(7)$ mode, thus rather confirming the assignment of Fukumura *et al*. Our measured mode at a frequency of 247 cm^{-1} and assigned to $E_2(6)$ is a newly observed mode.

4.3 Paraelectric phase *P6₃/mmc*

There are 30 zone-center phonon modes in the hexagonal *P6₃/mmc* paraelectric phase of $YMnO_3$ that can be classified into: $\Gamma = A_{1g} \oplus E_{1g} \oplus 3E_{2g} \oplus 4A_{2u} \oplus 4E_{1u} \oplus 3B_{2g} \oplus 2B_{1u} \oplus 2E_{2u}$ [55]. The A_{1g}, E_{1g} and E_{2g} are Raman-active, A_{2u} and E_{1u} are infrared-active and B_{2g}, B_{1u} and E_{2u} are silent modes (Table 4.7). The acoustic modes A_{2u} and E_{1u} are set to zero by applying the acoustic sum rule. The E modes are doubly degenerated. The paraelectric structure of $YMnO_3$ is centrosymmetric thus the Raman- and infrared-active modes are separated.

Table 4.8 summarizes the zone-center phonon frequencies of $YMnO_3$ calculated from first principles within LSDA+*U* in comparison to empirical and experimental values. Note that the experimental data of Fukumura *et al.* [60] are listed as in their original work, according to the

assignment based on the semi-empirical calculations. To the best our knowledge, there are no previous density functional calculations in the literature.

$\Gamma_{Raman} = A_{1g} \oplus E_{1g} \oplus 3E_{2g}$
$\Gamma_{infrared} = 3A_{2u} \oplus 3E_{1u}$
$\Gamma_{silent} = 3B_{2g} \oplus 2B_{1u} \oplus 2E_{2u}$
$\Gamma_{acoustic} = A_{2u} \oplus E_{1u}$

Table 4.7 Classification of the zone-center phonon modes of *P6₃/mmc* into Raman-, infrared-active, silent and acoustic modes.

The phonon frequencies determined using a shell model match reasonably well the first-principles data, but are less accurate. The frequencies of $E_{2g}(2)$, $E_{1u}(3)$ and $E_{2u}(2)$ modes are highly overestimated and underestimated, respectively.

The calculated frequencies are in good agreement with the experimental values. Experimentally, 4 of 5 frequencies of phonon modes are observed. The mode measured at a frequency of $\sim 395\ cm^{-1}$ is assigned to $E_{2g}(2)$ mode with respect to semi-empirical calculations. Our first-principles calculations show a closer match with the $E_{2g}(3)$ mode.

The zone-center phonon frequencies of *P6₃/mmc* paraelectric phase of $YMnO_3$ do not show any structural instability although the ground structure of $YMnO_3$ is the ferroelectric *P6₃cm* phase. This confirms that $YMnO_3$ is not a proper ferroelectric. Instead, the condensation of the polar distortion is driven by an unstable mode at K $(\frac{1}{3}\ \frac{1}{3}\ 0)$. In order to access to the frequencies at K-point, we computed the zone-center phonons of the *P6₃/mmc* in the triple paraelectric unit cell.

The zone-center calculations of the *P6₃/mmc* triple paraelectric phase give the frequencies at the zone-center Γ-point (0 0 0) and zone-boundary K-point $(\frac{1}{3}\ \frac{1}{3}\ 0)$. There are 30 phonon modes at Γ-point (classified as in Table 4.7) and 30 phonon modes at K-point that can be

classified into : $\Gamma_K = 2K_1 \oplus 2K_2 \oplus 3K_3 \oplus 3K_4 \oplus 6K_5 \oplus 4K_6$ [55]. The K_5 and K_6 modes are doubly degenerated.

Mode	LSDA+*U*	SM [54]	1100K [60]
A_{1g}	713	666	664
E_{1g}	440	402	~420
$E_{2g}(1)$	143	107	~120 (?)
$E_{2g}(2)$	249	395	~395
$E_{2g}(3)$	456	498	
$A_{2u}(1)$	88	170	
$A_{2u}(2)$	411	389	
$A_{2u}(3)$	593	594	
$E_{1u}(1)$	165	121	
$E_{1u}(2)$	255	239	
$E_{1u}(3)$	392	496	
$B_{2g}(1)$	166		
$B_{2g}(2)$	394		
$B_{2g}(3)$	791		
$E_{2u}(1)$	108	83	
$E_{2u}(2)$	367	244	
$B_{1u}(1)$	193		
$B_{1u}(2)$	701		

Table 4.8 Zone-center phonon frequencies (cm^{-1}) of *P6$_3$/mmc* paraelectric $YMnO_3$ calculated from first principles in comparison to shell model (SM) calculations and experimental values obtained at 1100 K.

The Table 4.9 shows the zone-center phonon frequencies of the *P6$_3$/mmc* triple paraelectric phase of $YMnO_3$ calculated from first principles. The frequencies of the triple cell at Γ-point (0 0 0) differ by only a few reciprocal centimeters from the frequencies calculated for the simple cell (see Table 4.8); this is a consequence of the different *k*-point sampling in both calculations and bring to light the level of convergence of our calculations. The calculations reveal two instabilities at K-point: K_3 mode at a frequency of $153i$ cm^{-1} and K_4 mode at a

frequency of $14i$ cm^{-1}. The unstable K_3 mode is the primary mode condensing at the ferroelectric phase transition. Our frequency of K_3 mode is identical to that calculated by Fennie and Rabe [16].

Mode	$\Gamma(0,0,0)$	Mode	Γ_K $(\frac{1}{3},\frac{1}{3},0)$
A_{1g}	712	$K_1(1)$	266
E_{1g}	438	$K_1(2)$	533
$E_{2g}(1)$	145	$K_2(1)$	215
$E_{2g}(2)$	246	$K_2(2)$	529
$E_{2g}(3)$	454	$K_3(1)$	$153i$
$A_{2u}(1)$	85	$K_3(2)$	228
$A_{2u}(2)$	410	$K_3(3)$	407
$A_{2u}(3)$	593	$K_4(1)$	$14i$
$E_{1u}(1)$	167	$K_4(2)$	265
$E_{1u}(2)$	253	$K_4(3)$	402
$E_{1u}(3)$	391	$K_5(1)$	182
$B_{2g}(1)$	165	$K_5(2)$	249
$B_{2g}(2)$	393	$K_5(3)$	372
$B_{2g}(3)$	791	$K_5(4)$	447
$E_{2u}(1)$	106	$K_5(5)$	483
$E_{2u}(2)$	365	$K_5(6)$	656
$B_{1u}(1)$	192	$K_6(1)$	213
$B_{1u}(2)$	701	$K_6(2)$	296
		$K_6(3)$	417
		$K_6(4)$	647

Table 4.9 LSDA+*U* zone-center phonon frequencies (cm^{-1}) of the *P6$_3$/mmc* triple paraelectric $YMnO_3$.

4.4 Improper ferroelectric

As described in Chapter 1, $YMnO_3$ is indeed an improper ferroelectric. The ferroelectric phase transition from the *P6₃/mmc* paraelectric phase to the *P6₃cm* ferroelectric one essentially arises from the condensation of an unstable K_3 zone-boundary mode (153*i* cm^{-1}), driving the concomitant condensation of a stable Γ_2^- polar zone-center mode (90 cm^{-1}), which linearly couples with it [16]. Consistently with them, we observe in the paraelectric *P6₃/mmc* phase, an unstable K_3 mode at a frequency of 153*i* cm^{-1} and a stable, but low frequency Γ_2^- mode at a frequency of 85 cm^{-1}, that are together responsible for 99% of the structural distortion yielding the *P6₃cm* ferroelectric phase. Restricting ourselves to the two-dimensional subspace defined by these relevant phonon modes, and based on the energy landscape reported by Fennie and Rabe, we can estimate[2] that these modes will be stabilized by anharmonicities to higher frequencies in the ferroelectric phase, giving rise to phonon modes at 224 cm^{-1} for K_3 and 302 cm^{-1} for Γ_2^-.

In order to test this ''2-phonons'' model and identify to which phonons these frequencies are associated, we made the overlap between the phonon eigendisplacements of the *P6₃cm* phase and the relevant K_3 and Γ_2^- mode eigendisplacements of the *P6₃/mmc* phase condensing at the phase transition.[3] On the one hand, we observed that the K_3 mode of the paraelectric phase mainly overlaps with the $A_1(TO_1)$ mode at 170 cm^{-1} (0.73) and the $A_1(TO_6)$ mode at 460 cm^{-1} (0.46) of the ferroelectric phase. On the other hand, we obtained that the Γ_2^- mode of the paraelectric phase mainly overlaps with the $A_1(TO_2)$ mode at 252 cm^{-1} (0.62) and the $A_1(TO_4)$ mode at 313 cm^{-1} (0.65) of the ferroelectric phase. Therefore, there is no one-to-one correspondence between the phonons of the paraelectric phase condensing at the phase

---

[2] The frequencies were determined from the curvature of the model energy along K_3 and Γ_2^- directions of the global minimum associated to the ferroelectric ground state.

[3] The overlap α is defined as $\alpha = <\eta^{FE} | M | \eta^{PE}_{K_3,\Gamma_2^-}>$ and listed in the appendix B.

transition and the phonons of the ferroelectric phase, but the K_3 and Γ_2^- modes can be linked to the low frequency A_1 modes of the ferroelectric phase.

4.5 Conclusions

We reported the zone-center phonon frequencies of hexagonal $YMnO_3$.

First, we reported the TO and LO phonon frequencies at Γ-point calculated from first principles using LSDA+*U* and B1-WC functional of the *P6₃cm* ferroelectric phase of $YMnO_3$. The obtained values using both theoretical approaches agreed well with each other, except the low frequency modes, where the difference was more significant. Then, we reported our measured Raman spectra at room temperature of $YMnO_3$ single crystal. The angular dispersion curves of oblique phonon modes didn't show a strong LO-TO mode splitting thus the misorientation of *c*-axis of our crystal didn't influence the assignment of modes. The correspondence with our measured as well as the experimental values available in the literature was very good. However, disagreements appeared in assigning modes since the empirical prediction used to label the modes was clearly not sufficiently accurate. Thus, our proposed reassignment of certain modes with respect to the first-principles calculations and our measured frequencies increased the number of known modes from 28 to 32 out of 38 Raman-active phonon modes. One of these modes was our newly observed E_2 symmetry mode at a frequency of 247 cm^{-1}. Our calculated Born effective charges within LSDA+*U* were slightly larger than the nominal values and were in good agreement with the experimentally obtained values.

Next, we reported the first-principles phonon frequencies at Γ-point using LSDA+*U* of the *P6₃/mmc* paraelectric phase of $YMnO_3$. The correspondence with the values calculated using a semi-empirical approach was good, although the inaccuracies were present since this approach was less reliable than the first-principles calculations. The calculated values matched well the available experimental data. We proposed a reassignment of one mode with

respect to our calculated values. We reported the zone-center frequencies of the *P6$_3$/mmc* in-plane triple cell. Two instabilities at Γ_K-point were obtained.

Last, we discussed the ferroelectric phase transition from the high-temperature paraelectric to ground ferroelectric phase. We identified the low frequency A_1 symmetry modes of the ferroelectric phase that strongly overlap with the K_3 zone-boundary at a frequency of 153*i* cm^{-1} and Γ_2^- polar zone-center at 85 cm^{-1} modes of the paraelectric phase condensing at the phase transition.

Chapter 5

First-principles based model energy for epitaxial $YMnO_3$ thin films

During the recent years, the tuning of the ferroelectric properties in thin films has been a topic of intensive researches. In particular the role of the mechanical and electrical boundary conditions on the ferroelectric properties of epitaxial films has been widely discussed and now is well understood. These studies quasi exclusively focused on proper ferroelectric oxides of cubic perovskite structure. In contrast, very little is known about the role of epitaxial strain on hexagonal perovskites and the role of the electrical boundary conditions on improper ferroelectrics.

Fennie and Rabe developed a simple model based on first-principles calculations to describe the ferroelectric properties [16]. This model properly includes the relevant ionic degrees of freedom, but without treating explicitly the strain. In the present study we generalize such a model in order to be able to treat explicitly the role of the mechanical constraints such as epitaxial strain. Taking advantage of recent study developments, we also include a term describing correctly electrostatic boundary conditions from open-circuit to short-circuit including the case of imperfect screening.

5.1 Relevant ionic degrees of freedom

In order to identify the relevant ionic degrees of freedom, first, we determined the atomic distortion vector Δ that relates the ferroelectric *P6$_3$/cm* and paraelectric *P6$_3$/mmc* phases of $YMnO_3$. Table 5.1 shows the Δ computed within LSDA+*U*. In order to properly decouple the ionic and strain degrees of freedom, the distortion vector was determined in reduced coordinates. Nevertheless, since this vector will be compare to phonon eigendisplacements of the paraelectric phase expressed in cartesian coordinates, Δ was converted in cartesian coordinates using the lattice parameters of the triple paraelectric phase.

Atom	Δ (Å)	
	Δx	Δz
Y_1	0	0.2801
Y_2	0	-0.2078
Mn	0.0011	0.0013
O_{ap1}	-0.1673	-0.0290
O_{ap2}	0.1624	-0.0325
O_{pl3}	0	-0.2619
O_{pl4}	0	0.2271

Table 5.1 Atomic distortions Δ (Å) along [100] (in-plane axis) and [001] (polar axis) of paraelectric $YMnO_3$, respectively. Space group: *P6$_3$cm*, from centrosymmetric positions, Space group: *P6$_3$/mmc*.

Then, we normalized the distortion $\Delta = \mathrm{A} \cdot \Delta^{\mathrm{norm}}$ (the norm $\mathrm{A} = 6.32$) and we made an overlap α_i between the atomic distortion vector Δ^{norm} and phonon eigendisplacement vectors of paraelectric phase η_i of modes i defined as $\alpha_i = <\eta_i | M | \Delta^{\mathrm{norm}}>$ such that $\sum_i \alpha_i^2 = 1$, where M is the standard atomic weight. Table 5.2 lists the most significant contributions α_i to the atomic distortions. Note that we considered the contributions $\alpha_i > 0.01\%$.

	K_3			Γ_2^-			Γ_1^+	K_1	
ω (cm^{-1})	153*i*	228	407	85	410	593	712	266	533
α_i	-0.967	0.162	-0.062	0.175	-0.003	0.001	-0.067	-0.002	0.006

Table 5.2 Frequencies ω and contributions α_i of modes *i* to the atomic distortion vector from the ferroelectric *P6₃cm* to paraelectric *P6₃/mmc* phase of $YMnO_3$. Space group: *P6₃/mmc*.

As we can see in Table 5.2, only 9 amongst the 90 phonon modes contribute to the ferroelectric distortion: four modes - Γ_2^- (label $A_{2u}(1)$ in Chapter 4) at the frequencies of 85 cm^{-1}, 410 cm^{-1}, 593 cm^{-1} and Γ_1^+ (label A_{1g} in Chapter 4) at a frequency of 712 cm^{-1} - are at the zone-center and five modes - K_3 at the frequencies of 153*i* cm^{-1}, 228 cm^{-1}, 407 cm^{-1} and K_1 at the frequencies 266 cm^{-1}, 533 cm^{-1} - are at the zone-boundary. The most significant contributions -0.967 and 0.175 are those of the unstable K_3 mode at a frequency of 153*i* cm^{-1} and the stable Γ_2^- mode, at a frequency of 85 cm^{-1}, respectively. This confirms that the ferroelectric transition mainly comes from the condensation of K_3 and Γ_2^- in the paraelectric phase [16]. However, as it will be further discussed later the inclusion of these only two ionic degrees of freedom is not sufficient to properly account of the strain relaxation, which requires the additional explicit treatment of the coupling with Γ_1^+ mode at a frequency of 712 cm^{-1} even if the contribution is small ($\alpha_{\Gamma_1^+} = -0.067$). Finally, contrary to what was first expected by Aken *et al.* [15], the contributions of K_1 modes are negligible.

Once we identified the relevant phonon modes, we constructed an atomic distortion vector Δ^{model} as a sum of contributions α_i of modes *i* limited to the relevant modes (Table 5.3). Since different K_3 and Γ_2^- contribute to the distortion, we defined a combination of modes ξ_i such that

$$\Delta^{\text{model}} = A\sum \alpha_i \eta_i = \xi_{K_3} + \xi_{\Gamma_2^-} + \xi_{\Gamma_1^+}, \tag{5.1}$$

where ξ_{K_3}, $\xi_{\Gamma_2^-}$ and $\xi_{\Gamma_1^+}$ are the combined distortion amplitudes of relevant K_3, Γ_2^- and Γ_1^+ modes, respectively, that are

$$\xi_{K_3} = A\cdot(-0.967\cdot\eta_{K_3}(153i) + 0.162\cdot\eta_{K_3}(228) - 0.062\cdot\eta_{K_3}(407)), \quad (5.2)$$

$$\xi_{\Gamma_2^-} = A\cdot(0.175\cdot\eta_{\Gamma_2^-}(85) - 0.003\cdot\eta_{\Gamma_2^-}(410) + 0.001\cdot\eta_{\Gamma_2^-}(593)), \quad (5.3)$$

$$\xi_{\Gamma_1^+} = A\cdot(-0.067\cdot\eta_{\Gamma_1^+}(712)). \quad (5.4)$$

The advantage to construct the atomic distortion vector using the phonon eigendisplacements is the possibility at any moment to extend the model including additional degrees of freedom with no influence on the previous results. The alternative way is to decompose the atomic distortions Δ, obtained from atomic positions (see Table 5.1), into the symmetry-adapted modes [16].

Atom	$\Delta^{model}(x,z)$ (Å)		$\xi_{K_3}(x,z)$ (Å)		$\xi_{\Gamma_2^-}(z)$ (Å)	$\xi_{\Gamma_1^+}(z)$ (Å)
Y_1	0	0.2950	0	0.3252	-0.03025	0
Y_2	0	-0.1929	0	-0.1626	-0.03026	0
Mn	0	0.0162	0	0	0.0162	0
O_{ap1}	-0.1649	-0.0141	-0.1649	0	0.0167	-0.0308
O_{ap2}	0.1649	0.0474	0.1649	0	0.0167	0.0308
O_{pl3}	0	-0.2469	0	-0.3260	0.0791	0
O_{pl4}	0	0.2421	0	0.1630	0.0791	0

Table 5.3 Atomic distortion vector Δ^{model} decomposed into amplitudes of relevant phonon modes $K_3(153i)$, $\Gamma_2^-(85)$ and $\Gamma_1^+(712)$ of paraelectric $YMnO_3$. Space group: *P6₃/mmc*.

As we can see in Table 5.3, the inclusion of 7 amongst the 90 modes reproduce well the atomic distortion vector Δ (Table 5.1): the correspondence is within 1.5 % and 7 % along *x*- and *z*-axis, respectively. The atomic distortions of the apical oxygen atoms O_{ap1} and O_{ap2}

along *z*-axis differ more, but the included Γ_1^+ mode imposes the correct distortion direction - opposing displacements along the ferroelectric *z*-axis (Figure 5.1). We don't treat well the position of manganese atom Mn in *ab* plane because our approximation doesn't include K_1 mode, which is associated to the motions of apical oxygen atoms O_{ap1} and O_{ap2} and manganese atom Mn in *ab* plane (Figure 5.1). The atomic distortion of Mn atom (Table 5.4) is by two orders of magnitude smaller than the distortions of other atoms (Table 5.3) thus the contribution of this mode is negligible.

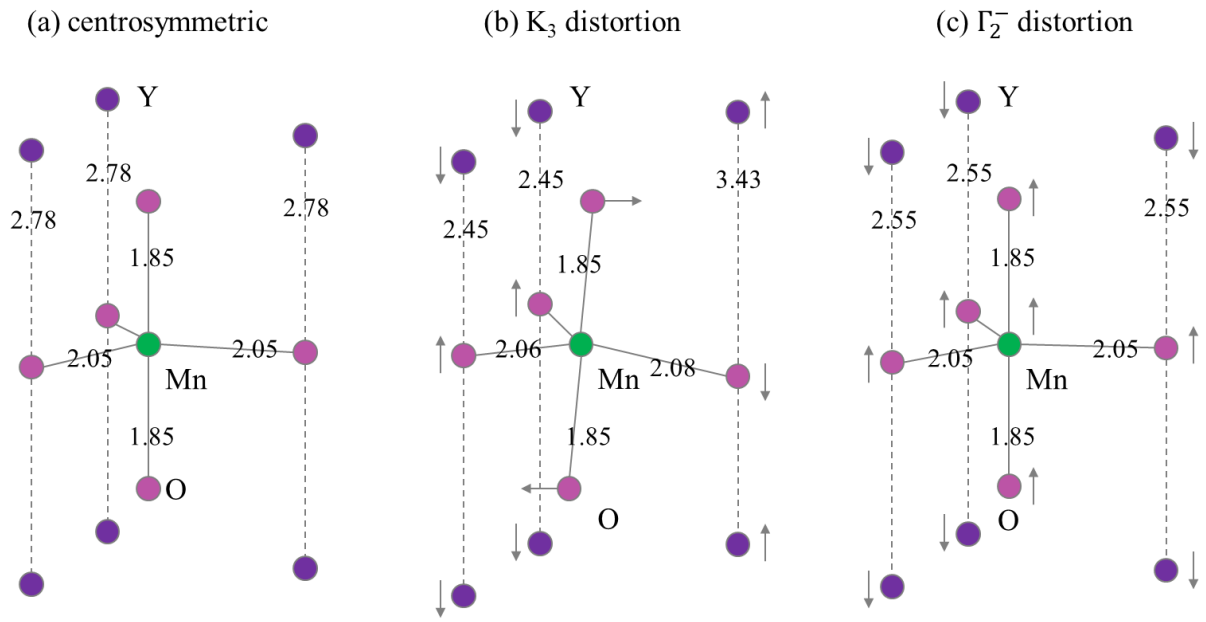

Figure 5.1 Schematic view of the MnO_5 triangular bipyramids surrounded by Y layers and corresponding measured atomic positions, when Γ_1^+ (b) and K_1 (c) distortions are frozen in the paraelectric phase of $YMnO_3$ (a). The numbers give the bond lengths in Å. The arrows indicate the directions of the atomic displacements with respect to the centrosymmetric structure.

The atomic distortion of the K_3 mode, listed in Table 5.3 and illustrated in Figure 5.2, is associated to displacements with the biggest amplitude compare to those of other modes. This mode is associated to the rotations of MnO_5 triangular bipyramids maintaining the Mn-O

atomic distances and Mn atoms at the center of the oxygen bipyramids and the displacements of Y atoms approaching the in-plane O atoms (see Figure 5.2). The K_3 mode is non-polar as the displacements of Y_1 and in-plane O atoms are compensated by the opposing displacements of two Y_2 and two in-plane O atoms along *z* direction, respectively (see Table 5.3). Equally, the opposing displacements of apical O atoms compensate each other along *x* direction.

Atom	$\xi_{K_1}(x)$ (Å)
Y_1	0
Y_2	0
Mn	0.0011
O_{ap1}	-0.0025
O_{ap2}	-0.0025
O_{ap3}	0
O_{ap4}	0

Table 5.4 Distortion amplitude (Å) of K_1 modes along [100] (in-plane axis) and [001] (polar axis) of paraelectric $YMnO_3$, respectively. The distortions were estimated as follows $\xi_{K_1} = A \cdot (-0.002 \cdot \eta_{K_1}(266) + 0.006 \cdot \eta_{K_1}(533))$.

As can be seen in Table 5.3, the Γ_2^- mode is polar and is associated to atomic displacements along *z* direction. These displacements are shown in Figure 5.2. The MnO_5 bipyramids move in opposite direction to that of the planes of Y atoms. The displacements do not compensate each others and lead to a ferroelectric polarization along *z* direction. Similarly to the displacements associated to the K_3 mode, when Γ_2^- mode is condensed into the paraelectric structure of $YMnO_3$, the Y-O bond length gets shorter, while the Mn-O atomic distance remains unchanged.

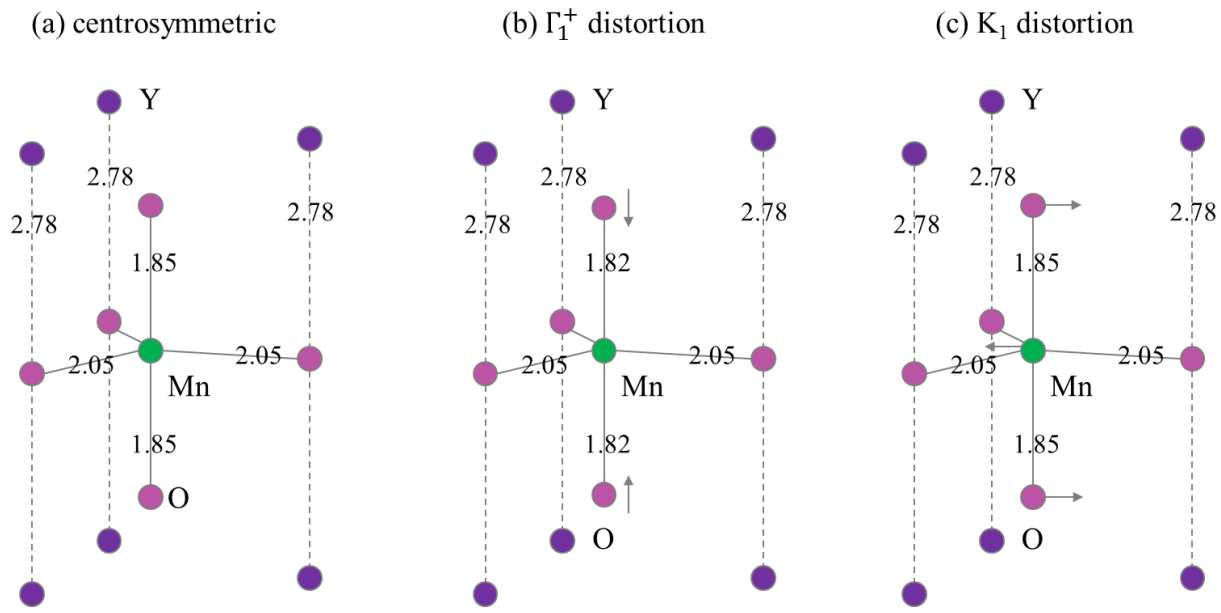

Figure 5.2 Schematic view of MnO_5 triangular bipyramids surrounded by Y layers and correspondent measured atomic positions, when K_3 (b) and Γ_2^- (c) distortions are frozen in the paraelectric phase of $YMnO_3$ (a). The numbers give the bond length in Å. The arrows indicate the directions of the atomic displacements with respect to the centrosymmetric structure.

5.2 First-principles based model energy

Since only few phonon modes are involved in the ferroelectric phase transition of $YMnO_3$, we now construct a model that consists in a Taylor expansion of the internal energy *U* (limited to low orders, in eV / formula units) around the paraelectric phase (taken as a reference) in terms of the relevant ionic and strain degrees of freedom (Eq. 5.5).

In the model, Q_{K_3}, $Q_{\Gamma_2^-}$ and $Q_{\Gamma_1^+}$ represent the amplitudes of the atomic distortions ξ_{K_3}, $\xi_{\Gamma_2^-}$ and $\xi_{\Gamma_1^+}$ that have been frozen. By construction, the ferroelectric ground state corresponds to $Q_{K_3} = Q_{\Gamma_2^-} = Q_{\Gamma_1^+} = 1$. The polynomial invariants were generated using the ISOTROPY software [61].

$$
\begin{aligned}
U = & -1.450\cdot Q_{\mathrm{K}_3}^2 + 1.138\cdot Q_{\mathrm{K}_3}^4 + 0.0193\cdot Q_{\Gamma_2^-}^2 - 0.0004\cdot Q_{\Gamma_2^-}^4 - 0.0010\cdot Q_{\Gamma_1^+} + 0.1710\cdot Q_{\Gamma_1^+}^2 \\
& + 0.0055\cdot Q_{\Gamma_1^+}^3 - 0.0009\cdot Q_{\Gamma_1^+}^4 - 0.462\cdot Q_{\mathrm{K}_3}^3\cdot Q_{\Gamma_2^-} + 0.217\cdot Q_{\mathrm{K}_3}^2\cdot Q_{\Gamma_2^-}^2 - 0.1022\cdot Q_{\mathrm{K}_3}^2\cdot Q_{\Gamma_1^+} \\
& - 0.0083\cdot \boxed{Q_{\mathrm{K}_3}^2\cdot Q_{\Gamma_1^+}^2} - 0.0062\cdot Q_{\Gamma_2^-}^2\cdot Q_{\Gamma_1^+} + 0.0026\cdot Q_{\Gamma_2^-}^2\cdot Q_{\Gamma_1^+}^2 \qquad 1 \\
& + 973\cdot\eta_a^2 + 445\cdot\eta_c^2 + 487\cdot\eta_a\cdot\eta_c - 3313\cdot\eta_a^3 - 1843\cdot\eta_c^3 - 1630\cdot\eta_a^2\cdot\eta_c - 160\cdot\eta_a\cdot\eta_c^2 \qquad 2 \\
& + 10.02\cdot\eta_a\cdot Q_{\mathrm{K}_3}^2 - 88\cdot\eta_a^2\cdot Q_{\mathrm{K}_3}^2 - 2.37\cdot\eta_a\cdot Q_{\mathrm{K}_3}^4 - 2.39\cdot\eta_c\cdot Q_{\mathrm{K}_3}^2 + 66\cdot\eta_c^2\cdot Q_{\mathrm{K}_3}^2 - 5.35\cdot\eta_c\cdot Q_{\mathrm{K}_3}^4 \\
& + 1.06\cdot\eta_a\cdot\eta_c\cdot Q_{\mathrm{K}_3}^2 + 19.1\cdot\eta_a\cdot\eta_c\cdot Q_{\mathrm{K}_3}^4 \\
& - 0.481\cdot\eta_a\cdot Q_{\Gamma_2^-}^2 - 0.082\cdot\eta_a\cdot Q_{\Gamma_2^-}^4 + \beta_{23}\cdot\boxed{\eta_c\cdot Q_{\Gamma_2^-}^2} + \beta_{43}\cdot\boxed{\eta_c\cdot Q_{\Gamma_2^-}^4} \\
& + 5.377\cdot\eta_a\cdot Q_{\Gamma_1^+} - 30.8\cdot\eta_a^2\cdot Q_{\Gamma_1^+} - 0.302\cdot\eta_a\cdot Q_{\Gamma_1^+}^2 + 1.2\cdot\eta_a^2\cdot Q_{\Gamma_1^+}^2 + \gamma_{31}\cdot\boxed{\eta_a\cdot Q_{\Gamma_1^+}^3} + \gamma_{41}\cdot\boxed{\eta_a\cdot Q_{\Gamma_1^+}^4} \\
& - 9.31\cdot\eta_c\cdot Q_{\Gamma_1^+} + 56.9\cdot\eta_c^2\cdot Q_{\Gamma_1^+} - 0.71\cdot\eta_c\cdot Q_{\Gamma_1^+}^2 + \gamma_{33}\cdot\boxed{\eta_c\cdot Q_{\Gamma_1^+}^3} + \gamma_{43}\cdot\boxed{\eta_c\cdot Q_{\Gamma_1^+}^4} \\
& + 0.69\cdot\eta_a\cdot Q_{\mathrm{K}_3}^3\cdot Q_{\Gamma_2^-} - 0.267\cdot\eta_a\cdot Q_{\mathrm{K}_3}^2\cdot Q_{\Gamma_2^-}^2 + 2.57\cdot\eta_c\cdot Q_{\mathrm{K}_3}^3\cdot Q_{\Gamma_2^-} - 1.33\cdot\eta_c\cdot Q_{\mathrm{K}_3}^2\cdot Q_{\Gamma_2^-}^2 \\
& - 0.659\cdot\eta_a\cdot Q_{\mathrm{K}_3}^2\cdot Q_{\Gamma_1^+} + 4.5\cdot\eta_a^2\cdot Q_{\mathrm{K}_3}^2\cdot Q_{\Gamma_1^+} + \tau_{221}\cdot\boxed{\eta_a\cdot Q_{\mathrm{K}_3}^2\cdot Q_{\Gamma_1^+}^2} + 0.878\cdot\eta_c\cdot Q_{\mathrm{K}_3}^2\cdot Q_{\Gamma_1^+} \\
& + \tau_{223}\cdot\boxed{\eta_c\cdot Q_{\mathrm{K}_3}^2\cdot Q_{\Gamma_1^+}^2} \\
& + \mu_{211}\cdot\boxed{\eta_a\cdot Q_{\Gamma_2^-}^2\cdot Q_{\Gamma_1^+}} + \mu_{221}\cdot\boxed{\eta_a\cdot Q_{\Gamma_2^-}^2\cdot Q_{\Gamma_1^+}^2} + \mu_{213}\cdot\boxed{\eta_c\cdot Q_{\Gamma_2^-}^2\cdot Q_{\Gamma_1^+}} + \mu_{223}\cdot\boxed{\eta_c\cdot Q_{\Gamma_2^-}^2\cdot Q_{\Gamma_1^+}^2}. \qquad 3
\end{aligned}
$$

(5.5)

The values of polynomial coefficients are the first-principles fitting parameters and were obtained independently from the systematic total energy calculations. We computed the

energy potentials by freezing the amplitudes of the atomic distortions ξ_{K_3}, $\xi_{\Gamma_2^-}$ and $\xi_{\Gamma_1^+}$ to reference paraelectric structure in a range of [-1, 1] with step of 0.25 fractional units. The obtained energy potentials were fitted with the 4th order polynomial function. The effect of the epitaxial strain to K_3, Γ_2^- and Γ_1^+ modes was estimated in the range of [-3%, 3%] with step of 1%. We considered that the coefficients were negligible when the change of total energy was of the order of the calculations error of 1 meV. Note that the negligible terms in (5.5) are delineated by full line rectangles. The model construction required a big number of about 2000 calculations to be performed and treated. The detailed description and the energy potential curves for each coefficient are given in Appendix C.

In the following, we discuss the related terms delineated by dashed-line rectangles numbered from 1 to 3.

The terms in the first dashed-line rectangle form the core of our model. They define the energy potentials of individual K_3, Γ_2^- and Γ_1^+ modes (Q_{K_3}, $Q_{\Gamma_2^-}$, $Q_{\Gamma_1^+}$, respectively) and coupling between each others: K_3 and Γ_2^-, K_3 and Γ_1^+, Γ_2^- and Γ_1^+ modes ($Q_{K_3}Q_{\Gamma_2^-}$, $Q_{K_3}Q_{\Gamma_1^+}$ and $Q_{\Gamma_2^-}Q_{\Gamma_1^+}$, respectively).

As expected, the coefficient of $Q_{K_3}^2$ is negative, which is coherent with the mode instability. The coefficient of $Q_{\Gamma_2^-}^2$ is positive and is renormalized by the positive biquadratic coupling coefficient between K_3 and Γ_2^-. This means that the K_3 mode doesn't tend to decrease the stability of Γ_2^- mode. Rather it shifts the Γ_2^- mode to a nonzero equilibrium position (see in Appendix Figure C.4, [16]) through the term $Q_{K_3}^3 Q_{\Gamma_2^-}$. It is the linear coupling of the unstable non-polar K_3 mode with the stable polar Γ_2^- mode that results in a finite polarization in the ferroelectric *P6$_3$cm* phase.

The coefficient of $Q_{\Gamma_1^+}^2$ is positive, but the coupling coefficient between K_3 and Γ_1^+ is negative meaning that the unstable non-polar K_3 mode also couples with the stable non-polar Γ_1^+ mode. The coupling coefficients of $Q_{K_3}^2 Q_{\Gamma_1^+}$ and $Q_{K_3}^2 Q_{\Gamma_1^+}^2$ renormalize the coefficients of

$Q_{\Gamma_1^+}$ and $Q_{\Gamma_1^+}^2$. They are negative meaning that K_3 tends to decrease the stability of Γ_1^+. We neglected the mode coupling term $Q_{K_3}^2 Q_{\Gamma_1^+}^2$ as the dependence in the coefficient curve (see in Figure C.6 in Appendix C) is linear.

The coupling between Γ_2^- and Γ_1^+ modes is weak as the value of coupling coefficient of $Q_{\Gamma_2^-}^2 Q_{\Gamma_1^+}$ is small.

We extended our model with the macroscopic strain degrees of freedom (dashed-line rectangle 2 and 3) in order to study the epitaxial $YMnO_3$ thin films under the imposed mechanical boundary conditions – epitaxial strain imposed by the substrate.

The expansion of elastic energy in terms of the in-plane η_a and out-of-plane strain η_c for the hexagonal structure (since the lattice parameters *a* = *b*, we imposed $\eta_a = \eta_{xx} = \eta_{yy}$) is shown in the second rectangle. We expended the energy till the third order to treat the asymmetry appearing from the different responses to compressive and tensile strain (see in Appendix C Figure C.10). As expected the system is more sensitive to compressive in-plane strain. The in-plane compression results in out-of-plane expansion that favors the ferroelectricity.

The terms in the third dashed-line rectangle define the response to applied strain of individual K_3, Γ_2^- and Γ_1^+ modes ($\eta_{a,c} Q_{K_3}$, $\eta_{a,c} Q_{\Gamma_2^-}$ and $\eta_{a,c} Q_{\Gamma_1^+}$, respectively) and mode coupling terms ($\eta_{a,c} Q_{K_3} Q_{\Gamma_2^-}$, $\eta_{a,c} Q_{K_3} Q_{\Gamma_1^+}$ and $\eta_{a,c} Q_{\Gamma_2^-} Q_{\Gamma_1^+}$).

Both K_3 and Γ_1^+ modes significantly couple with strain while the coupling of Γ_2^- mode with in-plane strain is weak and with out-of-plane strain is negligible (terms $\eta_c Q_{\Gamma_2^-}^2$ and $\eta_c Q_{\Gamma_2^-}^4$). As follows, the strain mode coupling terms of K_3 and Γ_2^-, K_3 and Γ_1^+ modes give a contribution to strain relaxation while the mode coupling terms of Γ_2^- and Γ_1^+ modes are negligible. Note that the high order terms of Γ_1^+ mode ($\eta_a Q_{\Gamma_1^+}^3$, $\eta_a Q_{\Gamma_1^+}^4$, $\eta_c Q_{\Gamma_1^+}^3$ and $\eta_c Q_{\Gamma_1^+}^4$) and mode coupling terms of K_3 and Γ_1^+ modes ($\eta_a Q_{K_3}^2 Q_{\Gamma_1^+}^2$ and $\eta_c Q_{K_3}^2 Q_{\Gamma_1^+}^2$) are negligible. This suggests that the

atomic distortions of Γ_1^+ mode are induced via the coupling of K_3 mode with strain since K_3 couples stronger with strain than Γ_1^+.

5.3 Ground state of bulk $YMnO_3$

As a first step, we verified to which accuracy our model (Eq. 5.5) can reproduce the ferroelectric ground state of $YMnO_3$. We minimized the energy expansion (Eq. 5.5) in terms of the relevant K_3, Γ_2^- and Γ_1^+ mode amplitudes Q_{K_3}, $Q_{\Gamma_2^-}$ and $Q_{\Gamma_1^+}$, respectively, in-plane η_a and out-of-plane strain η_c to know whether in freezing our chosen degrees of freedom to *P6₃/mmc* paraelectric high-temperature phase, we go down to the *P6₃cm* ferroelectric ground state of $YMnO_3$. Then, we calculated the total energy *E* and the ferroelectric polarization P_0 (Eq. 5.8) at the minimum. Table 5.5 lists the energy minimum and related distortion amplitudes of our model (Model 0) in comparison to the first-principles calculations performed within LSDA+*U* for the ferroelectric phase of $YMnO_3$ (a*b-initio*). We also consider 8 alternative models excluding certain terms.

As we can see in Table 5.5, our model (Model 0) properly reproduces the bulk ferroelectric ground-state (*ab-initio*): the mode amplitudes, energy and polarization agree within 3 % and the strain values within 10 %.

In the following, we explore the influence of certain terms excluding them from the model in order to understand better their role. First, we analyze the necessity to include the Γ_1^+ mode.

If we exclude the Γ_1^+ mode, the model doesn't treat well the strain relaxation (see Model 1 in Table 5.5). The values of the in-plane η_a and out-of-plane strain η_c are almost twice smaller than the ones obtained from *ab-initio* calculations, the mode amplitudes, energy and polarization are reproduced less precise within 13 %. Thus, the Γ_1^+ mode is necessary to properly account for the strain relaxation.

	Q_{K_3}	$Q_{\Gamma_2^-}$	$Q_{\Gamma_1^+}$	η_a (%)	η_c (%)	E (eV)	P_0 (μC/cm^2)
ab-initio	1.000	1.000	1.000	-1.19	2.07	-0.706	7.51
Model 0	1.007	0.974	0.999	-1.31	2.23	-0.712	7.31
Model 1	0.931	0.888	0	-0.61	0.86	-0.612	6.66
Model 2	0.942	0.906	0.276	-0.62	0.89	-0.625	6.80
Model 3	1.012	1.002	1.017	-1.36	2.28	-0.715	7.52
Model 4	1.039	1.003	1.117	-1.46	2.63	-0.738	7.53
Model 5	0.905	0.876	0.368	-0.17	0.36	-0.588	6.57
Model 6	0.938	0.902	0.245	-0.60	0.85	-0.622	6.77
Model 7	0.954	0.916	0.498	-0.94	1.50	-0.639	6.88
Model 8	0.969	0.932	0.650	-1.10	1.81	-0.650	6.99

Table 5.5 Minimum of our first-principles based model (Model 0) for $YMnO_3$ in comparison to LSDA+U data (*ab-initio*) in terms of amplitudes Q of K_3, Γ_2^- and Γ_1^+ modes (in fractional units), in-plane and out-of-plane strain η_a and η_c, total energy E and bulk polarization P_0, respectively. Alternative models when excluded from Eq. 5.5 the terms of 1: Γ_1^+ mode, 2: Γ_1^+ strain individual mode $\eta_{a,c}Q_{\Gamma_1^+}$ and strain mode coupling $\eta_{a,c}Q_{K_3}Q_{\Gamma_1^+}$ and $\eta_{a,c}Q_{\Gamma_2^-}Q_{\Gamma_1^+}$ 3: Γ_2^- and Γ_1^+ mode coupling $Q_{\Gamma_2^-}Q_{\Gamma_1^+}$ and Γ_2^- strain individual mode coupling $\eta_a Q_{\Gamma_2^-}$, 4: K_3 and Γ_2^- strain mode coupling $\eta_{a,c}Q_{K_3}Q_{\Gamma_2^-}$, 5: K_3 strain individual mode coupling $\eta_{a,c}Q_{K_3}$, 6: Γ_1^+ strain individual mode coupling $\eta_{a,c}Q_{\Gamma_1^+}$, 7: K_3 and Γ_1^+ mode coupling $Q_{K_3}Q_{\Gamma_1^+}$, 8: K_3 and Γ_1^+ mode coupling $Q_{K_3}Q_{\Gamma_1^+}$ and strain mode coupling $\eta_{a,c}Q_{K_3}Q_{\Gamma_1^+}$.

If we exclude just the strain coupling terms $\eta_{a,c}Q_{\Gamma_1^+}$, $\eta_{a,c}Q_{K_3}Q_{\Gamma_1^+}$ and $\eta_{a,c}Q_{\Gamma_2^-}Q_{\Gamma_1^+}$ of Γ_1^+ mode (see Model 2 in Table 5.5), the model results with respect to *ab-initio* calculations are slightly improved (correspondence within 12% for the mode K_3 and Γ_2^- amplitudes, energy and polarization), but still the strain η_a and η_c values remain unchanged and the amplitude of Γ_1^+

mode is not well estimated. This confirms that Γ_1^+ mode is induced via the coupling with strain.

Next, we analyze the role of the Γ_2^- mode in the model.

As discussed and concluded in Section 5.2, the coupling between Γ_2^- and Γ_1^+ modes and Γ_2^- individual mode with strain is weak as the polynomial coefficients of the terms $Q_{\Gamma_2^-}Q_{\Gamma_1^+}$ and $\eta_a Q_{\Gamma_2^-}$, respectively, are small and might be probably excluded from the model (Eq. 5.5). As we can see in Table 5.5 (see Model 3), the model results in this case are slightly overestimated, but still in satisfactory agreement with the *ab-initio* calculations. The mode amplitudes, energy and polarization are reproduced more precisely (within 2 %), but the coupling with strain is not so good (the strain η_a and η_c values are reproduced within 14 %) compare to the *ab-initio* calculations.

If, in the following, we exclude the strain mode coupling terms $\eta_{a,c}Q_{\mathrm{K}_3}Q_{\Gamma_2^-}$ of K_3 and Γ_2^- modes (Model 4), we observe that the amplitude of Γ_2^- mode remains almost unchanged and the other parameters are highly overestimated. The strain relaxation is again worst (within 27 %).

Concluding, the Model 3 and Model 4 results confirm that Γ_2^- mode is not sensitive to strain, but this mode contribute to define well the strain relaxation.

Last, we analyze the coupling with strain of the K_3 and Γ_1^+ modes.

In the previous Section 5.2, we posed that K_3 mode couples with strain stronger than Γ_1^+ mode. In order to check it, we excluded, once, the terms $\eta_{a,c}Q_{\mathrm{K}_3}$ that define the K_3 individual mode coupling with strain (Model 5), next, the terms $\eta_{a,c}Q_{\Gamma_1^+}$ that define the Γ_1^+ individual mode coupling with strain (Model 6). We notice that both model results are strongly underestimated compare to the *ab-initio* results, in particular, the strain values and the amplitude of Γ_1^+ mode. These values are not so well estimated in case when the coupling with

strain of K_3 mode is absent (Model 5), which confirms that the coupling with strain of K_3 mode is stronger than that of Γ_1^+ mode.

Then, in order to check whether the coupling of K_3 and Γ_1^+ individual modes or the coupling of K_3 and Γ_1^+ individual modes with strain is more significant to define properly the strain relaxation, we exclude, once, the terms $Q_{K_3}Q_{\Gamma_1^+}$ (Model 7) and, next, in addition the terms $\eta_{a,c}Q_{K_3}Q_{\Gamma_1^+}$ (Model 8), respectively. We observe that the results obtained within Model 7 and Model 8 configurations are less accurate compared to *ab-initio* results. In the following, we notice that Model 7 values are further away from the *ab-initio* values than Model 8 results. This means that the coupling of K_3 and Γ_1^+ individual modes itself is more significant than their coupling with strain.

5.4 Mechanical and electrical boundary conditions in $YMnO_3$ thin films

In this section, we apply our constructed first-principles model to study the epitaxial $YMnO_3$ thin films. The main difference comparing to the bulk case is that (i) the thin film is constrained by the substrate meaning that it is under the imposed mechanical boundary conditions and (ii) the electric field within the film depends on the electrical boundary conditions.

5.4.1 Introduction

In order to treat the mechanical and electrical boundary conditions in a real system, we consider a model ferroelectric capacitor structure under finite bias V_b as shown in Figure 5.3.

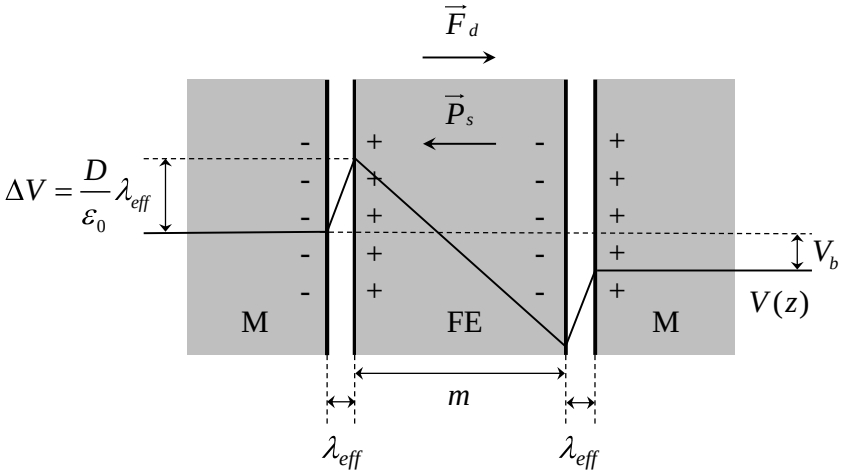

Figure 5.3 Structure of ferroelectric capacitor: a ferroelectric film of *m* thickness (FE) between two ideal metallic (M) electrodes with applied bias V_b separated by a region of thickness λ_{eff}. The vectors $\vec{P}_s$ and $\vec{F}_s$ show the orientation of the spontaneous polarization and depolarizing field, respectively. ΔV, the potential drop across the interface.

As it has been proposed recently [62], the electric enthalpy *F* of ferroelectric capacitor can be written as:

$$F = mU + \beta_{el} P_z^2 + S\beta_{el}^b P_z V_b, \tag{5.6}$$

where the first term corresponds to the internal energy *U* as described by our model (Eq. 5.5), the other two terms correspond to an additional electrostatic energy dependent on the electrical boundary conditions. The latter are fixed by two independent parameters: the screening length of the electrodes λ_{eff} and the applied bias V_b.

The coefficient β_{el} in Eq. 5.6 is given by

$$\beta_{el} = \frac{\lambda_{eff} S}{\varepsilon_0 (1 + 2\frac{\lambda_{eff} S \varepsilon_\infty}{m\Omega_0})}, \tag{5.7}$$

where $\Omega_0 = 364.86\ \text{Å}^3$ is the volume and $S = 32.84\ \text{Å}^2$ is the surface of one unit cell of paraelectric $YMnO_3$ (LSDA+*U*, Chapter 3); *m* is the thickness of the thin film expressed in

terms of the number of layers, λ_{eff} is the effective screening length in Angstroms, $\varepsilon_0 = 8.85 \cdot 10^{-12}$ is the permittivity of vacuum and $\varepsilon_\infty = 6.46$ [57] is the optical dielectric constant.

The spontaneous polarization P_z is induced by the polar Γ_2^- mode with the atomic displacements along the ferroelectric *z*-axis and in Eq. 5.6 is:

$$P_z = \frac{Z_{zz}^*}{\Omega_0} Q_{\Gamma_2^-}, \tag{5.8}$$

where Z_{zz}^* is the diagonal component of the LSDA+*U* Born effective charges reported in Chapter 4 (see Table 4.4), $Q_{\Gamma_2^-}$ is the amplitude of the atomic distortion of Γ_2^- mode defined in Eq. 5.3.

The coefficient β_{el}^b in Eq. 5.6 is given by

$$\beta_{el}^b = \frac{1}{1 + 2\dfrac{\lambda_{eff} S \varepsilon_\infty}{m\Omega_0}}. \tag{5.9}$$

The term $\beta_{el} P_z^2$ in Eq. 5.6 takes into account the effect of the incomplete screening of the depolarizing field by the metallic electrodes. It renormalizes the term $Q_{\Gamma_2^-}^2$ in our model (Eq. 5.5) and tends to suppress the polarization since the parameter β_{el} is always positive.

In what follows, we will restrict our investigations to capacitor without applied bias ($V_b = 0$). We will investigate the evolution of the ferroelectric properties with the quality of screening provided by the electrodes.

In the limit of $\lambda_{eff} \to \infty$, the system is under the open-circuit conditions. The coefficient of $\beta_{el} P_z^2$ term is written as

$$\beta_{el} P_z^2 = \frac{m\Omega_0}{2\varepsilon_0 \varepsilon_\infty} \left(\frac{Z_{zz}^*}{\Omega_0} \right)^2 Q_{\Gamma_2^-}^2. \tag{5.10}$$

In case of perfect screening ($\lambda_{eff} \to 0$), the tem $\beta_{el} P_z^2 \to 0$ and this yields in short-circuit. Then we can analyze the system under the imperfect screening conditions for finite value λ_{eff} choosing the typical value in perovskites of an effective screening length of 0.25 Å (Eq. 5.6).

Note that when the system is under the open-circuit conditions, not only the ionic contribution (Eq. 5.7), but also the electronic contribution is taken into account to total polarization. The decomposition is allowed by the application of the Born-Oppenheimer approximation when the total polarization of the system P_z is written as a sum of an ionic contribution P_{ion} and an electronic contribution P_{el}:

$$P_z = P_{el} + P_{ion} = \varepsilon_0 \chi_\infty E + \frac{Z^*_{zz}}{\Omega_0} Q_{\Gamma_2^-}, \tag{5.11}$$

where χ_∞ is the optical susceptibility defined as $\varepsilon_\infty = 1 + \chi_\infty$, E is the electric field expressed via the electronic polarization with the electric displacement $D = 0$ as $E = -\frac{P_{ion}}{\varepsilon_0 \varepsilon_\infty}$. In the following, the total polarization in *z* direction under the open-circuit conditions is:

$$P_z = \frac{1}{\varepsilon_\infty} \frac{Z^*_{zz}}{\Omega_0} Q_{\Gamma_2^-}. \tag{5.12}$$

As we can see, in Eq.5.12, the spontaneous polarization is not only dependent on the Born effective charges Z^* and atomic distortions $Q_{\Gamma_2^-}$ (see Eq. 5.8), but also on the optical dielectric constant ε_∞, which causes the reduce of the polarization under the open-circuit conditions.

Finally, let us mention than an additional complication arises from the fact that $YMnO_3$ exhibits in its paraelectric centrosymmetric phase a non-vanishing formal polarization [63]. When dealing here with $YMnO_3$ films in open-circuit, we consider the stoechiometric films in a practical situation, where a given underlying mechanism (adsorbates, defects, …) appearing likely during the growth at high temperature, is screening the formal polarization, but we assume that this screening is frozen and that no additional screening of the ferroelectric

polarization is present (i.e. the displacement field of the paraelectric field is taken as zero [64]. In the case of a ferroelectric capacitor with ideal or real electrodes, we better refer to a symmetric configuration (i.e. with the same interface on both sides); in this case, the eventual imperfect screening of the formal polarization will simply produce the same jump of potential at both interfaces, without producing any field in the film.

5.4.2 Role of mechanical boundary conditions

In this section, we will consider thin films of $YMnO_3$ epitaxially grown on substrate under short-circuit conditions with a perfect screening of the depolarizing field. This enables the analysis of the role of mechanical boundary conditions imposed by a substrate independently from the electrical boundary conditions. In short-circuit, the results are independent of the film thickness.

Figure 5.4 shows our model results minimizing the Eq. 5.5 in terms of distortion amplitudes Q_{K_3}, $Q_{\Gamma_2^-}$, $Q_{\Gamma_1^+}$ and η_a or η_c (depending on which in-plane or out-of plane strain was varied) for a film of $YMnO_3$ under the mechanical boundary conditions in short-circuit, when the screening of the depolarizing field is perfect.

As we can see in Figure 5.4 (a), the amplitude of Γ_1^+ mode varies significantly from 1.62 to -0.62 on the applied in-plane strain η_a in the range from -3% to +3%. While the Γ_2^- and K_3 modes are just slightly strain dependent. The amplitudes of Γ_2^- and K_3 decrease with strain by 0.26 (from 1.04 to 0.78) and 0.32 (from 1.10 to 0.78) fractional units at $\eta_a = [-3\%, +3\%]$, respectively. This confirms once again that the Γ_1^+ mode plays an important role in treating the strain relaxation. Unfortunately, the amplitudes of Γ_2^- and K_3 modes are little sensitive to epitaxial strain and they cannot be expected to be tuned using the epitaxial strain favouring the ferroelectricity.

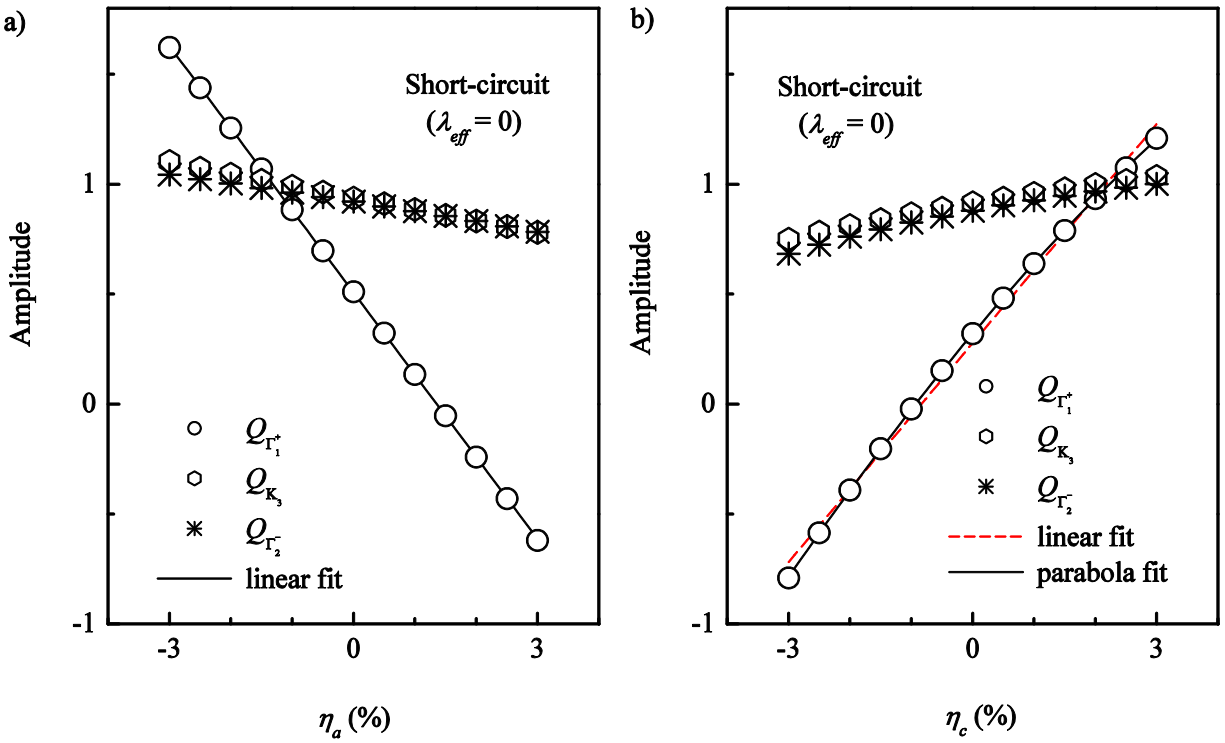

Figure 5.4 Evolution of the amplitudes of K_3, Γ_2^- and Γ_1^+ distortions in the *P6₃cm* ground state of epitaxial $YMnO_3$ thin films under short-circuit ($\lambda_{eff} = 0$) in terms of (a) in-plane epitaxial strain η_a imposed by the substrate and (b) out-of-plane strain η_c (at T = 0 K).

Similar results are observed minimizing the model (Eq. 5.5) in terms of Q_{K_3}, $Q_{\Gamma_2^-}$, $Q_{\Gamma_1^+}$ and η_a at various out-of-plane strain η_c (Figure 5.4, b). The amplitudes of Γ_2^- and K_3 modes are almost the same and show a similar coherent behaviour – slight increase with strain. The Q_{K_3} increases by 0.32 (from 0.75 to 1.04) fractional units at $\eta_c = [-3\%, +3\%]$ as decreases in case of η_a (Figure 5.4, a). The $Q_{\Gamma_2^-}$ increases by 0.32 (from 0.68 to 1.00) fractional unit at $\eta_c = [-3\%, +3\%]$, slightly more than decreases in case of η_a. The Γ_1^+ mode shows a strong dependence on strain. The $Q_{\Gamma_1^+}$ increases from -0.79 to 1.21 fractional units with out-of-strain in the range between -3 % and +3 % . In opposite to $Q_{\Gamma_2^-}$, the amplitude of Γ_1^+ mode increases less than decreases in case of in-plane strain η_a between -3 % and +3 % (Figure 5.4, a).

We observe that the distortions linearly decrease with in-plane strain η_a between -3 % and +3 % (Figure 5.4, a) and a slightly quadratic dependence on strain of distortion amplitudes is observed with out-of-plane strain η_c between -3 % and +3 % (Figure 5.4, b).

5.4.3 Role of electrical boundary conditions

Now when the role of mechanical boundary conditions in thin films of $YMnO_3$ is understood, in the present section, we discuss the role of electrical boundary conditions. We consider the system under open-circuit conditions, when the depolarizing field is not screened, and under the imperfect screening of depolarizing field conditions with the effective screening length $\lambda_{eff} = 0.25\,\text{Å}$. In this case, we considered a film thickness of 11.11 Å ($m = 1$). While in open-circuit, the results are independent of the thickness.

Figure 5.5 shows our model results for a film of $YMnO_3$ in the *P6₃cm* ground state obtained minimizing the Eq. 5.5 with the term $\beta_{el} P_z^2$ included (Eq. 5.10) in terms of the distortion amplitudes of K_3, Γ_2^- and Γ_1^+ modes and out-of plane strain η_c with various in-plane strain η_a between -3% and +3%. The polarization[4] *P* was calculated using Eq. 5.12 The bulk polarization P_0 equal to 7.31 $\mu C/cm^2$ was calculated using Eq. 5.8, when $Q_{\Gamma_2^-}$ is at a global minimum of our model (see Table 5.5). The bulk value η_{c0} equal to 2.23 % corresponds to a global minimum of our model (see Table 5.5).

As expected and shown in Figure 5.5 (a), the term $\beta_{el} P_z^2$ has an impact only to Γ_2^- mode, which amplitude under open-circuit conditions reduces comparing to the amplitude under short-circuit by a factor of 1.5 - 2.0 for $\eta_a = [-3\%, +3\%]$. In case of imperfect screening, the amplitude of Γ_2^- mode under open-circuit reduces (comparing to short-circuit) by a factor of 1.1 - 1.2 at $\eta_a = [-3\%, +3\%]$ and is in between short-circuit and open-circuit remaining closer

[4] The polarization *P*, in the following, unless stated differently, corresponds to the polarization along *z* direction P_z.

to perfect screening case. The direct change of $Q_{\Gamma_2^-}$ indirectly influences the amplitudes of K_3 and Γ_1^+ modes, but the effect is negligible. The Q_{K_3} and $Q_{\Gamma_1^+}$ remain almost constant under short-circuit and open-circuit conditions. For this reason, we didn't include in Figure 5.5 (a) the evolution of K_3 and Γ_1^+ mode amplitudes under imperfect screening conditions.

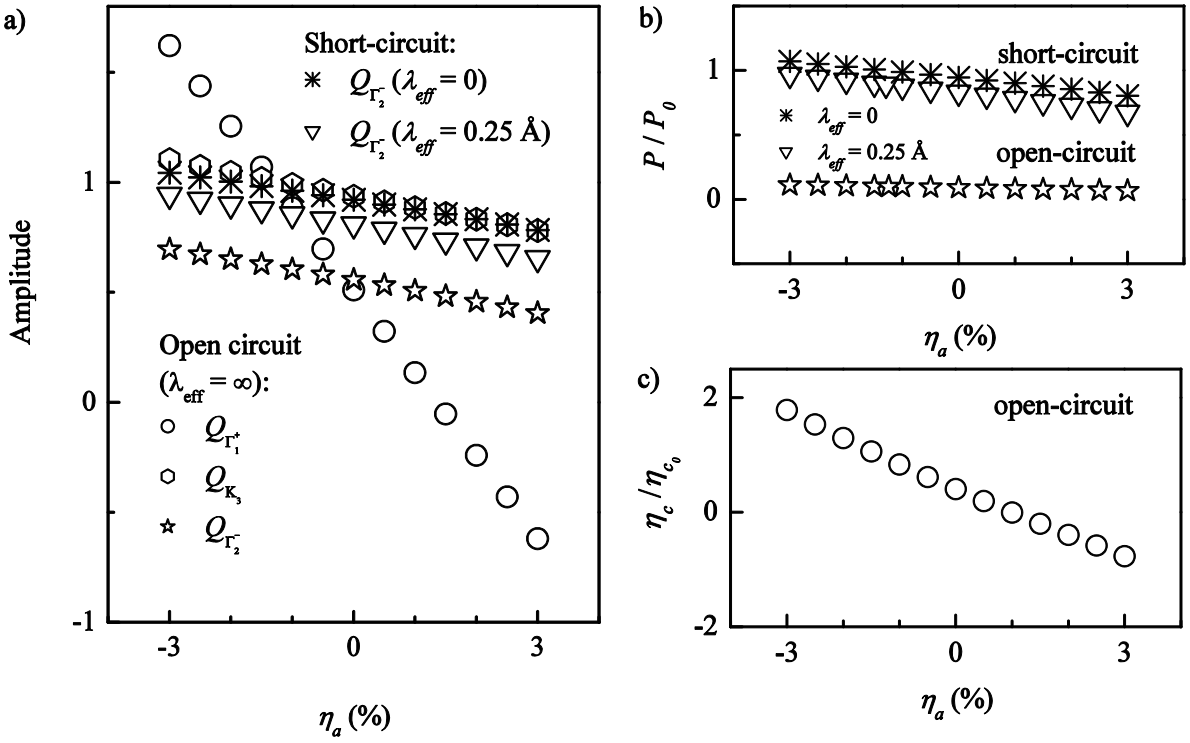

Figure 5.5 Evolution of (a) the amplitudes of K_3, Γ_2^- and Γ_1^+ distortions in fractional units, (b) the spontaneous polarization *P* (relative to the bulk polarization P_0), (c) the out-of-plane strain η_c (relative to the bulk value η_{c0}) in the $P6_3cm$ ground state of epitaxial $YMnO_3$ films under short-circuit ($\lambda_{eff}=0$ and $\lambda_{eff}=0.25$ Å ($m=1$)) and open-circuit ($\lambda_{eff}=\infty$) in terms of the in-plane epitaxial strain η_a imposed by the substrate (at T = 0 K).

The spontaneous polarization (Figure 5.5, b) in a film of ferroelectric $YMnO_3$ under open-circuit conditions is significantly reduced comparing to short-circuit by a factor of 10 - 13 at $\eta_a=[-3\%,+3\%]$, although the amplitude of Γ_2^- mode is reduced by a factor of 1.5 - 2.0 for

$\eta_a = [-3\%, +3\%]$. As discussed in Section 5.4.1, under open-circuit conditions purely electronic response to total polarization is taken into account through the optical dielectric constant ε_∞, which essentially causes the reduction of the polarization (see Eq. 5.8 and Eq. 5.12). Surprisingly, the polarization is reduced, but not supressed as expected for very thin films of proper ferroelectrics [65]. The system remains ferroelectric confirming the results obtained by Sai *et al*. [66]. Under the imperfect screening conditions, consistently with the amplitude of $Q_{\Gamma_2^-}$ mode, the polarization reduces less by a factor of $1.0 - 1.2$ at $\eta_a = [-3\%, +3\%]$.

As expected, under the compressive in-plane strain between -3 % and +3 % the system is elongated along *c*-axis (Figure 5.5, c) by a factor of 2.3 from 1.79 to -0.77 fractional units, respectively. The same tendency is obtained for short-circuit and imperfect screening conditions. The curves superpose and the size of a symbol is too big to see an effect. Thus we show the out-of-plane strain dependence on in-plane strain only under open-circuit conditions.

Figure 5.6 shows our model results minimizing Eq. 5.5 in terms of the amplitudes of K_3, Γ_2^- and Γ_1^+ modes and the in-plane strain η_a at out-of-plane strain η_c between -3 % and +3 % for a film of ferroelectric $YMnO_3$. The polarization *P* and the bulk polarization P_0 were determined in the same way as in Figure 5.5. The bulk value η_{a0} equal to -1.31 % corresponds to a global minimum of our model (see Table 5.5).

Comparing Figure 5.5 (a) to Figure 5.6 (a), the evolution of amplitudes of K_3, Γ_2^- and Γ_1^+ modes in case of uniaxial strain is in opposite direction than in case of epitaxial strain. The amplitudes are minimum under compressive 3% strain and maximum under a tensile 3% strain. The amplitude of Γ_2^- mode reduces comparing to short-circuit by a factor of 1.9 - 1.7 at $\eta_c = [-3\%, +3\%]$. Comparing to effect of epitaxial strain (Figure 5.6, a), the factor by which reduces polarization in open-circuit is bigger for compressive and smaller for tensile strain by a factor of 12 - 11 at $\eta_c = [-3\%, +3\%]$ (Figure 5.6, b) under open-circuit conditions, respectively. Under imperfect screening conditions ccomparing to effect of epitaxial strain,

similarly to open-circuit, the polarization is reduced more by a factor of 1.2 for compressive strain and reduced less by a factor of 1.1 for tensile strain at $\eta_c = [-3\%, +3\%]$.

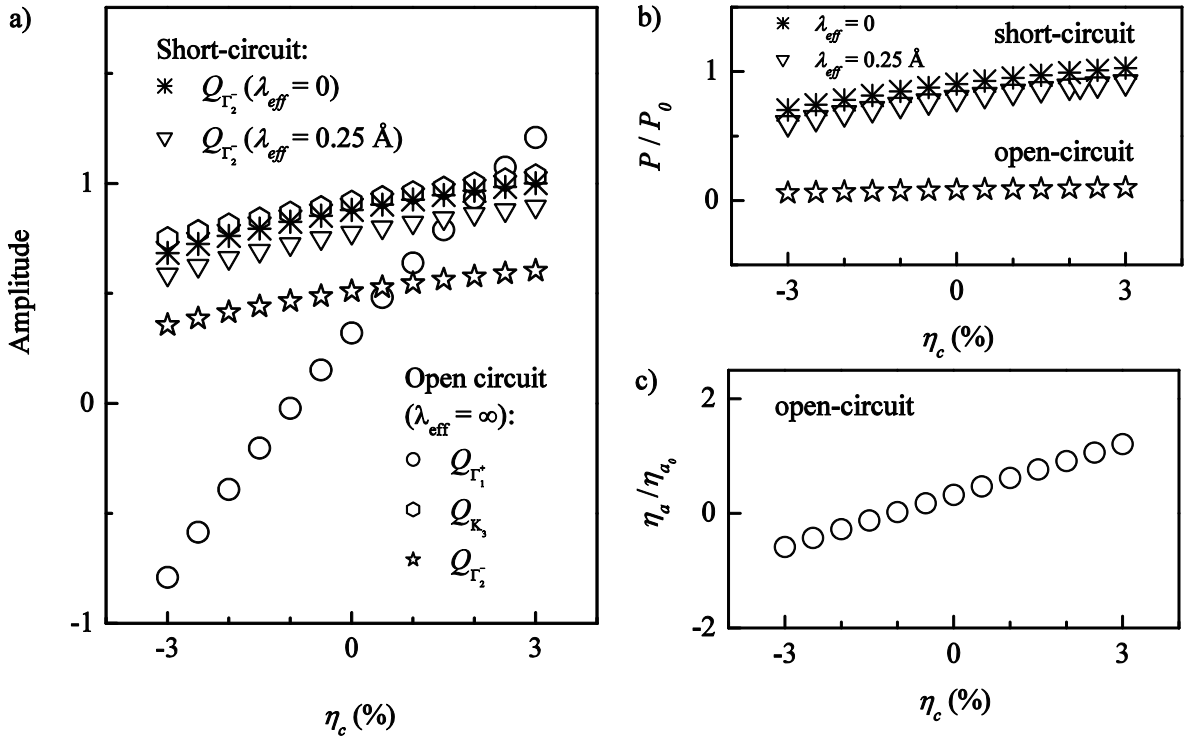

Figure 5.6 Evolution of (a) the amplitudes of K_3, Γ_2^- and Γ_1^+ distortions, (b) the spontaneous polarization *P* (relative to the bulk polarization P_0), (c) the in-plane strain η_a (relative to the bulk value η_{a0}) in the $P6_3cm$ ground state of $YMnO_3$ thin films under short-circuit ($\lambda_{eff}=0$ and $\lambda_{eff}=0.25$ Å ($m=1$)) and open-circuit ($\lambda_{eff}=\infty$) in terms of the out-of-plane strain η_c (at T = 0 K).

The behaviours of K_3 and Γ_1^+ modes (Figure 5.6, a) don't differ significantly under open-circuit, short-circuit and imperfect screening conditions. Although, the amplitudes of K_3 and Γ_1^+ modes distance more far with epitaxial than uniaxial strain. The amplitude of K_3 mode increases from 0.72 to 1.00 fractional units (open-circuit) and from 0.74 to 1.03 fractional units (imperfect screening) with strain between -3 % and +3 %. The amplitude of Γ_1^+ mode

increases from -0.82 to 1.19 fractional units (open-circuit) and from -0.80 to 1.21 fractional units (imperfect screening). As we can see, in case of imperfect screening, the amplitudes of K_3 and Γ_1^+ modes are slightly smaller than in case of imperfect screening, but too small to be included into the graph. Thus we didn't show the evolution of Q_{K_3} and $Q_{\Gamma_1^+}$ under the imperfect screening conditions in Figure 5.6 (a).

In case of uniaxial strain, the in-plane strain (Figure 5.6, c) is less sensitive to out-of-plane strain in the range from -3 % to +3 %. The strain value increases from -0.58 to 1.21 by a factor of 2.1, respectively. The dependence is similar to that for imperfect screening.

5.5 Conclusions

In this chapter, we discussed a model built from first principles describing the properties of epitaxial $YMnO_3$ thin films under the mechanical and electrical boundary conditions.

Our first-principles calculations confirmed that the ferroelectric distortion is mainly coming from the unstable zone-boundary K_3 mode of the paraelectric phase, at a frequency of $153i$ cm^{-1} and the stable zone-center Γ_2^- mode, at a frequency of 85 cm^{-1}. However, the proper strain relaxation mandatory required the inclusion of Γ_1^+ mode. Our analysis showed that the Γ_1^+ mode is induced via the K_3 mode coupling with strain. Contrary to K_3 and Γ_1^+ modes, the polar Γ_2^- mode showed a weak coupling with strain.

Our first-principles model properly reproduced the bulk ferroelectric ground-state of $YMnO_3$ and allowed us to predict the evolution (at T = 0 K) of K_3, Γ_2^- and Γ_1^+ distortion amplitudes, spontaneous polarization and strain between metallic electrodes taking into account the quality of screening provided by the electrodes through an effective screening length parameter, λ_{eff}.

The amplitude of Γ_1^+ mode was strongly strain dependent, while the amplitudes of K_3 and Γ_2^- modes were little strain dependent under the mechanical boundary conditions (epitaxial and uniaxial strain between -3% and 3%) and electrical boundary conditions (open-circuit, short-circuit and imperfect screening). The distortion amplitudes and polarization for imperfect screening of depolarizing filed with the screening length $\lambda_{eff} = 0.25\,\text{Å}$ were always closer to perfect screening (short-circuit) than without screening of the depolarizing field (open-circuit) conditions. All K_3, Γ_2^- and Γ_1^+ distortions were proportionally more sensitive to compressive strain along both *a* and *c* directions. The K_3 and Γ_1^+ modes were slightly and significantly more sensitive to epitaxial than uniaxial strain, respectively. At the opposite, the Γ_2^- mode was little more sensitive to uniaxial than epitaxial strain. All distortions showed a linear and slightly quadratic behavior with epitaxial and uniaxial strain in the range from -3 % to +3 %, respectively. The little dependence on strain of K_3 and Γ_2^- modes didn't confirm the expectations to tune the ferroelectricity in hexagonal $YMnO_3$ as was successfully achieved in cubic perovskites.

The slightly stronger response to uniaxial strain of Γ_2^- mode was in agreement with a decrease of the amplitude Γ_2^- under open-circuit comparing to short-circuit conditions by a factor of 1.5 – 2.0 and 1.9 - 1.7 for epitaxial and uniaxial strain between -3 % and +3 %, respectively. In the following, the spontaneous polarization decreased by a factor of 10 - 13 and 12 - 11 for epitaxial and uniaxial strain, respectively. Although, a big decrease of Γ_2^- amplitude under open-circuit conditions (comparing to short-circuit) was observed, the ferroelectricity was not suppressed in thin films of $YMnO_3$. The film remained ferroelectric even under the open-circuit conditions.

As expected, in case of in-plane compression of hexagonal $YMnO_3$ structure, we observed an elongation along *c* direction and vice versa. The response of system was bigger to applied epitaxial than uniaxial strain.

Chapter 6

Structural and dynamical properties of experimentally grown $YMnO_3$ epitaxial thin films

The present chapter is devoted to the experimental growth, by liquid injection Metal Organic Chemical Vapor Deposition (MOCVD), and characterization of thin films of hexagonal $YMnO_3$. The epitaxial growth and structural properties of hexagonal $YMnO_3$ films on YSZ substrate are discussed. We report our room-temperature Raman spectra of films in comparison to single crystal discussed in the previous chapters of this manuscript.

6.1 Epitaxial growth on yttria-stabilized zirconia substrate

As presented in Chapter 1, $YMnO_3$ usually crystallizes in a stable hexagonal $P6_3cm$ phase, but can also be stabilized in a perovskite-type orthorhombic phase [67,68,69]. The growth of hexagonal $YMnO_3$ is therefore not straightforward since the use of usual perovskite substrates ($SrTiO_3$, $LaAlO_3$) promote the growth of the perovskite phase of $YMnO_3$ phase (by epitaxial

phase stabilization). The growth of hexagonal phase required to find an appropriate substrate. The choice was limited by the requirement of having a good crystalline match with hexagonal $YMnO_3$. In this work, we used the yttria-stabilized zirconia (YSZ) (111) substrate.

The crystal structure of YSZ is a cubic fluorite-type structure with the space group *Fm-3m* (225) (Figure 6.1). The lattice parameter is $a_{YSZ} = 5.12$ Å. The plane of the crystal surface used for the growth of hexagonal films is (111) finished by Zr (Y) atoms[5].

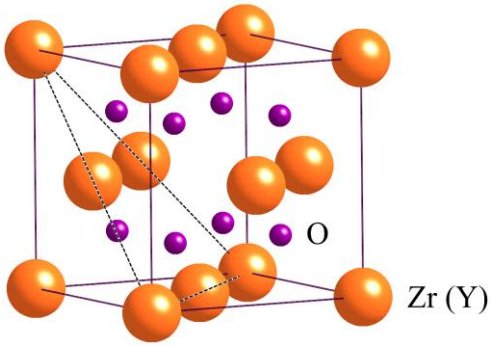

Figure 6.1 Crystal structure of YSZ. The dashed line shows the plane (111).

The atomic arrangement of the (111) plane of YSZ substrate matches very well the hexagonal structure of $YMnO_3$ (Figure 6.2) and allows an epitaxial growth with a good crystalline quality.

The correspondence between the lattice parameter a_{YSZ} of YSZ substrate and the distance of hexagonal atomic arrangement a_{hex} shown in Figure 6.2 is:

$$a_{hex} = \sqrt{\frac{3}{2}}\, a_{YSZ}. \qquad (6.1)$$

[5] The YSZ (111) substrates were provided by company CrysTec [70] through the collaboration in European Project MaCoMuFi.

Then, the epitaxial strain η_s imposed by the YSZ (111) substrate on hexagonal $YMnO_3$ film is given as follows:

$$\eta_s = \frac{a_{hex} - a_{YMO}}{a_{YMO}}. \tag{6.2}$$

In compounds exhibiting different phases, report of epitaxial strain is often misleading in the literature since its value depends on the phase taken as reference.

On one hand, the evaluated epitaxial strain $\eta_{S\text{-}FE}$ imposed by YSZ (111) substrate on the *ferroelectric* phase of $YMnO_3$ (space group $P6_3cm$) is +2.1 % considering the experimental lattice parameter $a_{YMO}^{FE} = 6.14$ Å of $YMnO_3$ [44] (for other lattice parameters see Table 3.2).

On the other hand, the epitaxial strain $\eta_{S\text{-}PE}$ imposed by YSZ (111) substrate on the *paraelectric* phase of $YMnO_3$ is +0.74 % using the experimental lattice parameter $a_{YMO}^{PE} = 3.61$ Å of $YMnO_3$ [43] (for other lattice parameters see Table 3.4).

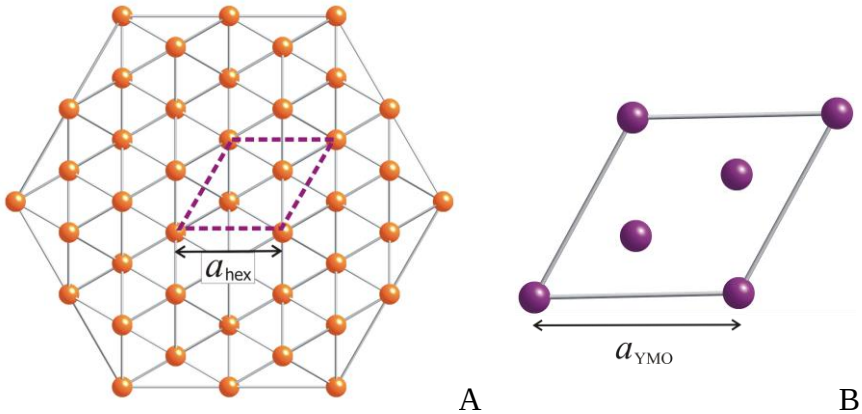

Figure 6.2 Structural relation between YSZ and hexagonal $YMnO_3$ (space group: $P6_3cm$). Equivalent hexagonal atomic arrangement (violet dashed line) in (111) plane of Zr (Y) atoms (orange balls) of YSZ; a_{hex} is the distance between two atoms connected by dashed line (A). The plane of oxygen atoms (violet balls) of $YMnO_3$; a_{YMO} is the lattice parameter defined by the distance between two oxygen atoms (B).

Since our first-principles model presented in Chapter 5 is built around the paraelectric reference structure of $YMnO_3$, in further discussion we will often consider the epitaxial strain $\eta_{S\text{-}PE}$ between YSZ (111) substrate and paraelectric phase of $YMnO_3$.

6.2 Growth parameters

We have grown the hexagonal $YMnO_3$ epitaxial thin films using liquid injection MOCVD. One of the challenges in the chemical vapour deposition of complex oxides is the control of the film composition as the molar ratio of precursors in the liquid solution is different than that in the film. The different precursors have different decomposition yields. The elements have different behaviours as far as diffusion and incorporation in the lattice is concerned. A calibration is needed to find out the appropriate ratio.

The main growth parameters that we optimized are the growth temperature (between 825 and 900°) and the molar ration of Y/Mn in the liquid solution (between 0.8 and 1.2). The other growth parameters concerning the gas flows, the evaporation temperature and the Ar and O_2 partial pressures were already optimized by A. Bosak [70] and are listed in Table 2.1 in Chapter 2.

6.3 Structural characterization

We used the X-ray diffraction technique as a primary tool for the optimization of the growth conditions and for the characterization of the crystalline structure of $YMnO_3$ thin films.

Our YMO_3 thin films are hexagonal, single phase and (001) textured. The optimized growth temperature is 850°C and the molar ratio of Y/Mn in liquid solution is $n_Y / n_{Mn} = 0.9$.

As an example, Figure 6.3 shows a X-ray diffraction $\theta / 2\theta$ scan of a YMO_3 film 32 nm thick grown on YSZ (111) substrate, where only peaks of $YMnO_3$ (001) and YSZ (111)

families are observed. The rocking curve scan around the 004 reflection indicates a narrow *c* axis distribution of 0.07° shown in Figure 6.4. The same behavior is observed in other films.

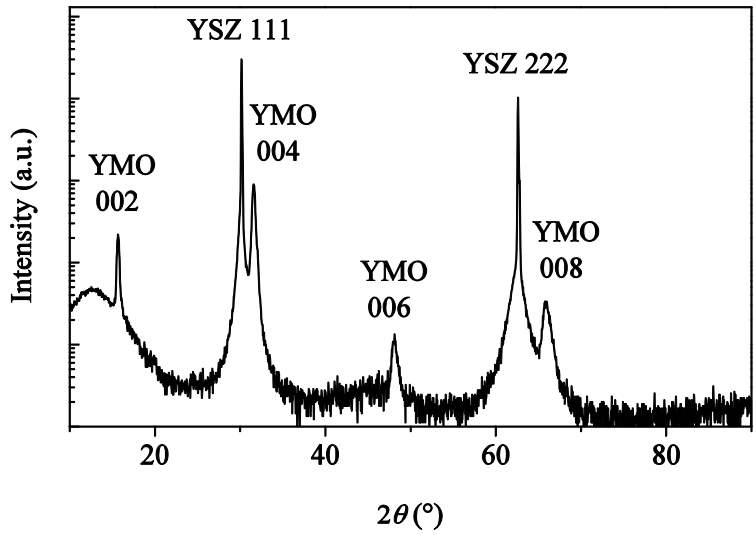

Figure 6.3 X-ray diffraction $\theta/2\theta$ scan of hexagonal $YMnO_3$ (YMO) film on YSZ (111) at 850°C and $n_Y / n_{Mn} = 0.9$. The film thickness is 32 nm.

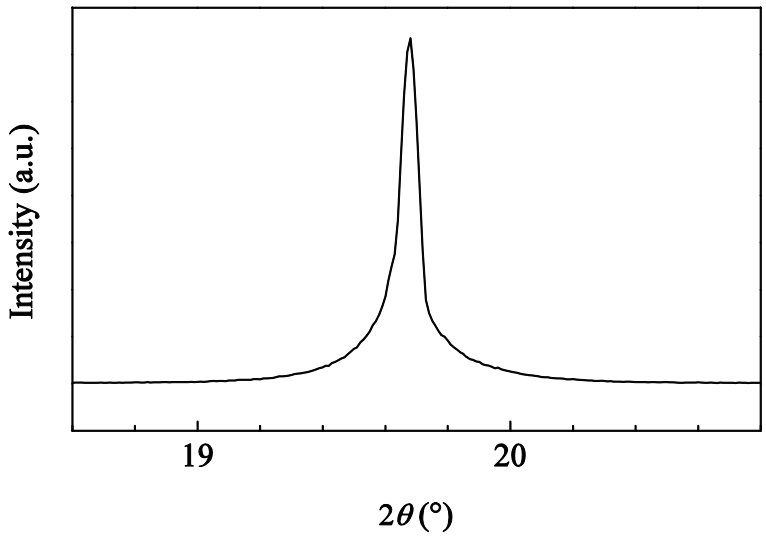

Figure 6.4 X-ray diffraction rocking curve of 004 reflection of hexagonal $YMnO_3$ film of 32 nm thick grown on YSZ (111) at 850°C and $n_Y / n_{Mn} = 0.9$.

The X-ray diffraction ϕ-scans were measured by I. Gélard [71] to determine the epitaxial relationship between the substrate and the film, which is given as follows $YMnO_3(001)_{hex}$ // YSZ(111) and $YMnO_3 <1\bar{1}0>_{hex}$ // YSZ $<1\bar{1}0>$.

As discussed in Section 6.1, thin films of $YMnO_3$ fully strained on YSZ (111) substrate are in-plane stretched by 2.1 % and are expected to exhibit a smaller out-of plane *c*-lattice parameter. This situation is expected for ultrathin films; as its thickness increases, the film will progressively relax and its *c*-parameter evolves to its unstrained value. Figure 6.5 shows the dependence of *c*-lattice parameter with film thickness for hexagonal $YMnO_3$.

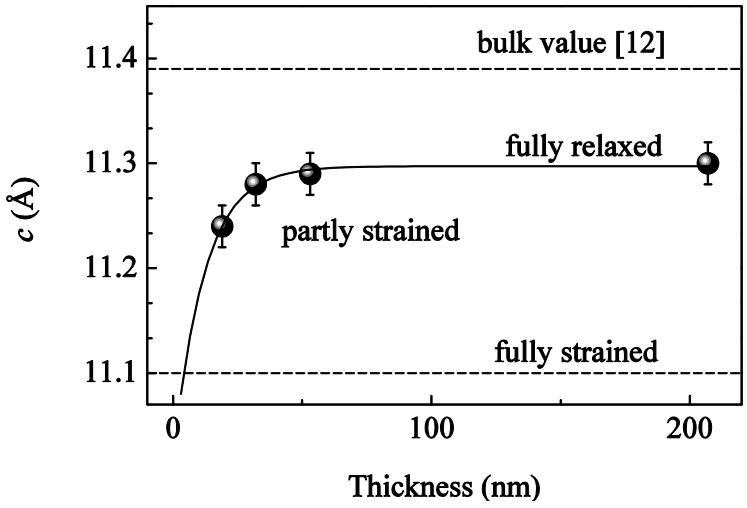

Figure 6.5 Lattice parameter *c* dependence on thickness of hexagonal $YMnO_3$ thin films. The lattice parameter was calculated from 008 reflection of films grown on YSZ (111) at 850°C and $n_Y / n_{Mn} = 0.9$.

Consistently with our expectations, we observe that the *c* parameter smoothly evolves with the film thickness, saturating to the value of 11.31 Å, for films thicker than 50 nm. Although, with a lattice parameter smaller than the one measured on single crystals (between 11.40 and 11.44 Å, see Table 3.2 in Chapter 3) those films can be considered as fully relaxed. A possible deviation from the stoichiometric Y/Mn ratio of 1 could explain the smaller lattice parameter of the relaxed films compared to the bulk [72]. We observe that the *c* parameter indeed decreases with decreasing film thickness.

Using our model (see Figure 5.3 in Chapter 5), we predict that the epitaxial strain imposed by the YSZ substrate, reduces the lattice parameter of fully strained films by 1.8 % compared to fully relaxed films. This translates *c* here into a lattice parameter of 11.11 Å (dashed line in Figure 6.5). This clarifies that our films at 19 – 53 nm are already partly relaxed. Assuming a smooth evolution, it also suggests that fully strained films are only observed below 4.5 nm; above this value the films are partly relaxed.

6.4 Room-temperature Raman spectra

As discussed in Chapter 4 (see Table 4.1), hexagonal $YMnO_3$ in space group $P6_3cm$ has 38 Raman-active phonon modes. The majority of these modes has already been observed and identified (see Section 4.2.4 in Chapter 4). At the opposite, to the best of our knowledge, no experimental Raman data was previously reported on $YMnO_3$ thin films. Therefore, we were interested to measure the Raman spectra of thin films and compare to those of a single crystal of $YMnO_3$.

Figure 6.6 shows the polarized room-temperature Raman spectrum of $YMnO_3$ thin film of 32 nm thick grown on YSZ (111) substrate. The direction of incident and scattered light is along *c*-axis. The incident and scattered light were polarized in *ab* plane.

As we can see, we observed two Raman peaks at 617 cm^{-1} and 686 cm^{-1} frequencies. The first peak corresponds to the phonon coming from the YSZ substrate and the second is a A_1(LO) phonon mode of $YMnO_3$.

The frequency of A_1(LO) mode measured in 32 nm thick thin film of $YMnO_3$ at 686 cm^{-1} is within the experience error and equal to the frequency of the A_1(LO) mode measured in a single crystal at 684 cm^{-1} (see Figure 4.4 in Chapter 4). It corresponds to our $A_1(LO_8)$ mode calculated at 691 cm^{-1} (LSDA+*U*) and 707 cm^{-1} (B1-WC) (see Table 4.2 in Chapter 4). We notice that the A_1(LO) mode has no substantial LO-TO splitting so that what is measured is also the $A_1(TO_9)$ mode (see Table 4.2 in Chapter 4). In further discussion, we will often

consider the A_1(LO) mode measured at 686 cm^{-1} in thin film as A_1(TO) (or Γ_1^+ used in our model).

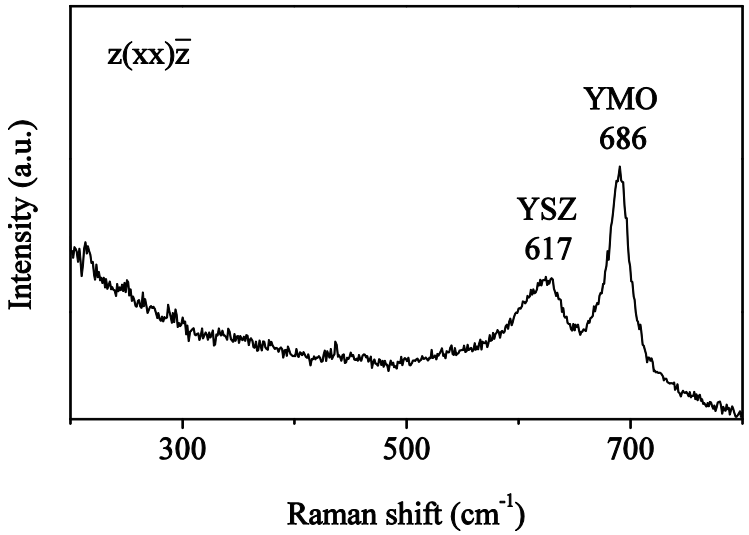

Figure 6.6 Raman spectrum of $YMnO_3$ thin film on YSZ (111) in $z(xx)\bar{z}$ configuration at room temperature. Film of thickness 32nm grown at 850°C with $n_Y / n_{Mn} = 0.9$.

In Figure 6.7, we observed a slight evolution of the Raman peak position with the film thickness. Although, this frequency change is within the experimental error, it might be questioned whether the following of this Raman peak position might provide indication about the degree of relaxation of the film.

Interestingly, the A_1(TO) mode at 686 cm^{-1} of ferroelectric *P6₃cm* phase corresponds to the Γ_1^+ (A_{1g}) mode at 712 cm^{-1} of paraelectric *P6₃mmc* phase of $YMnO_3$. The overlap between these two modes is equal to 0.995[6]. This Γ_1^+ mode is associated to opposite motion of apical oxygen atoms in oxygen octahedral along *z*-axis as illustrated in Figure 5.1 and is included in our first-principles model discussed in Chapter 5. We observed there that the amplitude of Γ_1^+ mode is strongly strain dependent so that we can expect to measure a significant Raman shift

[6] Contrary to the paraelectric K_3 and Γ_2^- modes (see discussion in Section 4.4 in Chapter 4), the correspondence of a paraelectric Γ_1^+ mode at 712 cm^{-1} with a ferroelectric A_1(TO) mode at 686 cm^{-1} is one to one.[6]

with increasing film thickness reinforcing the hope that the Raman spectroscopy could be a useful indirect tool to evaluate the strain state of thin films.

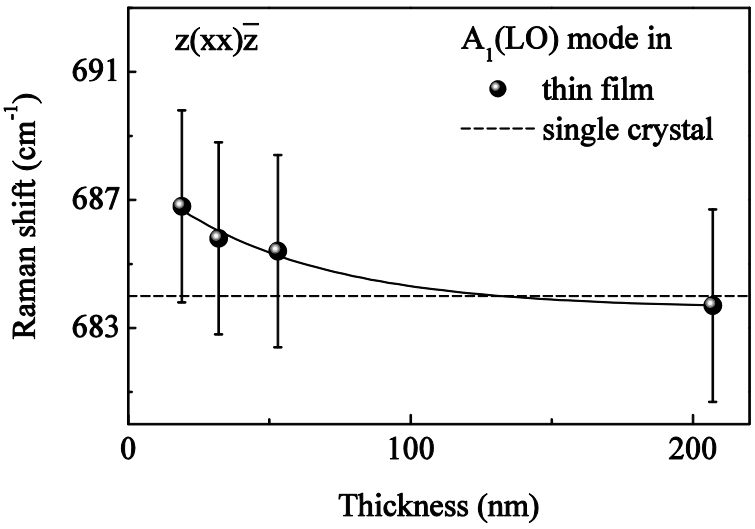

Figure 6.7 Evolution of A_1(LO) mode in room-temperature Raman measurements (Raman shift in cm^{-1}) on thickness of hexagonal $YMnO_3$ thin films in $z(xx)\bar{z}$ configuration on YSZ (111) at 850°C and $n_Y / n_{Mn} = 0.9$. Dashed line corresponds to a value of single crystal (obtained within this work, Figure 4.4 in Chapter 4). The line is for visual guidance.

In order to quantify the strain effect and supplement with the theoretical estimations our experimental Raman results shown in Figure 6.7, we used our model to estimate the frequency shift of A_1(TO) mode in a fully strained film.

Our model provides the energy landscape in terms of relevant degrees of freedom. In order to determine the frequency of Γ_1^+ mode in a fully strained film, we computed the curvature of model energy (Eq. 5.5 in Chapter 5) along Γ_1^+ direction:

$$E^{(2)} = \frac{\partial^2 E}{\partial Q_{\Gamma_1^+}{}^2} = 0.34190 + 0.03312 \cdot Q_{\Gamma_1^+} - 0.01092 \cdot Q_{\Gamma_1^+}^2 + 0.00526 \cdot Q_{\Gamma_2^-}^2 \\ -0.60350 \cdot \eta_a + 2.32756 \cdot \eta_a^2 - 1.42872 \cdot \eta_c. \qquad (6.3)$$

This curvature is directly proportional to ω^2 and we can estimate it from different values of the parameters. Table 6.1 lists the amplitudes of K_3, Γ_2^- and Γ_1^+ modes and the values of in-plane η_a and out-of-plane η_c strain in ferroelectric *P6$_3$cm* ground state of $YMnO_3$ used to compute the energy curvature (Eq. 6.3) and determine the frequency of Γ_1^+ mode for fully strained films of $YMnO_3$. The first line corresponds to fully relaxed configuration in our first-principles model. The strain percentage indicates the strain values with respect to the paraelectric phase of $YMnO_3$. The second line indicates the mode amplitudes and the value of out-of plane strain for a fully strained film grown on YSZ (111) substrate (see Section 6.1).

	Q_{K_3}	$Q_{\Gamma_2^-}$	$Q_{\Gamma_1^+}$	η_a (%)	η_c (%)	$E^{(2)}$(eV)	ω (cm^{-1})
Relaxed	0.974	1.007	0.999	-1.31	+2.23	0.3455	683
Fully strained (YSZ)	0.89	0.90	0.23	+0.74	+0.31	0.3443	682

Table 6.1 Amplitudes of K_3, Γ_2^- and Γ_1^+ modes (in fractional units) and in-plane η_a and out-of-plane η_c strain in ferroelectric *P6$_3$cm* ground state of $YMnO_3$ for (a) the relaxed structure respect to paraelectric structure (fully relaxed configuration in our model, see discussion and Table 5.5 in Chapter 5) and (b) for fully strained thin film of $YMnO_3$ grown on YSZ (111) substrate.

The computed frequency of Γ_1^+ mode in a fully strained film is 682 cm^{-1}. Contrary to our expectations, the strain effect on Γ_1^+ mode frequency is very small and of the order of 1 cm^{-1} (considering that the measured frequency of Γ_1^+ mode in a relaxed film is 683 cm^{-1}). We note that, computing the curvature of model energy (Eq. 6.3) when considering just the first three terms of Γ_1^+ mode and neglecting the contribution of other terms, the effect is bigger and of the order of 14 cm^{-1} (669 cm^{-1}). This means that the Γ_1^+ mode is intrinsically sensitive to strain (as the amplitude reduces with strain, see Table 6.1) and it shifts the minimum to higher energy, but other anharmonic contributions as phonon-phonon coupling and phonon-strain

coupling act in order to compensate this evolution. This analysis concludes that the weak evolution shown in Figure 6.7 is not significant and is in agreement with the modeling. In addition, from our calculations, the frequency of Γ_1^+ mode should increase with increasing film thickness contrary to what suggests Figure 6.7.

It is unfortunate, that we observed just one intense Raman-active mode $A_1(LO)$ at a frequency of 686 cm^{-1} in $YMnO_3$ thin films at room temperature. The background coming from the YSZ substrate (Figure 6.8) is too high and thus covered the other peaks of $YMnO_3$. We obtained the same results for the other Raman measurement configurations (see Table 4.5 in Chapter 5). A posteriori, Raman spectroscopy does not appear as a useful tool to get information on the strain in such films.

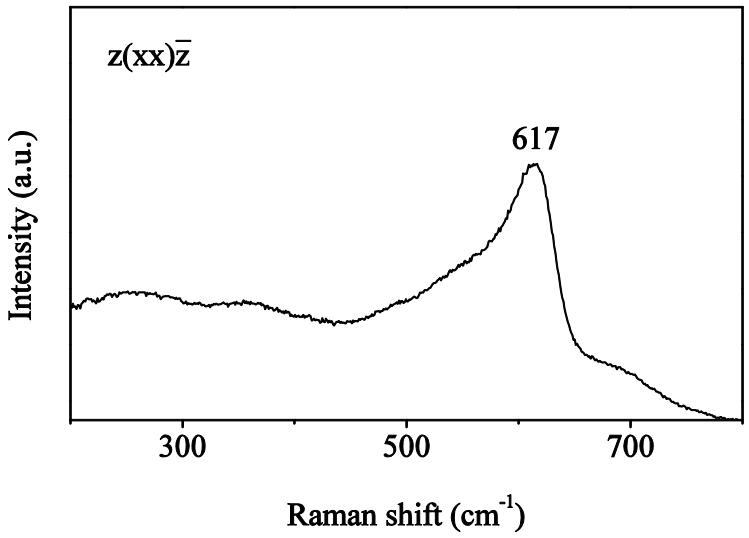

Figure 6.8 Raman spectrum of YSZ (111) in $z(xx)\bar{z}$ configuration at room temperature.

6.5 Conclusions

The epitaxial growth of hexagonal $YMnO_3$ with *c*-axis out-of-plane has been achieved on YSZ (111) substrate by liquid injection MOCVD. The optimised growth temperature was

850°C. The molar ration of Y/Mn in the liquid solution was 0.9. Films were grown in the thickness range of 19 – 207 nm.

The structural characterization showed that the thin films of $YMnO_3$ were of a good crystalline quality. The epitaxial relationship was $YMnO_3(001)_{hex}$ // YSZ(111) and $YMnO_3 <1\bar{1}0>_{hex}$ // YSZ $<1\bar{1}0>$. The bi-axial tensile strain led to an elongation of the *c*-lattice parameter. The *c* parameter increased with increasing film thickness and reached a constant value corresponding to the relaxed lattice parameter. This result was consistent with the modelling, although the *c*-lattice parameter of relaxed thin film was smaller than the lattice parameters of single crystals reported in literature, which could be related to a deviation from 1:1 cationic stoichiometry. From our first-principles model results, we estimated that the films in a range of thickness of 19 – 53 nm with *c* value between 11.25 – 11.30 Å were already partly relaxed. From first-principle model, we predicted a *c* value of 11.11 Å for fully strained thin film of $YMnO_3$ and estimated that the films started relaxing at 4.5 nm.

Then, we performed room-temperature Raman measurements expecting that the Raman spectroscopy could be a useful indirect tool to study strain state in thin films of $YMnO_3$ discussed in Chapter 5. We observed the phonon mode measured at a frequency of 686 cm^{-1}, which we assigned to the Γ_1^+ mode. From our first-principles model, this mode was predicted to have a weak frequency dependence on epitaxial strain. This is in good agreement with our experimental Raman measurements that showed only a weak evolution, within the experimental accuracy.

In addition, we expected to compare the phonon frequencies observed in thin films with the frequencies measured in a single crystal $YMnO_3$ within this work, but the YSZ substrate was too high Raman-active. We measured one phonon mode at 686 cm^{-1}, which is in a good agreement with that measured in a single crystal and with that calculated from first-principles values. We couldn't observe other Raman-active phonons at room temperature.

Conclusions / Perspectives

In this thesis, after presenting the general theoretical overview in Chapter 1 and our used theoretical and experimental techniques followed by technical details in Chapter 2, we reported a diverse study of yttrium manganite representing the class of less known hexagonal in comparison to usual widely studied cubic ABO_3 compounds. We achieved to combine theoretical and experimental approaches. We explored yttrium manganite in single crystal and thin film forms. Both ground-state ferroelectric and high-temperature paraelectric phases of yttrium manganite were under investigation. Our main results can be summarized as follows.

First, in Chapter 3, we reported our optimized structures of ferroelectric and paraelectric phases of hexagonal $YMnO_3$ in bulk from first principles. The LSDA+*U* and B1-WC functionals and our limitation to collinear magnetism provided the good estimates of lattice parameters, atomic positions (except the position of Mn atom in ferroelectric phase), band gap and local magnetic moment of Mn atoms for both phases comparing to other theoretical and experimental data. The attempts to go beyond collinear magnetism and to treat more properly the triangular arrangement of Mn spins could be important to achieve a better description of the Mn position.

Next, once we had the optimized structures, we calculated the zone-center phonon frequencies of ferroelectric and paraelectric phases of hexagonal $YMnO_3$ in bulk, as reported and discussed in Chapter 4. From our calculations, we refined the assignment previously based on semi-empirical calculations of experimentally observed phonon modes available in the literature. We supplemented our theoretical study with our own measured Raman spectra measurements at room temperature of ferroelectric $YMnO_3$ in bulk. Although the single crystal of $YMnO_3$ was miscut, our calculated angular dependence of phonon frequencies was

weak and we concluded that our measured frequencies were good estimate of TO and LO modes and in very good agreement with previous experimental data available in the literature. The experimentally observed new E_2 mode at a frequency of 247 cm^{-1} and proposed reassignment of experimentally measured modes with respect to our first-principles values increased the number of known Raman-active phonon modes from 28 to 32 out of 38 in ferroelectric phase of $YMnO_3$. Our first-principles phonon calculations confirmed that the $YMnO_3$ is indeed an improper ferroelectric.

Then, we extended our study from bulk to thin films of hexagonal and improper ferroelectric $YMnO_3$ reported in Chapter 5. In order to study whether the ferroelectricity in hexagonal as in cubic ABO_3 compounds is tunable with strain engineering, we developed a first-principles model based on K_3, Γ_2^-, Γ_1^+ and strain degrees of freedom and we treated explicitly the role of the mechanical and electrical boundary conditions in thin film epitaxially grown on a substrate between two metallic electrodes. We showed that the Γ_1^+ had to be included into the model to properly account for the strain relaxation and consequently this mode was observed to be strongly strain dependent. In contrary to our expectations, the hexagonal ABO_3 compounds didn't show high capabilities to tune ferroelectricity via strain engineering as the polar Γ_2^- mode and the unstable K_3 showed a weak dependence on strain. However, the hexagonal ABO_3 compounds remained highly interesting for the applications as the ferroelectricity was not suppressed even in ultrathin improper ferroelectric films under the open circuit conditions.

Last, we realized the epitaxial growth of hexagonal $YMnO_3$ thin films on YSZ substrate by MOCVD and we studied the structure of the films and its strain dependence using X-Ray diffraction and Raman spectroscopy as described in Chapter 6. In agreement with our first-principles model for thin films of $YMnO_3$, X-ray diffraction results showed the relaxation of *c*-lattice parameter with increasing film thickness to bulk value. In Raman spectra measured at room temperature, we observed a slight frequency dependence approaching the bulk value of the ferroelectric A_1 symmetry mode measured at a frequency of 686 cm^{-1} with increasing film thickness. As the recorded ferroelectric A_1 mode was one to one in correspondence to paraelectric Γ_1^+ mode at a frequency of 712 cm^{-1} included in our model, we determined that the observed slight A_1 phonon frequency dependence on film thickness was not significant.

Concluding, the perspectives of the present work, related to our constructed first-principles model and the experimental approach to study thin films of $YMnO_3$, are the following.

First, our first-principles model opens the possibility to study the role of mechanical and electrical boundary conditions in thin films of $YMnO_3$ under finite bias. Next, it would be interesting to compare the behaviour of proper to that of improper ferroelectrics, for instance, compare the behaviour of $BaTiO_3$ to the behaviour of hexagonal $YMnO_3$. Going further, since the hexagonal $YMnO_3$ is a magnetoelectric material, the model could be extended to treat the coupling with magnetism.

From the experimental point of view, first, it would be interesting to study and understand better the existence of formal polarization and its screening mechanism in the paraelectric centrosymmetric phase of $YMnO_3$. Next, the realization of the epitaxial growth of hexagonal $YMnO_3$ films on less Raman-active substrates could let observe and measure more phonon modes and thus compare better the dynamical properties in film to those in bulk $YMnO_3$.

Appendix A

Overlaps of TO phonon modes

This appendix contains total overlaps defined and discussed in Chapter 4 section 4.2.3.2.

TO, 0°	LO-TO, 20°	ω_{TO} (cm^{-1})	$\omega_{LO\text{-}TO}$ (cm^{-1})	overlap A_1(TO)	overlap E_1(TO)
A_1 (TO_1)	LO-TO (1)	170.18	170.33	0.9996	0.0283
A_1 (TO_2)	LO-TO (2)	252.23	252.76	0.9913	0.1314
A_1 (TO_3)	LO-TO (3)	272.39	272.40	0.9967	0.0811
A_1 (TO_4)	LO-TO (4)	312.57	312.03	0.9723	0.2337
A_1 (TO_5)	LO-TO (5)	427.58	427.58	0.9999	0.0127
A_1 (TO_6)	LO-TO (6)	460.08	459.96	0.9684	0.2494
A_1 (TO_7)	LO-TO (7)	497.92	481.31	0.7579	0.6524
A_1 (TO_8)	LO-TO (8)	593.21	530.34	0.7646	0.6445
A_1 (TO_9)	LO-TO (9)	691.23	691.24	1.0000	0.0025

Table A.1 Total overlaps of TO phonon modes of A_1 symmetry with modes at the angle of 20°.

TO mode, 90°	LO-TO mode, 70°	ω_{TO} (cm^{-1})	$\omega_{LO\text{-}TO}$ (cm^{-1})	overlap A_1(TO)	overlap E_1(TO)
E_1 (TO_1)	LO-TO (1)	171.28	171.28	0.0012	1.0000
E_1 (TO_2)	LO-TO (2)	183.03	183.03	0.0043	1.0000
E_1 (TO_3)	LO-TO (3)	211.13	211.56	0.0591	0.9983
E_1 (TO_4)	LO-TO (4)	245.23	245.23	0.0111	0.9999
E_1 (TO_5)	LO-TO (5)	273.99	282.94	0.6098	0.7926
E_1 (TO_6)	LO-TO (6)	301.71	303.91	0.4218	0.9067
E_1 (TO_7)	LO-TO (7)	366.72	373.05	0.25626	0.96661
E_1 (TO_8)	LO-TO (8)	379.22	380.17	0.1338	0.9910
E_1 (TO_9)	LO-TO (9)	402.69	403.08	0.0595	0.9982
E_1 (TO_{10})	LO-TO (10)	418.69	419.52	0.0876	0.9962
E_1 (TO_{11})	LO-TO (11)	459.44	459.44	0.0431	0.9991
E_1 (TO_{12})	LO-TO (12)	488.85	488.86	0.0181	0.9998
E_1 (TO_{13})	LO-TO (13)	622.20	622.17	0.0378	0.9993
E_1 (TO_{14})	LO-TO (14)	644.10	644.09	0.0088	1.0000

Table A.2 Total overlaps of TO phonon modes of E_1 symmetry with modes at the angle of 70°.

Appendix B

Overlaps of A_1(TO) and K_3, Γ_2^- and Γ_1^+ modes

This appendix contains the overlaps defined and discussed in Chapter 4 section 4.4 and Chapter 6 section 6.4.

mode	frequency (cm^{-1})	overlap K_3 ($153i$ cm^{-1})	overlap Γ_2^- (85 cm^{-1})	overlap Γ_1^+ (712 cm^{-1})
A_1 (TO_1)	170	-0.731	0.187	-0.011
A_1 (TO_2)	252	0.037	-0.616	0.034
A_1 (TO_3)	272	0.144	-0.303	0.067
A_1 (TO_4)	313	-0.217	-0.649	-0.055
A_1 (TO_5)	428	-0.191	0.157	0.006
A_1 (TO_6)	460	-0.458	-0.200	-0.001
A_1 (TO_7)	498	0.006	0.091	0.017
A_1 (TO_8)	593	-0.010	0.010	0.023
A_1 (TO_9)	691	0.030	-0.005	-0.995

Table B.1 Overlaps between the eigendisplacements of ferroelectric A_1(TO) modes and paraelectric K_3, Γ_2^- and Γ_1^+ modes.

Appendix C
Coefficients of first-principles model for epitaxial $YMnO_3$ thin films

This appendix reports the explicit description of how the polynomial coefficients of the first-principles model for epitaxial $YMnO_3$ thin films presented in Chapter 5 were determined. The coefficients are the fitting parameters of the first-principles data performed for an optimized LSDA+*U* triple paraelectric phase reported in Chapter 3. All curves were fitted with the 4^{th} order polynomial function in amplitude range of [-1, 1] with step of 0.25 in fractional units. We analysed the mode coupling with strain in the range of [-3 %, 3 %] with step of 1%. The self-consistent cycles were converged up to tolerances of 10^{-9} Ha / Bohr on the difference of total energy. We considered that the coefficients were negligible when the change of total energy was of the order of the calculations error of 1 meV. The values of coefficients were rounded till the last significant number. We used the colors to sort the associated polynomial terms.

C.1 Notations

This section contains the description of notations used in the energy expansion Eq. C.1.

K_3	individual mode K_3
Γ_2^-	individual mode Γ_2^-
Γ_1^+	individual mode Γ_1^+
Q_{K_3}	distortion amplitude of K_3 mode in fractional units
$Q_{\Gamma_2^-}$	distortion amplitude of Γ_2^- mode in fractional units
$Q_{\Gamma_1^+}$	distortion amplitude of Γ_1^+ mode in fractional units
$Q_{K_3}Q_{\Gamma_2^-}$	mode coupling : K_3 and Γ_2^-
$Q_{K_3}Q_{\Gamma_1^+}$	mode coupling : K_3 and Γ_1^+
$Q_{\Gamma_2^-}Q_{\Gamma_1^+}$	mode coupling : Γ_2^- and Γ_1^+
η_a	in-plane strain
η_c	out-of plane strain
$\eta_{a,c}Q_{K_3}$	strain individual mode coupling : strain and K_3
$\eta_{a,c}Q_{\Gamma_2^-}$	strain individual mode coupling : strain and Γ_2^-
$\eta_{a,c}Q_{\Gamma_1^+}$	strain individual mode coupling : strain and Γ_1^+
$\eta_{a,c}Q_{K_3}Q_{\Gamma_2^-}$	strain mode coupling : strain and K_3, Γ_2^-
$\eta_{a,c}Q_{K_3}Q_{\Gamma_1^+}$	strain mode coupling : strain and K_3, Γ_1^+
$\eta_{a,c}Q_{\Gamma_2^-}Q_{\Gamma_1^+}$	strain mode coupling : strain and Γ_2^-, Γ_1^+

$\boxed{Q^2_{K_3} \cdot Q^2_{\Gamma_1^+}}$ in rectangle: not included into the model

C.2 List of coefficients

This section contains the notations of corresponding polynomial coefficients of the energy expansion Eq. C.1. A summary of numerical values is given in Section C.5.

$Q^2_{K_3}$, $Q^4_{K_3}$	α_{20}, α_{40}
$Q^2_{\Gamma_2^-}$, $Q^4_{\Gamma_2^-}$	β_{20}, β_{40}
$Q_{\Gamma_1^+}$, $Q^2_{\Gamma_1^+}$, $Q^3_{\Gamma_1^+}$, $Q^4_{\Gamma_1^+}$	γ_{10}, γ_{20}, γ_{30}, γ_{40}
$Q^3_{K_3}Q_{\Gamma_2^-}$, $Q^2_{K_3}Q^2_{\Gamma_2^-}$	κ_{310}, κ_{220}
$Q^2_{K_3}Q_{\Gamma_1^+}$, $Q^2_{K_3}Q^2_{\Gamma_1^+}$	τ_{210}, τ_{220}
$Q^2_{\Gamma_2^-}Q_{\Gamma_1^+}$, $Q^2_{\Gamma_2^-}Q^2_{\Gamma_1^+}$	μ_{210}, μ_{220}
η_a^2, η_a^3	ρ_{a2}, ρ_{a3}
η_c^2, η_c^3	ρ_{c2}, ρ_{c3}
$\eta_a\eta_c$, $\eta_a^2\eta_c$, $\eta_a\eta_c^2$	ρ_{ac}, ρ_{ac21}, ρ_{ac12}
$\eta_a Q^2_{K_3}$, $\eta_a^2 Q^2_{K_3}$, $\eta_a Q^4_{K_3}$	α_{21}, α_{212}, α_{41}
$\eta_c Q^2_{K_3}$, $\eta_c^2 Q^2_{K_3}$, $\eta_c Q^4_{K_3}$	α_{23}, α_{232}, α_{43}
$\eta_a\eta_c Q^2_{K_3}$, $\eta_a\eta_c Q^4_{K_3}$	α_{24}, α_{44}

$\eta_a Q^2_{\Gamma_2^-}$, $\eta_a Q^4_{\Gamma_2^-}$	β_{21} , β_{41}
$\eta_c Q^2_{\Gamma_2^-}$, $\eta_c Q^4_{\Gamma_2^-}$	β_{23} , β_{43}
$\eta_a Q_{\Gamma_1^+}$, $\eta_a^2 Q_{\Gamma_1^+}$, $\eta_a Q^2_{\Gamma_1^+}$, $\eta_a^2 Q^2_{\Gamma_1^+}$, $\eta_a Q^3_{\Gamma_1^+}$, $\eta_a Q^4_{\Gamma_1^+}$	γ_{11} , γ_{112} , γ_{21} , γ_{212} , γ_{31} , γ_{41}
$\eta_c Q_{\Gamma_1^+}$, $\eta_c^2 Q_{\Gamma_1^+}$, $\eta_c Q^2_{\Gamma_1^+}$, $\eta_c Q^3_{\Gamma_1^+}$, $\eta_c Q^4_{\Gamma_1^+}$	γ_{13} , γ_{132} , γ_{23} , γ_{33} , γ_{43}
$\eta_a Q^3_{K_3} Q_{\Gamma_2^-}$, $\eta_a Q^2_{K_3} Q^2_{\Gamma_2^-}$	κ_{311} , κ_{221}
$\eta_c Q^3_{K_3} Q_{\Gamma_2^-}$, $\eta_c Q^2_{K_3} Q^2_{\Gamma_2^-}$	κ_{313} , κ_{223}
$\eta_a Q^2_{K_3} Q_{\Gamma_1^+}$, $\eta_a^2 Q^2_{K_3} Q_{\Gamma_1^+}$, $\eta_a Q^2_{K_3} Q^2_{\Gamma_1^+}$	τ_{211} , τ_{2112} , τ_{221}
$\eta_c Q^2_{K_3} Q_{\Gamma_1^+}$, $\eta_c Q^2_{K_3} Q^2_{\Gamma_1^+}$	τ_{213} , τ_{223}
$\eta_a Q^2_{\Gamma_2^-} Q_{\Gamma_1^+}$, $\eta_a Q^2_{\Gamma_2^-} Q^2_{\Gamma_1^+}$	μ_{211} , μ_{221}
$\eta_c Q^2_{\Gamma_2^-} Q_{\Gamma_1^+}$, $\eta_c Q^2_{\Gamma_2^-} Q^2_{\Gamma_1^+}$	μ_{213} , μ_{223}

C.3 Associated coefficients

This section groups and lists the general notations of associated coefficients defined in previous Section C.2.

$(\eta_{a,c}) Q^2_{K_3}$	$\alpha_2\ \eta_a, \eta_c\ = \alpha_{20} + \alpha_{21} \cdot \eta_a + \alpha_{212} \cdot \eta_a^2 + \alpha_{23} \cdot \eta_c + \alpha_{232} \cdot \eta_c^2 + \alpha_{24} \cdot \eta_a \cdot \eta_c$
$(\eta_{a,c}) Q^4_{K_3}$	$\alpha_4\ \eta_a, \eta_c\ = \alpha_{40} + \alpha_{41} \cdot \eta_a + \alpha_{43} \cdot \eta_c + \alpha_{44} \cdot \eta_a \cdot \eta_c$

$(\eta_{a,c})Q^2_{\Gamma_2^-}$ $\beta_2\ \eta_a,\eta_c\ = \beta_{20} + \beta_{21}\cdot\eta_a + \beta_{23}\cdot\eta_c$

$(\eta_{a,c})Q^4_{\Gamma_2^-}$ $\beta_4\ \eta_a,\eta_c\ = \beta_{40} + \beta_{41}\cdot\eta_a + \beta_{43}\cdot\eta_c$

$(\eta_{a,c})Q_{\Gamma_1^+}$ $\gamma_1\ \eta_a,\eta_c\ = \gamma_{10} + \gamma_{11}\cdot\eta_a + \gamma_{112}\cdot\eta_a^2 + \gamma_{13}\cdot\eta_c + \gamma_{132}\cdot\eta_c^2$

$(\eta_{a,c})Q^2_{\Gamma_1^+}$ $\gamma_2\ \eta_a,\eta_c\ = \gamma_{20} + \gamma_{21}\cdot\eta_a + \gamma_{212}\cdot\eta_a^2 + \gamma_{23}\cdot\eta_c$

$(\eta_{a,c})Q^3_{\Gamma_1^+}$ $\gamma_3\ \eta_a,\eta_c\ = \gamma_{30} + \gamma_{31}\cdot\eta_a + \gamma_{33}\cdot\eta_c,$

$(\eta_{a,c})Q^4_{\Gamma_1^+}$ $\gamma_4\ \eta_a,\eta_c\ = \gamma_{40} + \gamma_{41}\cdot\eta_a + \gamma_{43}\cdot\eta_c.$

$(\eta_{a,c})Q^3_{K_3}Q_{\Gamma_2^-}$ $\kappa_{31}\ \eta_a,\eta_c\ = \kappa_{310} + \kappa_{311}\cdot\eta_a + \kappa_{313}\cdot\eta_c$

$(\eta_{a,c})Q^2_{K_3}Q^2_{\Gamma_2^-}$ $\kappa_{22}\ \eta_a,\eta_c\ = \kappa_{220} + \kappa_{221}\cdot\eta_a + \kappa_{223}\cdot\eta_c$

$(\eta_{a,c})Q^2_{K_3}Q_{\Gamma_1^+}$ $\tau_{21}\ \eta_a,\eta_c\ = \tau_{210} + \tau_{211}\cdot\eta_a + \tau_{2112}\cdot\eta_a^2 + \tau_{213}\cdot\eta_c$

$(\eta_{a,c})Q^2_{K_3}Q^2_{\Gamma_1^+}$ $\tau_{22}\ \eta_a,\eta_c\ = \tau_{220} + \tau_{221}\cdot\eta_a + \tau_{223}\cdot\eta_c$

$(\eta_{a,c})Q^2_{\Gamma_2^-}Q_{\Gamma_1^+}$ $\mu_{21}\ \eta_a,\eta_c\ = \mu_{210} + \mu_{211}\cdot\eta_a + \mu_{213}\cdot\eta_c$

$(\eta_{a,c})Q^2_{\Gamma_2^-}Q^2_{\Gamma_1^+}$ $\mu_{22}\ \eta_a,\eta_c\ = \mu_{220} + \mu_{221}\cdot\eta_a + \mu_{223}\cdot\eta_c$

C.4 Energy expansion

The internal energy *U* expansion for the hexagonal $YMnO_3$ including all symmetry-allowed terms to fourth order in terms of relevant ionic and strain degrees of freedom is given in Eq. C.1. This is the equivalent energy expansion as that given in Chapter 5 (Eq. 5.5) with notations of coefficients instead of their numerical values listed in Section C.5.

$$U[Q_{K_3}, Q_{\Gamma_2^-}, Q_{\Gamma_1^+}, \eta_a, \eta_c] = \alpha_{20} \cdot Q_{K_3}^2 + \alpha_{40} \cdot Q_{K_3}^4 + \beta_{20} \cdot Q_{\Gamma_2^-}^2 + \beta_{40} \cdot Q_{\Gamma_2^-}^4$$

$$+\gamma_{10} \cdot Q_{\Gamma_1^+} + \gamma_{20} \cdot Q_{\Gamma_1^+}^2 + \gamma_{30} \cdot Q_{\Gamma_1^+}^3 + \gamma_{40} \cdot Q_{\Gamma_1^+}^4 + \kappa_{310} \cdot Q_{K_3}^3 \cdot Q_{\Gamma_2^-} + \kappa_{220} \cdot Q_{K_3}^2 \cdot Q_{\Gamma_2^-}^2$$

$$+\tau_{210} \cdot Q_{K_3}^2 \cdot Q_{\Gamma_1^+} + \tau_{220} \cdot \boxed{Q_{K_3}^2 \cdot Q_{\Gamma_1^+}^2} + \mu_{210} \cdot Q_{\Gamma_2^-}^2 \cdot Q_{\Gamma_1^+} + \mu_{220} \cdot Q_{\Gamma_2^-}^2 \cdot Q_{\Gamma_1^+}^2$$

$$+\rho_{a2} \cdot \eta_a^2 + \rho_{c2} \cdot \eta_c^2 + \rho_{ac} \cdot \eta_a \cdot \eta_c + \rho_{a3} \cdot \eta_a^3 + \rho_{c3} \cdot \eta_c^3 + \rho_{ac21} \cdot \eta_a^2 \cdot \eta_c + \rho_{ac12} \cdot \eta_a \cdot \eta_c^2$$

$$+\alpha_{21} \cdot \eta_a \cdot Q_{K_3}^2 + \alpha_{212} \cdot \eta_a^2 \cdot Q_{K_3}^2 + \alpha_{41} \cdot \eta_a \cdot Q_{K_3}^4 + \alpha_{23} \cdot \eta_c \cdot Q_{K_3}^2 + \alpha_{232} \cdot \eta_c^2 \cdot Q_{K_3}^2 + \alpha_{43} \cdot \eta_c \cdot Q_{K_3}^4$$

$$+\alpha_{24} \cdot \eta_a \cdot \eta_c \cdot Q_{K_3}^2 + \alpha_{44} \cdot \eta_a \cdot \eta_c \cdot Q_{K_3}^4$$

$$+\beta_{21} \cdot \eta_a \cdot Q_{\Gamma_2^-}^2 + \beta_{41} \cdot \eta_a \cdot Q_{\Gamma_2^-}^4 + \beta_{23} \cdot \boxed{\eta_c \cdot Q_{\Gamma_2^-}^2} + \beta_{43} \cdot \boxed{\eta_c \cdot Q_{\Gamma_2^-}^4}$$

$$+\gamma_{11} \cdot \eta_a \cdot Q_{\Gamma_1^+} + \gamma_{112} \cdot \eta_a^2 \cdot Q_{\Gamma_1^+} + \gamma_{21} \cdot \eta_a \cdot Q_{\Gamma_1^+}^2 + \gamma_{212} \cdot \eta_a^2 \cdot Q_{\Gamma_1^+}^2 + \gamma_{31} \cdot \boxed{\eta_a \cdot Q_{\Gamma_1^+}^3} + \gamma_{41} \cdot \boxed{\eta_a \cdot Q_{\Gamma_1^+}^4}$$

$$+\gamma_{13} \cdot \eta_c \cdot Q_{\Gamma_1^+} + \gamma_{132} \cdot \eta_c^2 \cdot Q_{\Gamma_1^+} + \gamma_{23} \cdot \eta_c \cdot Q_{\Gamma_1^+}^2 + \gamma_{33} \cdot \boxed{\eta_c \cdot Q_{\Gamma_1^+}^3} + \gamma_{43} \cdot \boxed{\eta_c \cdot Q_{\Gamma_1^+}^4}$$

$$+\kappa_{311} \cdot \eta_a \cdot Q_{K_3}^3 \cdot Q_{\Gamma_2^-} + \kappa_{221} \cdot \eta_a \cdot Q_{K_3}^2 \cdot Q_{\Gamma_2^-}^2 + \kappa_{313} \cdot \eta_c \cdot Q_{K_3}^3 \cdot Q_{\Gamma_2^-} + \kappa_{223} \cdot \eta_c \cdot Q_{K_3}^2 \cdot Q_{\Gamma_2^-}^2$$

$$+\tau_{211} \cdot \eta_a \cdot Q_{K_3}^2 \cdot Q_{\Gamma_1^+} + \tau_{2112} \cdot \eta_a^2 \cdot Q_{K_3}^2 \cdot Q_{\Gamma_1^+} + \tau_{221} \cdot \boxed{\eta_a \cdot Q_{K_3}^2 \cdot Q_{\Gamma_1^+}^2} + \tau_{213} \cdot \eta_c \cdot Q_{K_3}^2 \cdot Q_{\Gamma_1^+} + \tau_{223} \cdot \boxed{\eta_c \cdot Q_{K_3}^2 \cdot Q_{\Gamma_1^+}^2}$$

$$+\mu_{211} \cdot \boxed{\eta_a \cdot Q_{\Gamma_2^-}^2 \cdot Q_{\Gamma_1^+}} + \mu_{221} \cdot \boxed{\eta_a \cdot Q_{\Gamma_2^-}^2 \cdot Q_{\Gamma_1^+}^2} + \mu_{213} \cdot \boxed{\eta_c \cdot Q_{\Gamma_2^-}^2 \cdot Q_{\Gamma_1^+}} + \mu_{223} \cdot \boxed{\eta_c \cdot Q_{\Gamma_2^-}^2 \cdot Q_{\Gamma_1^+}^2} \,. \tag{C.1}$$

The polynomial invariants were generated using the ISOTROPY software [61]. The character table for the most relevant K_3, Γ_2^- and Γ_1^+ modes included in the model is listed in Table C.1.

D_{6h} (6/mmm)	E	6	3	2_z	2_h	$2_{h'}$	I	-6	-3	m_z	m_d	m_v
Multiplicity	1	2	2	1	3	3	1	2	2	1	3	3
K_3	2	0	2	0	0	-2	0	-2	0	-2	2	0
Γ_2^- (A_{2u})	1	1	1	1	-1	-1	-1	-1	-1	-1	1	1
Γ_1^+ (A_{1g})	1	1	1	1	1	1	1	1	1	1	1	1

Table C.1 Character table for the K_3, Γ_2^- and Γ_1^+ modes. The top row indicates the symmetry operations. Space group: $P6_3/mmc$ (194). Point group: D_{6h} (6/mmm).

C.4.1 Double-well potential of K_3 mode

When $Q_{\Gamma_2^-} = Q_{\Gamma_1^+} = 0$ and $\eta_a = \eta_c = 0$, the energy expansion Eq. C.1 is written as:

$$E^{\text{individual mode}}\left[Q_{K_3}\right] = \alpha_{20} \cdot Q_{K_3}^2 + \alpha_{40} \cdot Q_{K_3}^4. \tag{C.2}$$

We froze K_3 mode in various amplitudes Q_{K_3} and computed the total energy of structure (Figure C.1). The coefficients of the second and fourth order terms are $\alpha_{20} = (-1.450 \pm 0.003)$ eV and $\alpha_{40} = (1.138 \pm 0.004)$ eV, respectively.

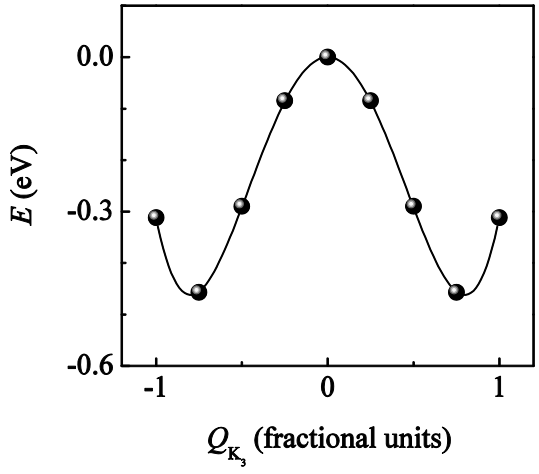

Figure C.1 Energy as a function of Q_{K_3}.

C.4.2 Single-well potential of Γ_2^- mode

When $Q_{K_3} = Q_{\Gamma_1^+} = 0$ and $\eta_a = \eta_c = 0,$ the energy expansion Eq. C.1 is written as:

$$E^{\text{individual mode}}\left[Q_{\Gamma_2^-}\right] = \beta_{20} \cdot Q_{\Gamma_2^-}^2 + \beta_{40} \cdot Q_{\Gamma_2^-}^4. \tag{C.3}$$

We froze Γ_2^- mode in various amplitudes $Q_{\Gamma_2^-}$ and computed the total energy of structure (Figure C.2). The coefficients of the second and fourth order terms are $\beta_{20} = (0.0193 \pm 0.0004)$ eV and $\beta_{40} = (-0.0004 \pm 0.0005)$ eV, respectively.

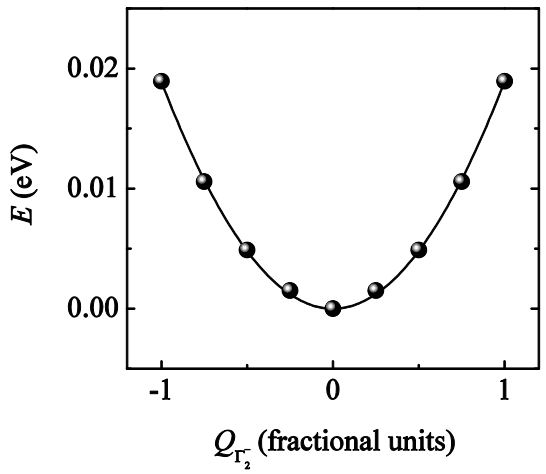

Figure C.2 Energy as a function of $Q_{\Gamma_2^-}$.

C.4.3 Single-well potential of Γ_1^+ mode

When $Q_{K_3} = Q_{\Gamma_2^-} = 0$ and $\eta_a = \eta_c = 0,$ the energy expansion Eq. C.1 is written as:

$$E^{\text{individual mode}}\left[Q_{\Gamma_1^+}\right] = \gamma_{10} \cdot Q_{\Gamma_1^+} + \gamma_{20} \cdot Q_{\Gamma_1^+}^2 + \gamma_{30} \cdot Q_{\Gamma_1^+}^3 + \gamma_{40} \cdot Q_{\Gamma_1^+}^4. \tag{C.4}$$

We froze Γ_1^+ mode in various amplitudes $Q_{\Gamma_1^+}$ and computed the total energy of structure (Figure C.3).

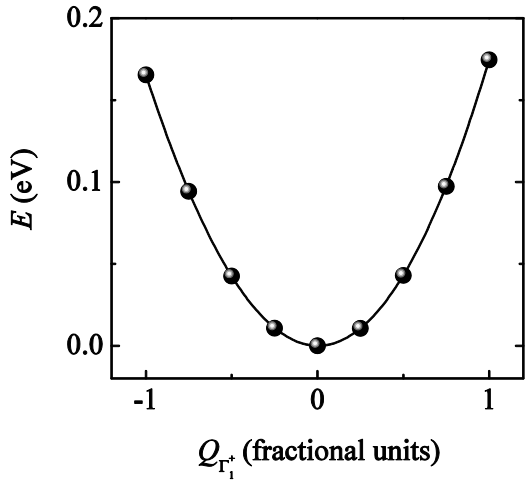

Figure C.3 Energy as a function of $Q_{\Gamma_1^+}$.

C.4.4 Coupled modes : K_3 and Γ_2^-

When Q_{K_3} is fixed, $Q_{\Gamma_1^+} = 0$ and $\eta_a = \eta_c = 0$, the energy expansion Eq. C.1 is written as:

$$E^{\text{mode coupling}}\left[Q_{K_3}, Q_{\Gamma_2^-}\right] = \kappa_{310} \cdot Q_{K_3}^3 \cdot Q_{\Gamma_2^-} + (\beta_{20} + \kappa_{220} \cdot Q_{K_3}^2) \cdot Q_{\Gamma_2^-}^2 + \beta_{40} \cdot Q_{\Gamma_2^-}^4. \qquad \text{(C.5)}$$

We froze the amplitude Q_{K_3} of K_3 mode in range of [0.25, 1] with step of 0.25 in fractional units and calculated the potential of Γ_2^- mode (Figure C.4) as described in Section C.4.2.

We plotted the first and second order terms of Eq. C.5 as a function of Q_{K_3} (Figure C.5) : the mode coupling coefficients are $\kappa_{310} = (-0.462 \pm 0.006)$ eV and $\kappa_{220} = (0.217 \pm 0.005)$ eV, respectively.

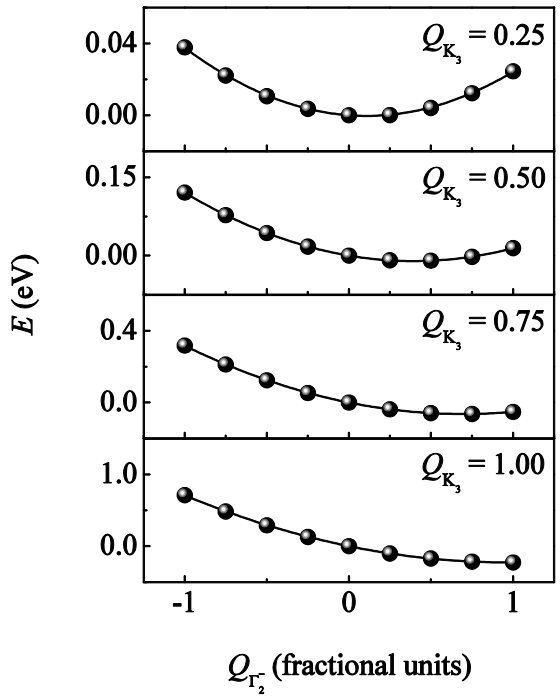

Figure C.4 Energy as a function of $Q_{\Gamma_2^-}$ at fixed Q_{K_3}.

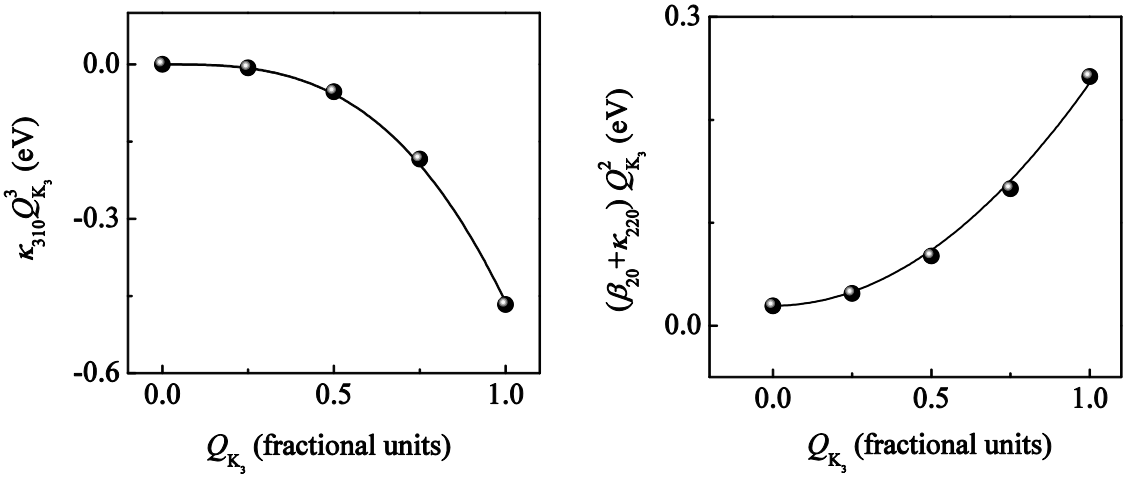

Figure C.5 Parameters $\kappa_{310}Q_{K_3}^3$ and $(\beta_{20}+\kappa_{220})Q_{K_3}^2$ as a function of Q_{K_3}.

C.4.5 Coupled modes : K_3 and Γ_1^+

When $Q_{\Gamma_1^+}$ is fixed, $Q_{\Gamma_2^-} = 0$ and $\eta_a = \eta_c = 0$, the energy expansion Eq. C.1 is written as:

$$E^{\text{mode coupling}}\left[Q_{K_3}, Q_{\Gamma_1^+}\right] = (\alpha_{20} + \tau_{210} \cdot Q_{\Gamma_1^+} + \tau_{220} \cdot Q_{\Gamma_1^+}^2) \cdot Q_{K_3}^2 + \alpha_{40} \cdot Q_{K_3}^4. \quad \text{(C.6)}$$

We froze the amplitude $Q_{\Gamma_1^+}$ of Γ_1^+ mode in range of [0.25, 1] with step of 0.25 in fractional units and calculated the potential of K_3 mode (Figure C.6) as described in Section C.4.1. We plotted the second order term of Eq. C.6 as a function of $Q_{\Gamma_1^+}$ (Figure C.6). The mode coupling coefficients are $\tau_{210} = (-0.1022 \pm 0.0004)$ eV and $\tau_{220} = (-0.0083 \pm 0.0005)$ eV. The dependence is linear thus we didn't include the term $Q_{\Gamma_1^+}^2 Q_{K_3}^2$ (Eq. C.6) in our model (Eq. C.1).

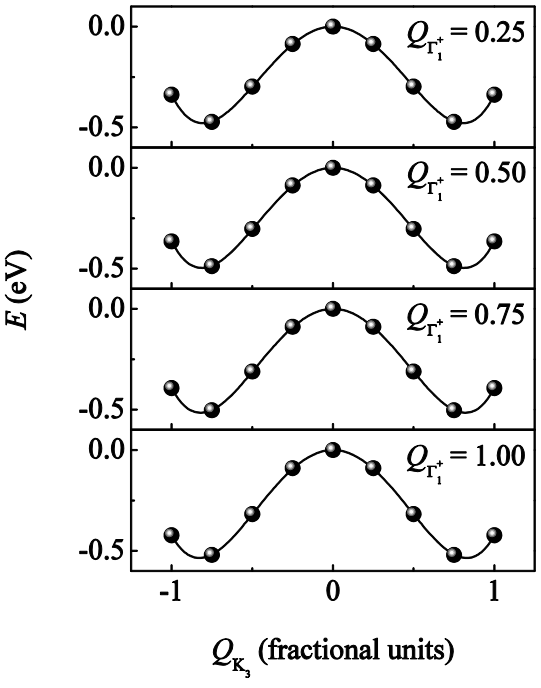

Figure C.6 Energy as a function of Q_{K_3} at fixed $Q_{\Gamma_1^+}$.

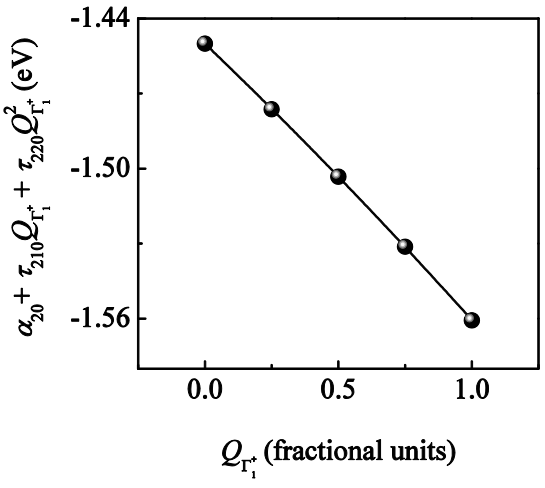

Figure C.7 Parameter $\alpha_{20} + \tau_{210} Q_{\Gamma_1^+} + \tau_{220} Q_{\Gamma_1^+}^2$ as a function of $Q_{\Gamma_1^+}$.

C.4.6 Coupled modes : Γ_2^- and Γ_1^+

When $Q_{\Gamma_1^+}$ is fixed, $Q_{K_3} = 0$ and $\eta_a = \eta_c = 0$, the energy expansion Eq. C.1 is written as:

$$E^{\text{mode coupling}}\left[Q_{\Gamma_2^-}, Q_{\Gamma_1^+}\right] = (\beta_{20} + \mu_{210} \cdot Q_{\Gamma_1^+} + \mu_{220} \cdot Q_{\Gamma_1^+}^2) \cdot Q_{\Gamma_2^-}^2 + \beta_{40} \cdot Q_{\Gamma_2^-}^4. \quad \text{(C.7)}$$

We froze the amplitude $Q_{\Gamma_1^+}$ of Γ_1^+ mode in the range of [0.25, 1] with step of 0.25 in fractional units and calculated the potential of Γ_2^- mode (Figure C.8) as described in Section C.4.2.

We plotted the second order term of Eq. C.7 as a function of $Q_{\Gamma_1^+}$ (Figure C.9). The mode coupling coefficients are $\mu_{210} = (-0.0062 \pm 0.0002)$ eV and $\mu_{220} = (0.0026 \pm 0.0002)$ eV.

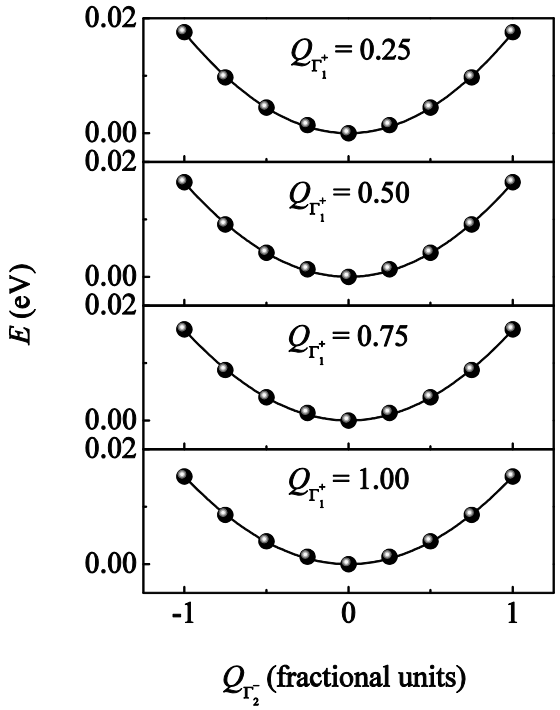

Figure C.8 Energy as a function of $Q_{\Gamma_2^-}$ at fixed $Q_{\Gamma_1^+}$.

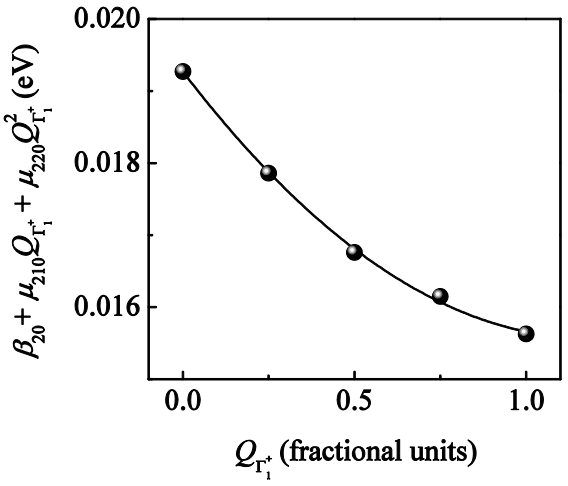

Figure C.9 Parameter $\beta_{20}+\mu_{210}\cdot Q_{\Gamma_1^+}+\mu_{220}\cdot Q^2_{\Gamma_1^+}$ as a function of $Q_{\Gamma_1^+}$.

C.4.7 Elastic energy

When $Q_{K_3}=Q_{\Gamma_2^-}=Q_{\Gamma_1^+}=0$, the energy expansion Eq. C.1 is written as:

$$E^{\text{elastic}}\ \eta_a,\eta_c\ =\rho_{a2}\cdot\eta_a^2+\rho_{c2}\cdot\eta_c^2+\rho_{ac}\cdot\eta_a\cdot\eta_c+\rho_{a3}\cdot\eta_a^3+\rho_{c3}\cdot\eta_c^3+\rho_{ac21}\cdot\eta_a^2\cdot\eta_c+\rho_{ac12}\cdot\eta_a\cdot\eta_c^2. \tag{C.8}$$

This is the expression of the elastic energy for a hexagonal structure with $\eta_x=\eta_y=\eta_a$ (in-plane lattice parameters for hexagonal structure are equal) and $\eta_z=\eta_c$.

First, we imposed $\eta_c=0$ (Figure C.10, a), then $\eta_a=0$ (Figure C.10, b) and calculated the total energy for various strain in the range of [-5 %, 5 %] with first step of 1 % and the rest - 0.5 %. The third order polynomial function fit gave the values of the elastic coefficients $\rho_{a2}=(973\pm1)$ eV, $\rho_{a3}=(-3313\pm25)$ eV, $\rho_{c2}=(445\pm1)$ eV and $\rho_{c3}=(-1843\pm53)$ eV, respectively.

The energy expansion Eq. C.8 when $\eta_a=\eta_c$ (Figure C.11, a) in terms of η_a is written as:

$$E\ \eta_a\ =(\rho_{a2}+\rho_{c2}+\rho_{ac})\cdot\eta_a^2+(\rho_{a3}+\rho_{c3}+\rho_{ac21}+\rho_{ac12})\cdot\eta_a^3. \tag{C.9}$$

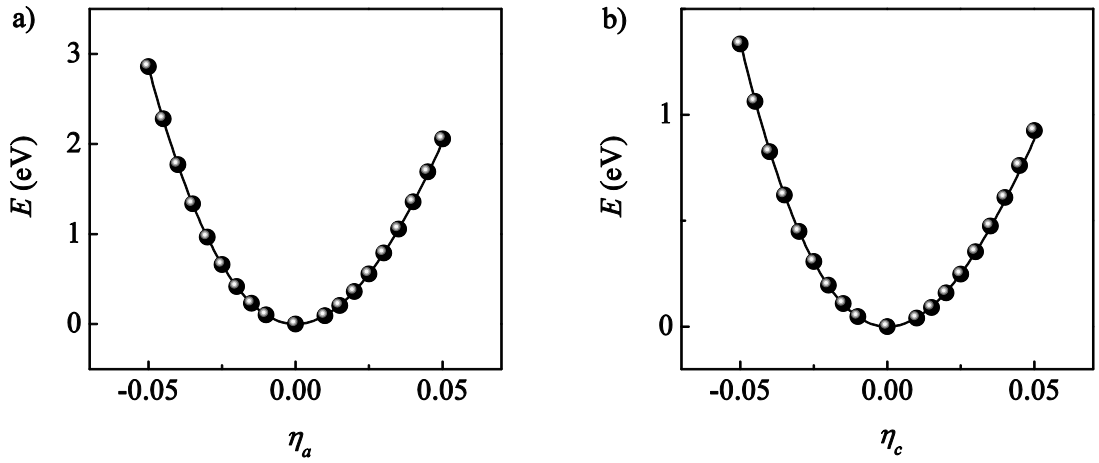

Figure C.10 Energy as a function of η_a (a) and η_c (b).

We determined the elastic coefficient $\rho_{ac} = (487 \pm 4)$ eV using the third order polynomial function. The determination of ρ_{ac21} and ρ_{ac12} required un additional equation. We imposed $\eta_a = -\eta_c$. The energy expansion in terms of η_a is written as follows

$$E\ \eta_a\ = (\rho_{a2} + \rho_{c2} - \rho_{ac}) \cdot \eta_a^2 + (\rho_{a3} - \rho_{c3} - \rho_{ac21} + \rho_{ac12}) \cdot \eta_a^3. \qquad \text{(C.10)}$$

The curve in Figure C.11 (b) is symmetric and the third order term in Eq. C10 is equal to zero. The coefficients are $\rho_{ac21} = (-1630 \pm 55)$ eV and $\rho_{ac12} = (-160 \pm 55)$ eV.

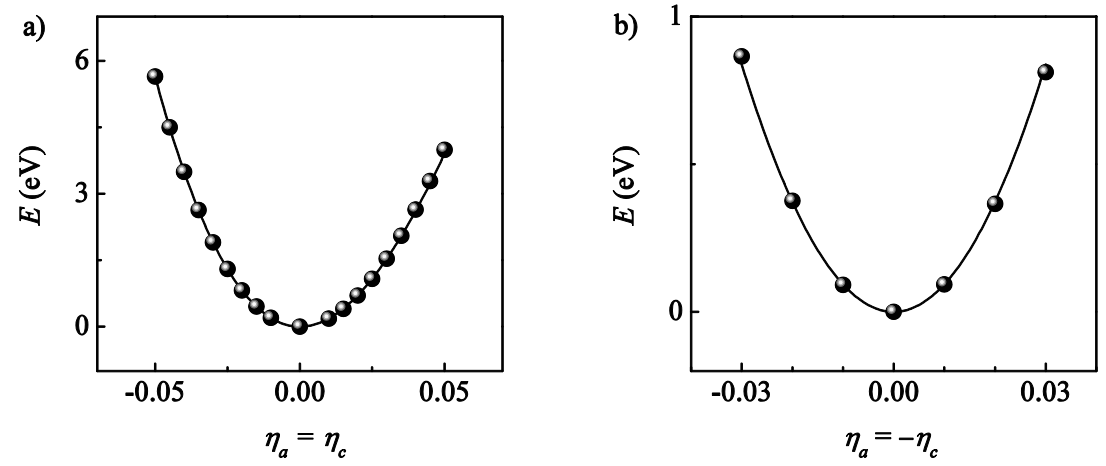

Figure C.11 Energy as a function of $\eta_a = \eta_c$ (a) and $\eta_a = -\eta_c$ (b).

C.4.8 Coupling with strain : K_3

When $Q_{\Gamma_2^-} = Q_{\Gamma_1^+} = 0$ and $E^{\text{elastic}} = 0$ the energy expansion Eq. C.1 is written as:

$$E^{\text{stain individual mode coupling}}\left[Q_{K_3}, \eta_a, \eta_c\right] = (\alpha_{20} + \alpha_{21}\cdot\eta_a + \alpha_{212}\cdot\eta_a^2 + \alpha_{23}\cdot\eta_c + \alpha_{232}\cdot\eta_c^2 + \alpha_{24}\cdot\eta_a\cdot\eta_c)\cdot Q_{K_3}^2$$

$$+(\alpha_{40} + \alpha_{41}\cdot\eta_a + \alpha_{43}\cdot\eta_c + \alpha_{44}\cdot\eta_a\cdot\eta_c)\cdot Q_{K_3}^4. \quad \text{(C.11)}$$

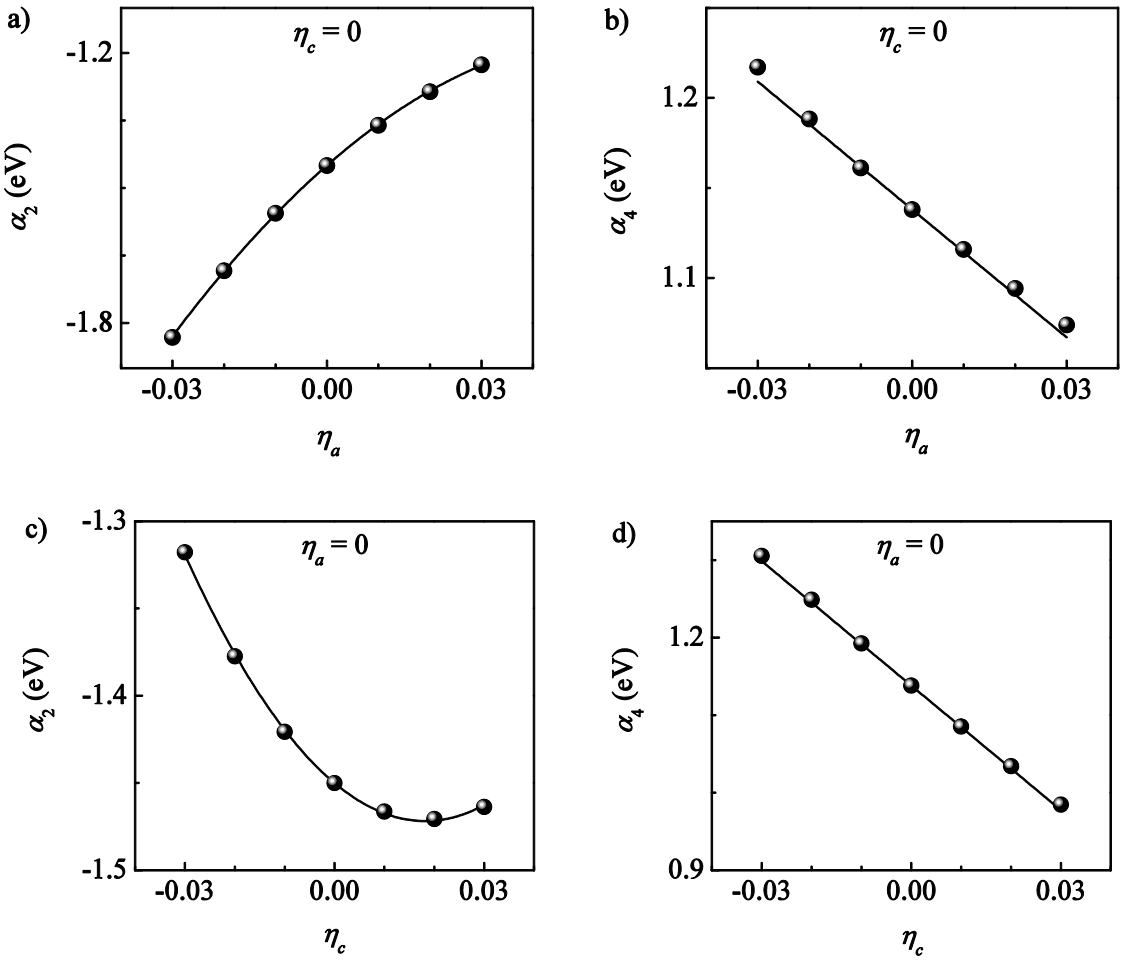

Figure C.12 Parameters α_2 (a, c) and α_4 (b, d) as a function of strain.

First, we imposed $\eta_c = 0$, then $\eta_a = 0$ and calculated the double-well potential of K_3 mode (as described in Section C.4.1) for various strain in the range of [-3%, +3%]. We plotted the parameters α_2 and α_4 as a function of strain (Figure C.12). The parameter α_2 shows the quadratic dependence along both *a*-axis and *c*-axis: the coefficients are $\alpha_{21} = (10.02 \pm 0.04)$ eV, $\alpha_{212} = (-88 \pm 2)$ eV (Figure C.12, a) and $\alpha_{23} = (-2.39 \pm 0.02)$ eV, $\alpha_{232} = (66 \pm 1)$ eV (Figure C.12, c). The fourth order parameter α_4 shows the linear dependence: the coefficients are $\alpha_{41} = (-2.37 \pm 0.09)$ eV (Figure C.12, b) and $\alpha_{43} = (-5.35 \pm 0.09)$ eV (Figure C.12, d), respectively.

The energy expansion Eq. C.11 when $\eta_a = \eta_c$ (Figure C.12) in terms of η_a is written as:

$$E^{\text{stain individual mode coupling}}\left[Q_{K_3}, \eta_a\right] = (\alpha_{20} + (\alpha_{21} + \alpha_{23}) \cdot \eta_a + (\alpha_{212} + \alpha_{232} + \alpha_{24}) \cdot \eta_a^2) \cdot Q_{K_3}^2 + (\alpha_{40} + (\alpha_{41} + \alpha_{43}) \cdot \eta_a + \alpha_{44} \cdot \eta_a^2) \cdot Q_{K_3}^4. \quad \text{(C.12)}$$

We plotted the parameters α_2 and α_4 as a function of strain (Figure C.13) and obtained the coefficients $\alpha_{24} = (1.06 \pm 0.09)$ eV and $\alpha_{44} = (19.1 \pm 0.6)$ eV, respectively.

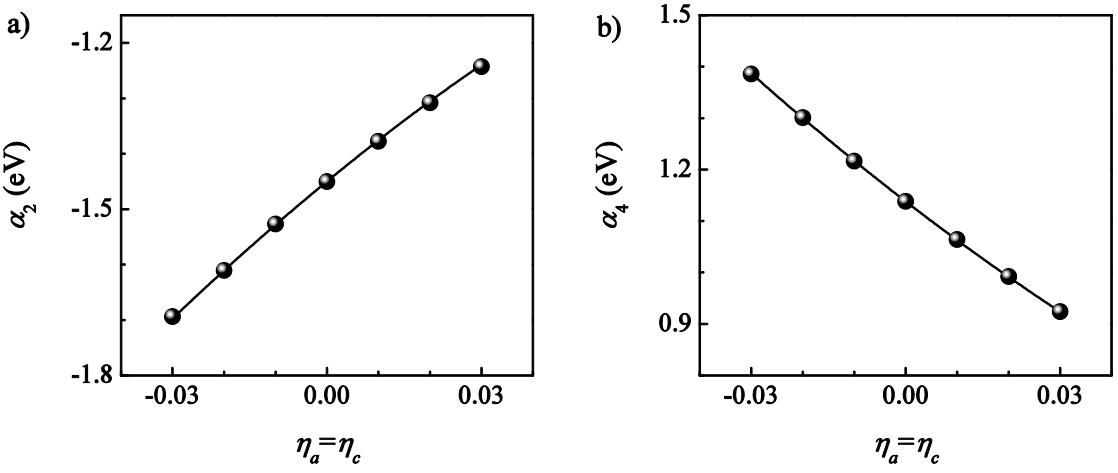

Figure C.13 Parameters α_2 (a) and α_4 (b) as a function of strain : $\eta_a = \eta_c$.

C.4.9 Coupling with strain : Γ_2^-

When $Q_{K_3} = Q_{\Gamma_1^+} = 0$ and $E^{\text{elastic}} = 0$ the energy expansion Eq. C.1 is written as:

$$E^{\text{strain individual mode coupling}}\left[Q_{\Gamma_2^-}, \eta_a, \eta_c\right] = (\beta_{20} + \beta_{21}\cdot\eta_a + \beta_{23}\cdot\eta_c)\cdot Q_{\Gamma_2^-}^2 + (\beta_{40} + \beta_{41}\cdot\eta_a + \beta_{43}\cdot\eta_c)\cdot Q_{\Gamma_2^-}^4 . \quad \text{(C.13)}$$

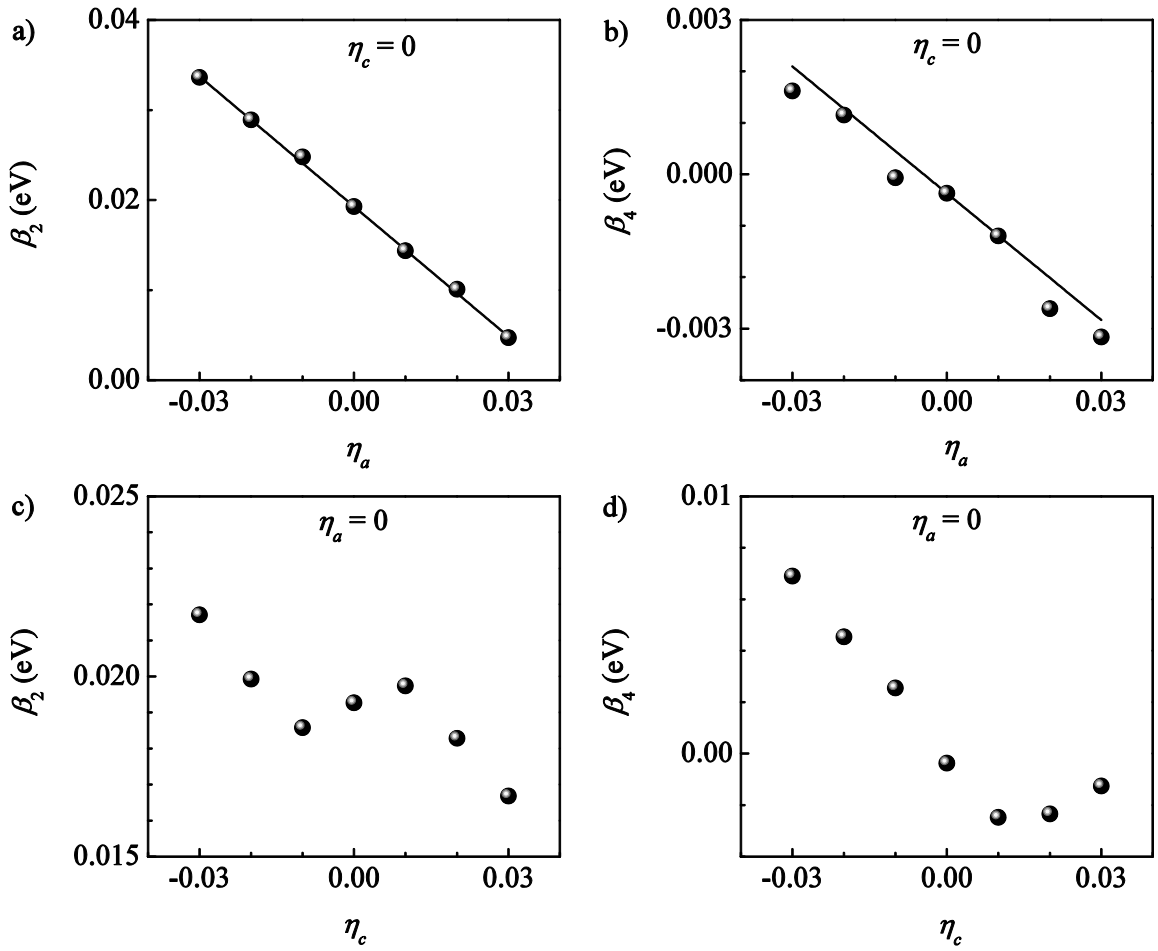

Figure C.14 Parameters β_2 (a, c) and β_4 (b, d) as a function of strain.

First, we imposed $\eta_c = 0$, then $\eta_a = 0$ and calculated the potential of Γ_2^- mode (as described in Section C.4.2) for various strain in the range of [-3%, +3%]. We plotted the parameters β_2

and β_4 as a function of strain. The coefficients are $\beta_{21} = (-0.481 \pm 0.007)$ eV (Figure C.14, a) and $\beta_{41} = (-0.082 \pm 0.008)$ eV (Figure C.14, b). The coupling of Γ_2^- mode with out-of plane strain η_c is weak. We didn't include the terms $\eta_c Q_{\Gamma_2^-}^2$ (Eq. C.13, Figure C.13, c) and $\eta_c Q_{\Gamma_2^-}^4$ (Eq. C.13, Figure C.13, d) in the model (Eq. C.1).

C.4.10 Coupling with strain : Γ_1^+

When $Q_{K_3} = Q_{\Gamma_2^-} = 0$ and $E^{\text{elastic}} = 0$ the energy expansion Eq. C.1 is written as:

$$\begin{aligned} E^{\text{strain individual mode coupling}}\left[Q_{\Gamma_1^+}, \eta_a, \eta_c\right] &= (\gamma_{10} + \gamma_{11}\cdot\eta_a + \gamma_{112}\cdot\eta_a^2 + \gamma_{13}\cdot\eta_c + \gamma_{132}\cdot\eta_c^2)\cdot Q_{\Gamma_1^+} \\ &+(\gamma_{20} + \gamma_{21}\cdot\eta_a + \gamma_{212}\cdot\eta_a^2 + \gamma_{23}\cdot\eta_c)\cdot Q_{\Gamma_1^+}^2 \\ &+(\gamma_{30} + \gamma_{31}\cdot\eta_a + \gamma_{33}\cdot\eta_c)\cdot Q_{\Gamma_1^+}^3 \\ &+(\gamma_{40} + \gamma_{41}\cdot\eta_a + \gamma_{43}\cdot\eta_c)\cdot Q_{\Gamma_1^+}^4. \end{aligned} \quad \text{(C.14)}$$

First, we imposed $\eta_c = 0$, then $\eta_a = 0$ and calculated the potential of Γ_1^+ mode (as described in Section C.4.3) for various strain in the range of [-3%, +3%]. We plotted the parameters γ_1 and γ_2 (Figure C.15), γ_3 (Figure C.16) and γ_4 (Figure C.17) as a function of strain.

The first order parameter γ_1 shows the quadratic coupling with strain along both *a*-axis and *c*-axis : the coefficients are $\gamma_{11} = (5.377 \pm 0.009)$ eV, $\gamma_{112} = (-30.8 \pm 0.4)$ eV (Figure C.15, a) and $\gamma_{13} = (-9.31 \pm 0.02)$ eV, $\gamma_{132} = (56.9 \pm 0.6)$ eV (Figure C.15, c), respectively. The second order coefficient γ_2 shows the quadratic coupling with η_a and linear coupling with η_c : the coefficients are $\gamma_{21} = (-0.302 \pm 0.005)$ eV, $\gamma_{212} = (1.2 \pm 0.2)$ eV (Figure C.15, b) and $\gamma_{23} = (-0.71 \pm 0.01)$ eV (Figure C.15, d), respectively.

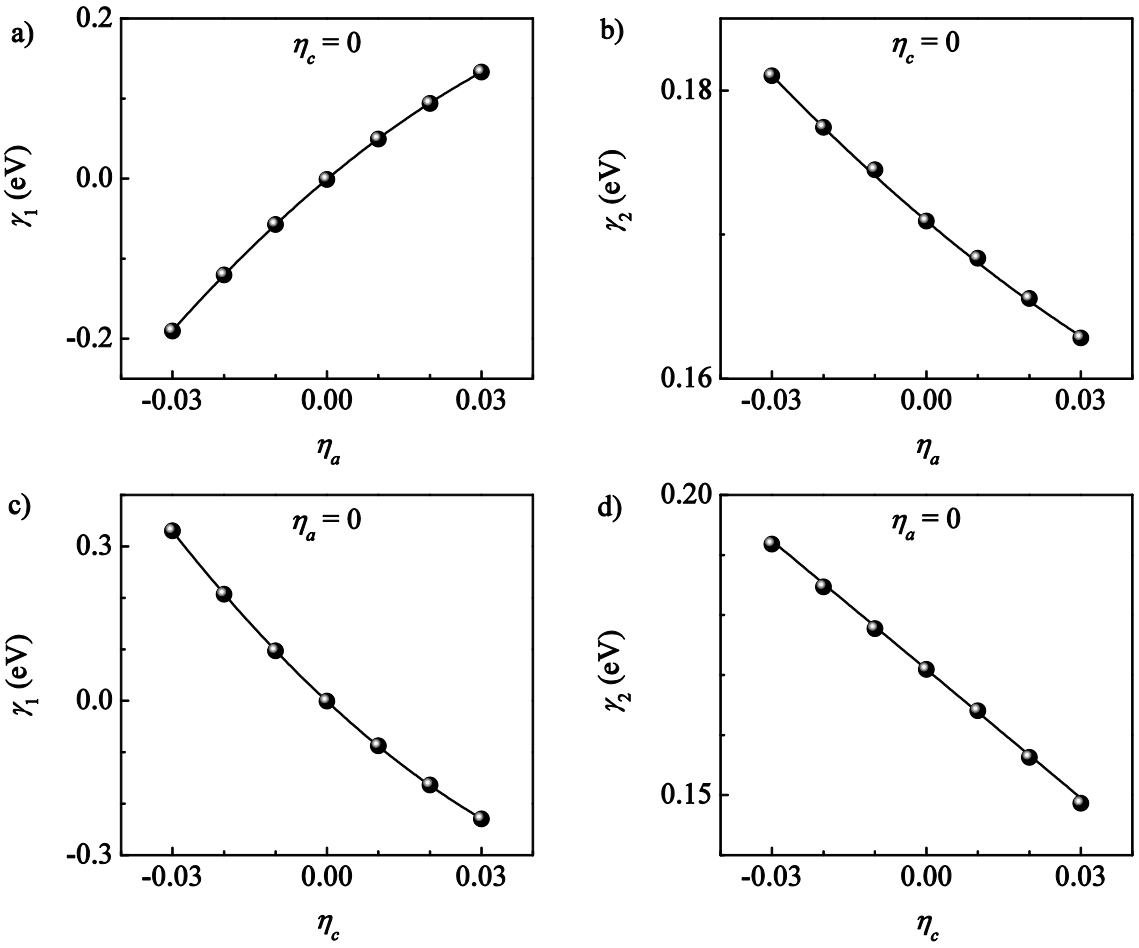

Figure C.15 Parameters γ_1 (a, c) and γ_2 (b, d) as a function of strain.

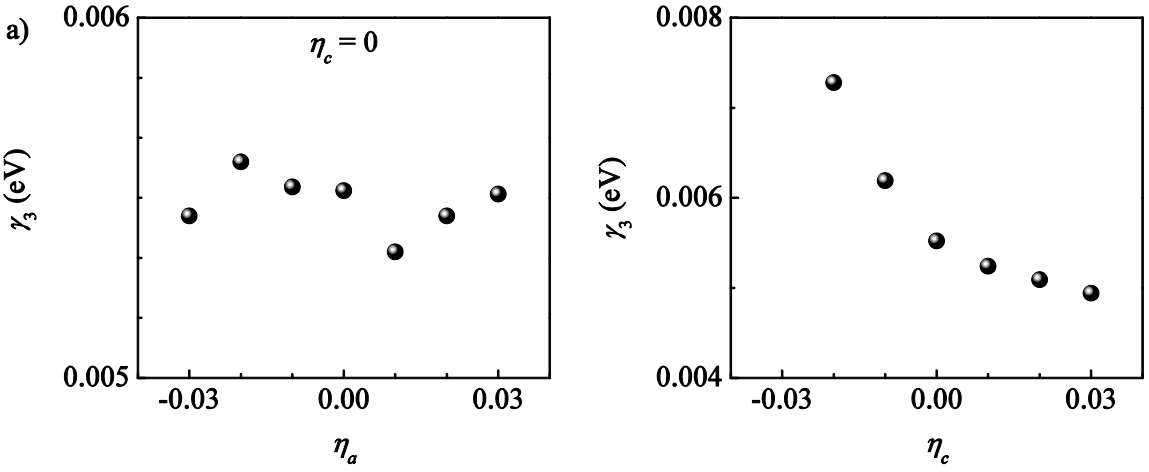

Figure C.16 Parameter γ_3 as a function of η_a (a) and η_c (b).

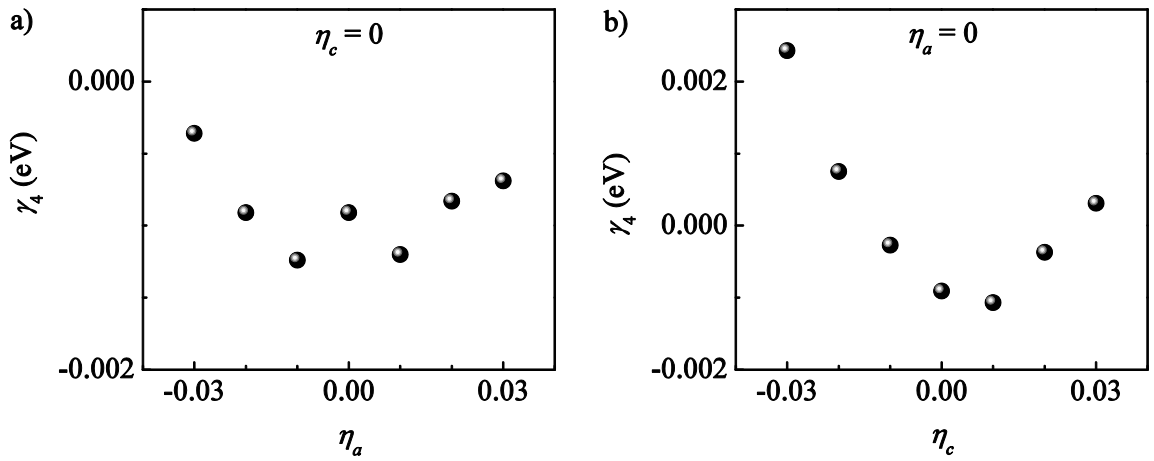

Figure C.17 Parameter γ_4 as a function of η_a (a) and η_c (b).

The higher order coupling with strain of Γ_1^+ mode is negligible. We didn't include the terms $\eta_a Q^3_{\Gamma_1^+}$ and $\eta_a Q^4_{\Gamma_1^+}$ (Eq. C.14, Figure C.16), $\eta_c Q^3_{\Gamma_1^+}$, and $\eta_c Q^4_{\Gamma_1^+}$ (Eq. C.14, Figure C.17) in the model (Eq. C.1).

C.4.11 Coupling with strain : K_3 and Γ_2^- coupled modes

When Q_{K_3} is fixed, $Q_{\Gamma_1^+} = 0$ and $E^{\text{elastic}} = 0$, the energy expansion Eq. C.1 is written as:

$$E^{\text{strain mode coupling}}\left[Q_{K_3}, Q_{\Gamma_2^-}, \eta_a, \eta_c\right] = (\kappa_{310} + \kappa_{311}\cdot\eta_a + \kappa_{313}\cdot\eta_c)\cdot Q^3_{K_3}\cdot Q_{\Gamma_2^-}$$
$$+(\beta_{20} + \beta_{21}\cdot\eta_a + \beta_{23}\cdot\eta_c + (\kappa_{220} + \kappa_{221}\cdot\eta_a + \kappa_{223}\cdot\eta_c)\cdot Q^2_{K_3})\cdot Q^2_{\Gamma_2^-}$$
$$+(\beta_{40} + \beta_{41}\cdot\eta_a + \beta_{43}\cdot\eta_c)\cdot Q^4_{\Gamma_2^-}. \quad \text{(C.15)}$$

We calculated the mode coupling coefficients κ_{31} and κ_{22} of K_3 and Γ_2^- modes (as described in Section C.4.4) for various strain in the range of [-3%, +3%] (Figure C.18). The coefficients

are $\kappa_{311} = (0.69 \pm 0.01)$ eV (Figure C.18, a), $\kappa_{221} = (-0.267 \pm 0.008)$ eV (Figure C.18, b), $\kappa_{313} = (2.57 \pm 0.03)$ eV (Figure C.18, c), and $\kappa_{223} = (-1.33 \pm 0.03)$ eV (Figure C.18, d).

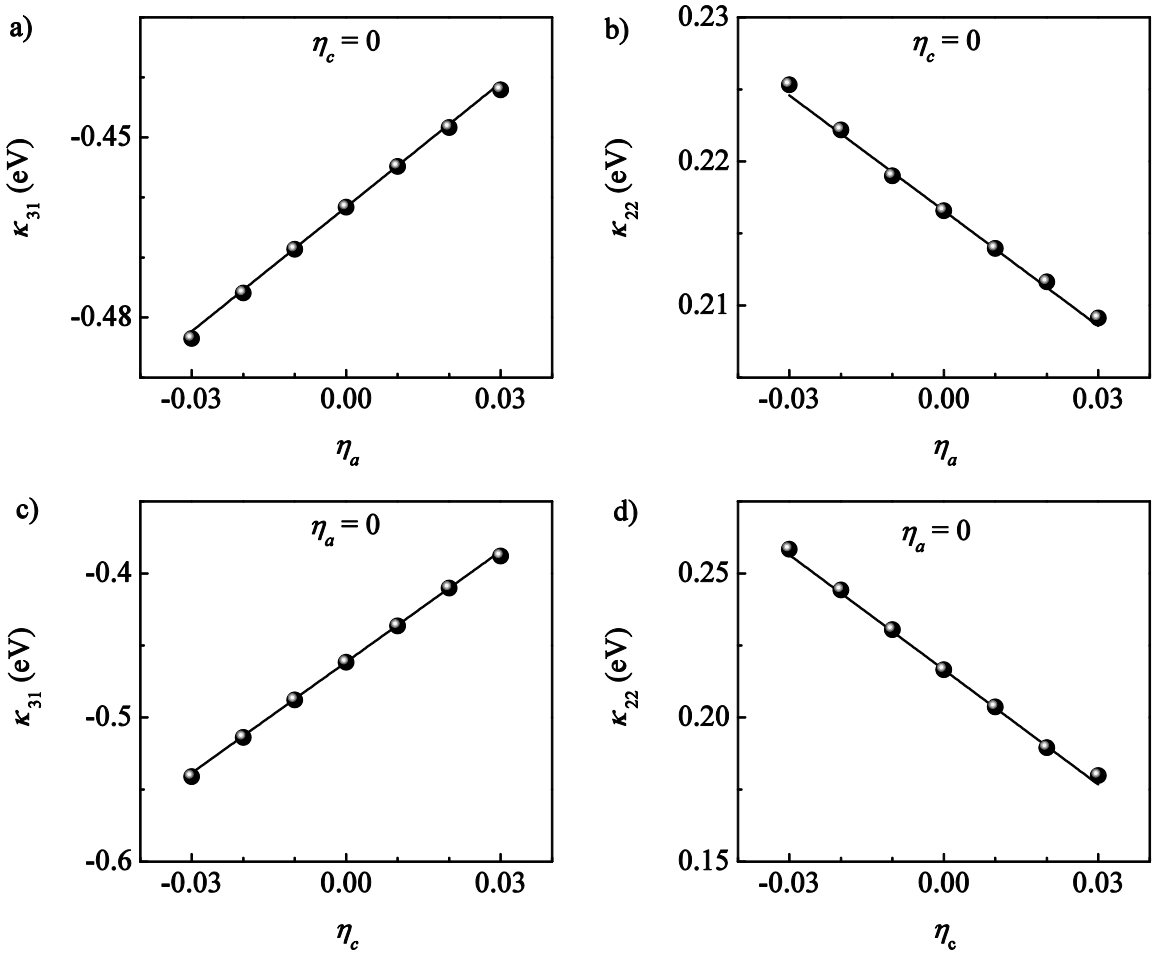

Figure C.18 Coefficients κ_{31} (a, c) and κ_{22} (b, d) as a function of strain.

C.4.12 Coupling with strain : K_3 and Γ_1^+ coupled modes

When $Q_{\Gamma_1^+}$ is fixed, $Q_{\Gamma_2^-} = 0$ and $E^{\text{elastic}} = 0$, the energy expansion Eq. C.1 is written as:

$$E^{\text{strain mode coupling}}\left[Q_{K_3}, Q_{\Gamma_1^+}, \eta_a, \eta_c\right] = ((\alpha_{20} + \alpha_{21}\cdot\eta_a + \alpha_{212}\cdot\eta_a^2 + \alpha_{23}\cdot\eta_c + \alpha_{232}\cdot\eta_c^2 + \alpha_{24}\cdot\eta_a\cdot\eta_c$$

$$+(\tau_{210} + \tau_{211}\cdot\eta_a + \tau_{2112}\cdot\eta_a^2 + \tau_{213}\cdot\eta_c)\cdot Q_{\Gamma_1^+}$$

$$+(\tau_{220} + \tau_{221}\cdot\eta_a + \tau_{223}\cdot\eta_c)\cdot Q_{\Gamma_1^+}^2)\cdot Q_{K_3}^2$$

$$+(\alpha_{40} + \alpha_{41}\cdot\eta_a + \alpha_{43}\cdot\eta_c + \alpha_{44}\cdot\eta_a\cdot\eta_c)\cdot Q_{K_3}^4.$$

(C.16)

We calculated the mode coupling coefficients τ_{21} and τ_{22} of K_3 and Γ_1^+ modes (as described in Section C.4.5) for various strain in the range of [-3%, +3%]. The coefficient τ_{21} shows the quadratic mode coupling with in-plane and linear coupling with out-of plane strain: $\tau_{211} = (-0.659 \pm 0.005)$ eV, $\tau_{2112} = (4.5 \pm 0.2)$ eV and $\tau_{213} = (0.878 \pm 0.008)$ eV (Figure C.19, a and b), respectively.

The higher order mode coupling with strain is negligible (Figure C.20). We didn't include the terms $\eta_a Q_{K_3}^2 Q_{\Gamma_1^+}^2$ (Eq. C.16, Figure C.19, a) and $\eta_c Q_{K_3}^2 Q_{\Gamma_1^+}^2$ (Eq. C.16, Figure C.20, b) in the model (Eq. C.1).

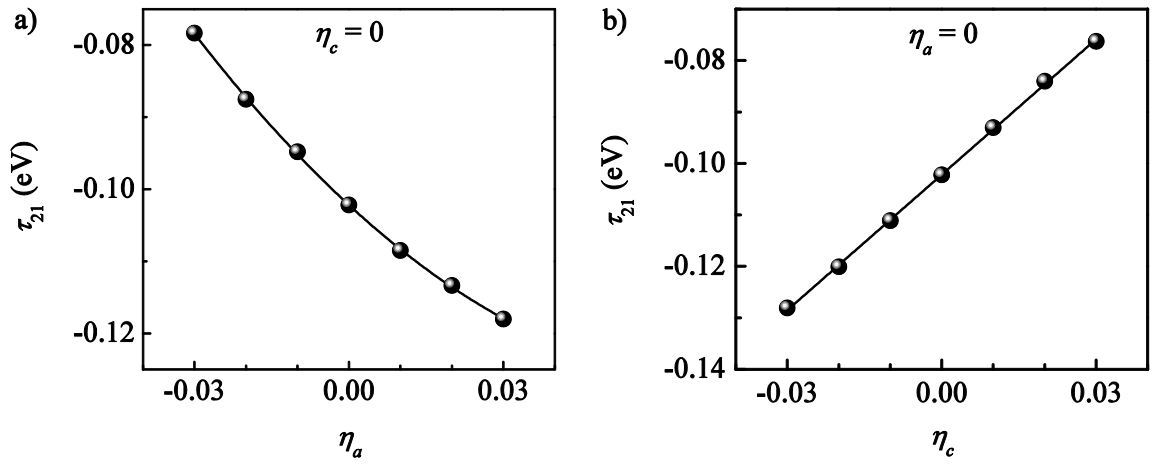

Figure C.19 Coefficient τ_{21} as a function of η_a (a), η_c (b).

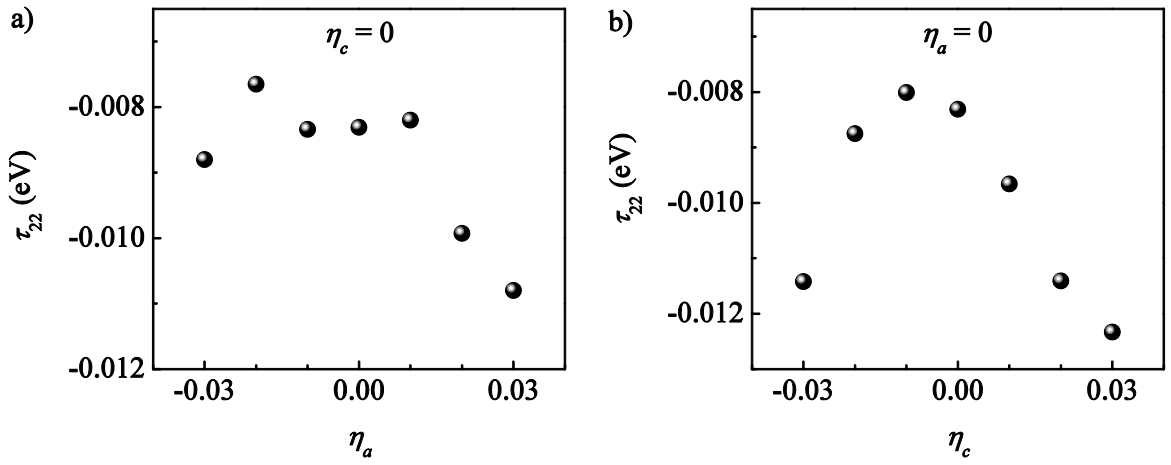

Figure C.20 Coefficient τ_{22} as a function of η_a (a), η_c (b).

C.4.13 Coupling with strain : Γ_2^- and Γ_1^+ coupled modes

When $Q_{\Gamma_1^+}$ is fixed, $Q_{K_3} = 0$ and $E^{\text{elastic}} = 0$, the energy expansion Eq. C.1 is written as:

$$\begin{aligned} E^{\text{strain mode coupling}}\left[Q_{\Gamma_2^-}, Q_{\Gamma_1^+}, \eta_a, \eta_c\right] = ((&\beta_{20} + \beta_{21}\cdot\eta_a + \beta_{23}\cdot\eta_c \\ &+(\mu_{210} + \mu_{211}\cdot\eta_a + \mu_{213}\cdot\eta_c)\cdot Q_{\Gamma_1^+} \\ &+(\mu_{220} + \mu_{221}\cdot\eta_a + \mu_{223}\cdot\eta_c)\cdot Q_{\Gamma_1^+}^2)\cdot Q_{\Gamma_2^-}^2 \\ &+(\beta_{40} + \beta_{41}\cdot\eta_a + \beta_{43}\cdot\eta_c)\cdot Q_{\Gamma_2^-}^4. \end{aligned} \quad \text{(C.17)}$$

We calculated the mode coupling coefficients μ_{21} and μ_{22} of Γ_2^- and Γ_1^+ modes (as described in Section C.4.6) for various strain in the range of [-3%, +3%]. As we can see in Figure C.21, the coupling with strain is negligible, thus the terms $\eta_a Q_{\Gamma_2^-}^2 Q_{\Gamma_1^+}$ and $\eta_a Q_{\Gamma_2^-}^2 Q_{\Gamma_1^+}^2$ (Eq. C.17, Figure C.21, a and b, respectively), $\eta_c Q_{\Gamma_2^-}^2 Q_{\Gamma_1^+}$ and $\eta_c Q_{\Gamma_2^-}^2 Q_{\Gamma_1^+}^2$ (Eq. C.17, Figure C.21, c and d, respectively) are not included in the model (Eq. C.1).

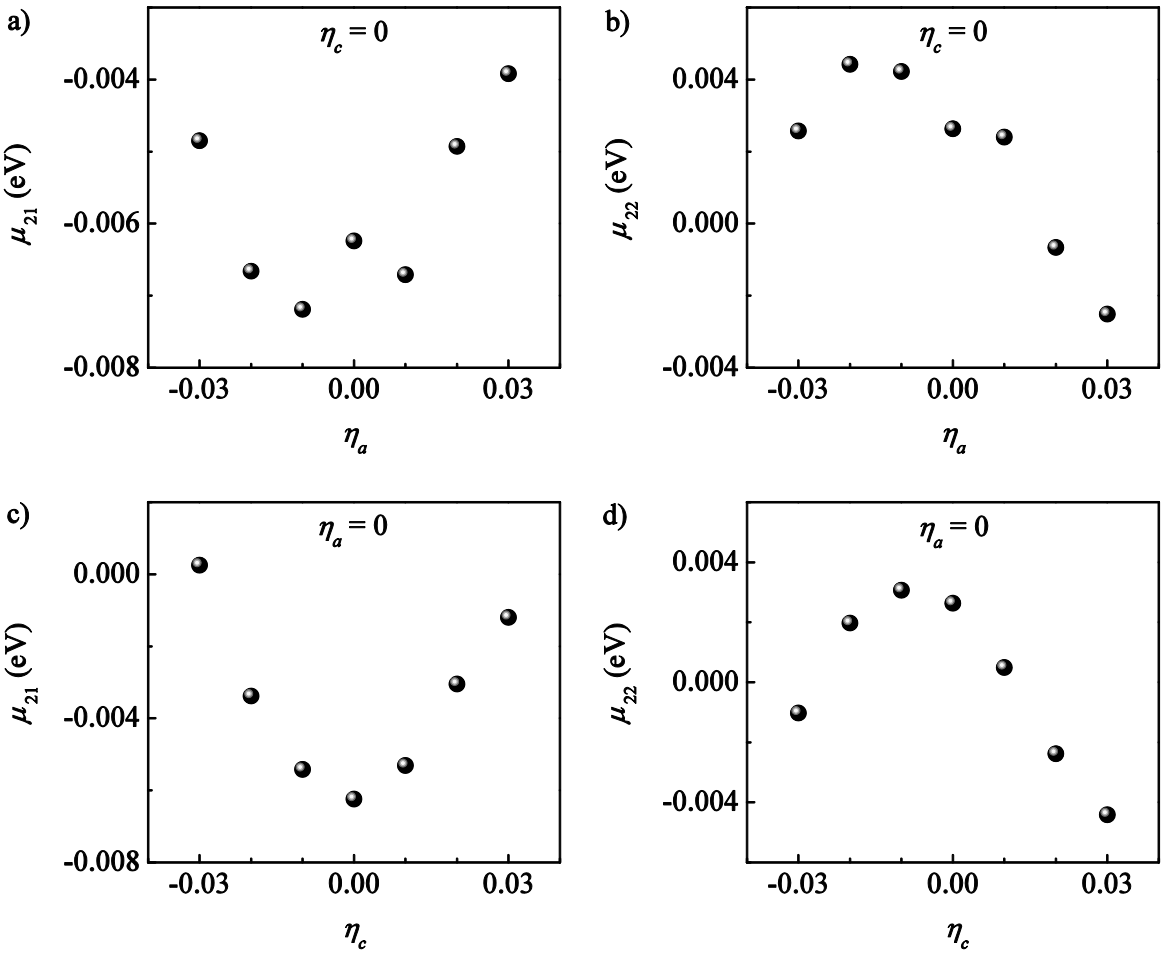

Figure C.21 Coefficients μ_{21} (a, c) and μ_{22} (b, d) as a function of strain.

C.5 Summary of coefficients

	Coefficient	eV	Section
$Q^2_{K_3}$	α_{20}	–1.450	C.4.1
$Q^4_{K_3}$	α_{40}	1.138	C.4.1
$Q^2_{\Gamma_2^-}$	β_{20}	0.0193	C.4.2
$Q^4_{\Gamma_2^-}$	β_{40}	–0.0004	C.4.2

	Coefficient	eV	Section
$Q_{\Gamma_1^+}$	γ_{10}	–0.0010	C.4.3
$Q^2_{\Gamma_1^+}$	γ_{20}	0.1710	C.4.3
$Q^3_{\Gamma_1^+}$	γ_{30}	0.0055	C.4.3
$Q^4_{\Gamma_1^+}$	γ_{40}	–0.0009	C.4.3
$Q^3_{\mathrm{K}_3} Q_{\Gamma_2^-}$	κ_{310}	–0.462	C.4.4
$Q^2_{\mathrm{K}_3} Q^2_{\Gamma_2^-}$	κ_{220}	0.217	C.4.4
$Q^2_{\mathrm{K}_3} Q_{\Gamma_1^+}$	τ_{210}	–0.1022	C.4.5
$Q^2_{\mathrm{K}_3} Q^2_{\Gamma_1^+}$	τ_{220}	–0.0083	C.4.5
$Q^2_{\Gamma_2^-} Q_{\Gamma_1^+}$	μ_{210}	–0.0062	C.4.6
$Q^2_{\Gamma_2^-} Q^2_{\Gamma_1^+}$	μ_{220}	0.0026	C.4.6
η_a^2	ρ_{a2}	973	C.4.7
η_a^3	ρ_{a3}	-3313	C.4.7
η_c^2	ρ_{c2}	445	C.4.7
η_c^3	ρ_{c3}	-1843	C.4.7
$\eta_a \eta_c$	ρ_{ac}	487	C.4.7
$\eta_a^2 \eta_c$	ρ_{ac21}	–1630	C.4.7
$\eta_a \eta_c^2$	ρ_{ac12}	–160	C.4.7
$\eta_a Q^2_{\mathrm{K}_3}$	α_{21}	10.02	C.4.8
$\eta_a^2 Q^2_{\mathrm{K}_3}$	α_{212}	-88	C.4.8
$\eta_a Q^4_{\mathrm{K}_3}$	α_{41}	-2.37	C.4.8
$\eta_c Q^2_{\mathrm{K}_3}$	α_{23}	-2.39	C.4.8
$\eta_c^2 Q^2_{\mathrm{K}_3}$	α_{232}	66	C.4.8
$\eta_c Q^4_{\mathrm{K}_3}$	α_{43}	-5.35	C.4.8
$\eta_a \eta_c Q^2_{\mathrm{K}_3}$	α_{24}	1.06	C.4.8

	Coefficient	eV	Section
$\eta_a\eta_c Q^4_{K_3}$	α_{44}	19.1	C.4.8
$\eta_a Q^2_{\Gamma_2^-}$	β_{21}	-0.481	C.4.9
$\eta_a Q^4_{\Gamma_2^-}$	β_{41}	-0.082	C.4.9
$\eta_c Q^2_{\Gamma_2^-}$	β_{23}	-	C.4.9
$\eta_c Q^4_{\Gamma_2^-}$	β_{43}	-	C.4.9
$\eta_a Q_{\Gamma_1^+}$	γ_{11}	5.377	C.4.10
$\eta_a^2 Q_{\Gamma_1^+}$	γ_{112}	-30.8	C.4.10
$\eta_a Q^2_{\Gamma_1^+}$	γ_{21}	-0.302	C.4.10
$\eta_a^2 Q^2_{\Gamma_1^+}$	γ_{212}	1.2	C.4.10
$\eta_a Q^3_{\Gamma_1^+}$	γ_{31}	-	C.4.10
$\eta_a Q^4_{\Gamma_1^+}$	γ_{41}	-	C.4.10
$\eta_c Q_{\Gamma_1^+}$	γ_{13}	-9.31	C.4.10
$\eta_c^2 Q_{\Gamma_1^+}$	γ_{132}	56.9	C.4.10
$\eta_c Q^2_{\Gamma_1^+}$	γ_{23}	-0.71	C.4.10
$\eta_c Q^3_{\Gamma_1^+}$	γ_{33}	-	C.4.10
$\eta_c Q^4_{\Gamma_1^+}$	γ_{43}	-	C.4.10
$\eta_a Q^3_{K_3} Q_{\Gamma_2^-}$	κ_{311}	0.69	C.4.11
$\eta_a Q^2_{K_3} Q^2_{\Gamma_2^-}$	κ_{221}	-0.267	C.4.11
$\eta_c Q^3_{K_3} Q_{\Gamma_2^-}$	κ_{313}	2.57	C.4.11
$\eta_c Q^2_{K_3} Q^2_{\Gamma_2^-}$	κ_{223}	-1.33	C.4.11
$\eta_a Q^2_{K_3} Q_{\Gamma_1^+}$	τ_{211}	-0.659	C.4.12
$\eta_a^2 Q^2_{K_3} Q_{\Gamma_1^+}$	τ_{2112}	4.5	C.4.12
$\eta_a Q^2_{K_3} Q^2_{\Gamma_1^+}$	τ_{221}	-	C.4.12
$\eta_c Q^2_{K_3} Q_{\Gamma_1^+}$	τ_{213}	0.878	C.4.12
$\eta_c Q^2_{K_3} Q^2_{\Gamma_1^+}$	τ_{223}	-	C.4.12

	Coefficient	eV	Section
$\eta_a Q_{\Gamma_2^-}^2 Q_{\Gamma_1^+}$	μ_{211}	-	C.4.13
$\eta_a Q_{\Gamma_2^-}^2 Q_{\Gamma_1^+}^2$	μ_{221}	-	C.4.13
$\eta_c Q_{\Gamma_2^-}^2 Q_{\Gamma_1^+}$	μ_{213}	-	C.4.13
$\eta_c Q_{\Gamma_2^-}^2 Q_{\Gamma_1^+}^2$	μ_{223}	-	C.4.13

Bibliography

[1] James S. Langer (editor), *Annual Review of Condensed Matter Physics* (Palo Alto, California, 2011).

[2] C. Li, K. C. K. Soh and P. Wu, *Formability of ABO_3 perovskites*, J. Alloy. Compd. 372, 40 (2004).

[3] M. Fiebig, *Revival of the magnetoelectric effect*, J. Phys. D-Appl. Phys. 38, R123 (2005).

[4] J. F. Jr. Brown, R. M. Hornreich and S. Shtrikman, *Upper bound on the magnetoelectric*, Phys. Rev. 168, 574 (1968).

[5] W. Eerenstein, N. D. Mathur and J. F. Scott., *Multiferroic and magnetoelectric materials*, Nature 442, 756 (2006).

[6] E. Ascher, H. Rieder, H. Schmid and H. Stossel, *Some properties of ferromagnetoelectric nickel-iodine boracite, Ni3Bi7O13I*, J. Appl. Phys. 37, 1404 (1966).

[7] R. Resta, *Macroscopic polarization in crystalline dielectrics: the geometric phase approach*, Rev. Mod. Phys. 66, 899 (1994).

[8] H. L. Yakel, W. C. Koehler, E. F. Bertaut, E. F. Forrat, *On the crystal structure of the manganese (III) trioxides of the heavy lanthanide and yttrium*, Acta Crystallogr. 16, 957 (1963).

[9] G. A. Smolenskii, V. A. Bokov, *Coexistence of magnetic and electric ordering in crystals*, J. Appl. Phys. 35, 915 (1964).

[10] N. Fujimura, T. Ishida, T. Yoshimura and T. Ito, *Epitaxially grown $YMnO_3$ film: New candidate for nonvolatile memory devices* , Appl. Phys. Lett. 69, 1011 (1996).

[11] K. Lukaszewicz and J. Karut-Kalicinska, *X-Ray investigations of the crystal structure and phase transitions of $YMnO_3$*, Ferroelectrics 7, 81 (1974).

[12] S. Lee, A. Pirogov, M. Kang, K.-H. Jang, M. Kamiyama, S.-W. Cheong, F. Gozzo, N. Shin, H. Kimura, Y. Noda and J.-G. Park, *Giant magneto-elastic coupling in multiferroic hexagonal manganites*, Nature 451, 805 (2008).

[13] T. Katsufuji, S. Mori, M. Masaki, Y. Moritomo, N. Yamamoto and H. Takagi, *Dielectric and magnetic anomalies and spin frustration in hexagonal $RMnO_3$ (R=Y, Yb, and Lu)*, Phys. Rev. B 64, 104419 (2001).

[14] M. Fiebig, Th. Lottermoser, D. Frölich and R. V. Pisarev, *Observation of coupled magnetic and electric domains*, Nature 419, 818 (2002).

[15] B. B. van Aken, T. T. M. Palstra, A. Filippetti and N. A. Spaldin, *The origin of ferroelectricity in magnetoelectric $YMnO_3$*, Nat. Mater. 3, 164 (2004).

[16] C. J. Fennie and K. M. Rabe, *Ferroelectric transition in $YMnO_3$ from first principles*, Phys. Rev. B 72, 100103 (R) (2005).

[17] M. Fiebig, D. Fröhlich, K. Kohn, St. Leute, Th. Lottermoser, V. V. Pavlov and R. V. Pisarev, *Determination of the magnetic symmetry of hexagonal manganites by second harmonic generation*, Phys. Rev. Lett. 84, 5620 (2000).

[18] P. Hohenberg and W. Kohn, *Inhomogeneous Electron Gas*, Phys. Rev. 136, B864 (1964).

[19] W. Kohn and L. J. Sham, *Self-consistent equations including exchange and correlation*, Phys. Rev. 140, A1133 (1965).

[20] R. M. Martin., *Electronic Structure, Basic Theory and Practical Methods* (Cambridge, University Press, 2004).

[21] D. M. Ceperley and B. J. Alder, *Ground state of the electron gas by a stochastic method*, Phys. Rev. Lett. 45, 566 (1980).

[22] J. P. Perdew, K. Burke and Y. Wang, *Generalized gradient approximation for the exchange-correlation hole of a many-body system*, Phys. Rev. B 54, 16533 (1996).

[23] Z. Wu and R. E. Cohen, *More accurate generalized gradient approximation for solids*, Phys. Rev. B 73, 235116 (2006).

[24] D. I. Bilc, R. Orlando, R. Shaltaf, G. M. Rignanese, J. Iniguez and Ph. Ghosez, *Hybrid exchange-correlation functional for accurate prediction of the electronic and structural properties of ferroelectric oxides*, Phys. Rev. B 77, 165107 (2008).

[25] A. I. Liechtenstein, V. I. Anisimov and J. Zaanen, *Density-functional theory and strong interactions: Orbital ordering in Mott-Hubbard insulators*, Phys. Rev. B 52, R5467 (1995).

[26] X. Gonze, J. M. Beuken, R. Caracas, F. Detraux, M. Fuchs, G. M. Rignanese, L. Sindic, M. Verstraete, G. Zerah, F. Jollet, M. Torrent, A. Roy, M. Mikami, Ph. Ghosez, J. Y. Raty and D. C. Allan, *First-principles computation of material properties: the ABINIT software project*, Comput. Mater. Sci. 25, 478 (2002).

[27] R. Dovesi, R. Orlando, B. Civalleri, C. Roetti, V. R. Saunders and C. M. Zicovich-Wilson, *CRYSTAL: A computational tool for the ab initio study of the electronic properties of crystals*, Zeitschrift Fur Kristallographie 220, 571 (2005).

[28] N. A. W. Holzwarth, G. E. Matthews, R. B. Dunning, A. R. Tackett and Y. Zeng, *Comparison of the projector augmented-wave, pseudopotential, and linearized augmented-plane-wave formalisms for density-functional calculations of solids*, Phys. Rev. B 55, 2005 (1997).

[29] http://www.abinit.org/

[30] J. P. Perdew and Y. Wang , *Accurate and simple analytic representation of the electron-gas correlation energy*, Phys. Rev. B 45, 13244 (1992).

[31] J. E. Medvedeva, V. I. Anisimov, M. K. Korotin, O. N. Mryasov and A. J. Freeman, *The effect of Coulomb correlation and magnetic ordering on the electronic structure of two hexagonal phases of ferroelectromagnetic $YMnO_3$*, J. Phys.: Condens. Matter 12, 4947 (2000).

[32] O. K. Andersen, O. Jepsen and J. Zaanen O. Gunnarsson, *Density-functional calculation of the parameters in the Anderson model: Application to Mn in CdTe*, Phys. Rev. B 39, 1708 (1989).

[33] V. I. Anisimov and O. Gunnarsson, *Density-functional calculation of effective Coulomb interactions in metals*, Phys. Rev. B 43, 7570 (1991).

[34] http://www.tcm.phy.cam.ac.uk/~mdt26/crystal.html

[35] M. D. Towler, N. L. Allan, N. M. Harrison, V. R. Saunders, W. C. Mackrodt and E. Apra, *Ab initio study of MnO and NiO*, Phys. Rev. B 50, 5041 (1994).

[36] S. Piskunov, E. Heifets, R. I. Eglitis and G. Borstel, *Bulk properties and electronic structure of $SrTiO_3$, $BaTiO_3$, $PbTiO_3$ perovskites: An ab initio HF/DFT study*, Mat. Sci. 29, 165 (2004).

[37] D. Alfè (1998). Program available at http://chianti.geol.ucl.ac.uk/~dario.

[38] X. Gonze and C. Lee, *Dynamical matrices, Born effective charges, dielectric permittivity tensors, and interatomic force constants from density-functional perturbation theory*, Phys. Rev. B 55, 10355 (1997).

[39] A. Anderson, *The Raman effect* (New York, Marcel Dekker, INC., 1971).

[40] R. Madar, F. Weiss, O. Thomas and A. Abrutis J. P. Sénateur, Brevet français FR 2707671 (1993), Brevet européen EP 730671 (1994), Brevet américain US 945162 (1999).

[41] J. Thery, *Elaboration par MOCVD à injection pulsée d'oxyde de fer et d'oxydes de fer-bismuth* (Thesis, Université de Grenoble, 2006).

[42] Company SAFC Hitech. http://www.sigmaaldrich.com/SAFC/Global.html

[43] G. Nénert, M. Pollet, S. Marinel, G. R. Blake, A. Meetsma and T. T. M. Palstra, *Experimental evidence for an intermediate phase in the multiferroic $YMnO_3$*, J. Phys.: Condens. Matter 19, 466212 (2007).

[44] B. B. van Aken, A. Meetsma and T. T. M. Palstra, *Hexagonal $YMnO_3$*, Acta Crystallogr. C57, 230 (2001).

[45] A. Munoz, J. A. Alonso, M. J. Martinez-Lope, M. T. Casais, J. L. Martinez and M. T. Fernandez-Diaz, *Magnetic structure of hexagonal, $RMnO_3$ (R = Y, Sc): Thermal evolution from neutron powder diffraction data*, Phys. Rev. B 62, 9498 (2000).

[46] T. Katsufuji, M. Masaki, A. Machida, M. Moritomo, K. Kato, E. Nishibori, M. Takata, M. Sakata, K. Ohoyama, K. Kitazawa and H. Takagi, *Crystal structure and magnetic properties of hexagonal $RMnO_3$ (R = Y, Lu, and Sc) and the effect of doping*, Phys. Rev. B 66, 134434 (2002).

[47] K. Uusi-Esko, J. Malm, N. Imamura, H. Yamauchi and M. Karppinen, *Characterization of $RMnO_3$ (R = Sc, Y, Dy-Lu): High-pressure synthesized metastable perovskites and their hexagonal precursor phases*, Mater. Chem. Phys. 112, 1029 (2008).

[48] C. Zhong, X. Jiang, H. Yu, Q. Jiang, J. Fang and Z. Li, *First-principles studies of the magnetic structure and exchange interactions in the frustrated multiferroic $YMnO_3$*, J. Magn. Magn. Mater. 321, 1260 (2009).

[49] V. I. Anisimov, F. Aryasetiawan and A. I. Lichtenstein, *First-principles calculations of the electronic structure and spectra of strongly correlated systems: The LDA+U method*, J. Phys.: Condensed Matter 9, 767 (1997).

[50] C. Degenhardt, M. Fiebig, D. Fröhlich, Th. Lottermoser and R. V. Pisarev, *Nonlinear optical spectroscopy of electronic transitions in hexagonal manganites*, Appl. Phys. B 73, 139 (2001).

[51] M. Janoschek, B. Roessli, L. Keller, S. N. Gvasaliya, K. Conder and E. Pomjakushina, *Reduction of the ordered magnetic moment in $YMnO_3$ with hydrostatic pressure*, J. Phys.: Condens. Matter 17, 425 (2005).

[52] C. J. Fennie and K. M. Rabe (unpublished).

[53] S. C. Abrahams, *Ferroelectricity and structure in the $YMnO_3$ family*, Acta Cryst. B 57, 485 (2001).

[54] M. N. Iliev, H. G. Lee, V. N. Popov, M. V. Abrashev, A. Hamed, R. L. Meng and C. W. Chu, *Raman- and infrared-active phonons in hexagonal $YMnO_3$: Experiment and lattice-dynamical calculations*, Phys. Rev. B 56, 2488 (1997).

[55] S. C. Miller and W. F. Love, *Tables of irreducible representations of space groups and co-representations of magnetic space groups* (Pruett, Boulder, 1967).

[56] Ph. Ghosez, J.-P. Michenaud and X. Gonze, *Dynamical atomic charges: The case of ABO_3 compounds*, Phys. Rev. B 58, 6224 (1998).

[57] M. Zaghrioui, V. Ta Phuoc, R. A. Souza and M. Gervais, *Polarized reflectivity and lattice dynamics calculation of multiferroic $YMnO_3$*, Phys. Rev. B 78, 184305 (2008).

[58] Ph. Ghosez, *First-principles study of the dielectric and dynamical properties of barium titanate* (Thesis, Université Catholique de Louvain, 1997).

[59] J. Vermette, S. Jandl, A. A. Mukhin, V. Yu Ivanov, A. Balbashov, M. M. Gospodinov and L. Pinsard-Gaudart, *Raman study of the antiferromagnetic phase transitions in hexagonal $YMnO_3$ and $LuMnO_3$*, J. Phys.: Condens. Matter 22, 356002 (2010).

[60] H. Fukumura, S. Matsui, H. Harima, K. Kisoda, T. Takahashi, T. Yoshimura and N. Fujimura, *Raman scattering studies on multiferroic $YMnO_3$*, J. Phys.: Condens. Matter 19, 365239 (2007).

[61] H. T. Stokes, D. M. Hatch, and B. J. Campbell (2007). ISOTROPY. stokes.byu.edu/isotropy.html

[62] M. Stengel (unpublished).

[63] M. Stengel and D. Vanderbilt, *Berry-phase theory of polar discontinuties at oxide-oxide interfaces*, Phys. Rev. B 80, 241103 (R) (2009).

[64] M. Stengel, C. J. Fennie and Ph. Ghosez, *Electrical properties of improper ferroelectrics from first principles*, Phy. Rev. B 86, 094112 (2012).

[65] J. Junquera and Ph. Ghosez, *Critical thickness for ferroelectricity in perovskite ultrathin films*, Nature 422, 506 (2003).

[66] N. Sai, C. J. Fennie and A. A. Demkov, *Absence of Critical Thickness in an Ultrathin Improper Ferroelectric Film*, Phys. Rev. Lett. 102, 107601 (2009).

[67] P. A. Salvador, T. D. Doan, B. Mercey and B. Raveau, *Stabilization of $YMnO_3$ in a perovskite structure as a thin film*, Chem. Mater. 10, 2592 (1998).

[68] O. Yu. Gorbenko, S. V. Samoilenkov, I. E. Graboy and A. R. Kaul, *Epitaxial stabilization of oxides in thin films*, Chem. Mater. 14, 4026 (2002).

[69] X. Martí, F. Sánchez, J. Fontcuberta, M. V. García-Cuenca, C. Ferrater, and M. Varela, *Exchange bias between magnetoelectric $YMnO_3$ and ferromagnetic $SrRuO_3$ epitaxial films*, J. Appl. Phys. 99, 08P302 (2006).

[70] A. Bosak, *Synthèse par MOCVD et caractérisation structurale et de magnéto-transport de couches minces de manganite de terre-rare non-substituées - Applications à des dispositifs de type jonctions "marche"*, PhD thesis (2003).

[71] I. Gélard, *Hétérostructures d'oxydes multiferroïques de manganites de terres rares hexagonaux $RMnO_3$ – Elaboration par MOCVD à injection et caractérisations structurales et physiques* (Thesis, Institut Polytechnique de Grenoble, 2009).

[72] I. Gélard, N. Jehanathan, H. Roussel, S. Gariglio, O. I. Lebedev, G. Van Tendeloo and C. Dubourdieu, *Off-stoichiometry effects on the crystalline and defect structure of hexagonal manganite $REMnO_3$ films (RE = Y, Er, Dy)*, Chem. Mater. 23, 1232 (2011).

[73] Company CrysTec. www.crystec.de